UNIVERSIDADE TÉCNICA DE LISBOA

INSTITUTO SUPERIOR TÉCNICO

The ASDEX Upgrade broadband microwave reflectometry system

António Guilherme Pereira Ehrhardt Gonçalves Silva
(Licenciado)

Dissertação para obtenção do Grau de Doutor em
Engenharia Electrotécnica e de Computadores

Orientador: Doutora Maria Emília Morais da Fonseca e Silva da Costa Manso

Júri:

Presidente: Reitor da Universidade Técnica de Lisboa

Vogais: Doutor Armando Mário Larcher Esteves Brinca
Doutor Michael Kaufmann
Doutor José Fernando da Rocha Pereira
Doutora Maria Emília Morais da Fonseca e Silva da Costa Manso
Doutor Fernando Manuel Moreira Serra
Doutor Carlos António Cardoso Fernandes
Doutor Joaquin Sanchez

Dezembro de 2006

Resumo

Este trabalho descreve em detalhe o desenho e implementação do sistema de reflectometria de banda larga para o Tokamak ASDEX Upgrade. Foram tomados como objectivos a atingir, a medida automática de perfis de densidade e suas flutuações desde a região periférica da coluna de plasma até ao centro da mesma, com elevada resolução temporal (< 50 μs) e espacial (< 5 mm). Contribuir para a compreensão de diversos fenómenos ligados ao transporte de partículas no plasma e testar algumas das soluções que permitam o uso da reflectometria como um diagnóstico de rotina nas futuras gerações de máquinas de fusão nuclear. Optou-se pela técnica de FM de banda larga por ser a que garante de uma forma mais eficaz os requisitos de elevada resolução temporal e espacial. Com uma gama de frequências de 16 a 100 GHz o sistema cobre as densidades de 0.3×10^{19} a 6.76×10^{19} m^{-3} na zona de elevado campo magnético (HFS) e de 0.3×10^{19} a 12.2×10^{19} m^{-3} na zona de baixo campo magnético (LFS), num total de 11 canais. O recurso a geradores de estado sólido, associados a conjuntos de multiplicadores de frequência activos e passivos permitiu localizar todos os componentes de emissão e recepção junto (< 2 m) à máquina. Estes geradores permitem variar toda a sua gama de frequências em tempos na ordem de 20 μs, quando actuados por um amplificador de desenho especifico. Foram realizadas um conjunto de medidas com plasma e sem plasma para avaliar o desempenho operacional do sistema e a sua capacidade para contribuir para a realização de estudos de física em plasmas de fusão.

Abstract

This work describes in detail the design and implementation of the ASDEX Upgrade broadband microwave reflectometer system. The main objectives were to be able to compute automatic density profiles and the related fluctuations from the scrape off layer up to the plasma center with high temporal (< 50 μs) and spatial (< 5 mm) resolutions. Contribute to a better understanding of the phenomena related to particle transport and to test different solutions that can make reflectometry a standard diagnostic for the next generation of fusion machines. The choice of the technique went to broadband FM because it guarantees the required high temporal and special resolutions. With eleven channels covering the frequency ranges from 16 to 100 GHz the system can probe the High Field Side (HFS) between 0.3×10^{-19} and 6.76×10^{-19} and the Low Field Side (LFS) between 0.3×10^{-19} and 12.2×10^{-19}. The use of solid state generators combined with active and passive frequency multipliers permitted that all microwave components could be placed close to the vessel (< 2 m). These generators could be swept in full frequency range in some 20 μs, when actuated by a custom made voltage amplifier. Several measurements without and with plasma were made to evaluate the operational performance of the system and the ability to contribute to physic studies in fusion plasmas.

Palavras Chave

- Reflectometria de micro-ondas
- Plasma de fusão
- Perfil de densidade electrónica
- Flutuações de densidade
- Varrimento rápido
- Energia de fusão nuclear

Keywords

- Microwave reflectometry
- Fusion plasma
- Electron density profile
- Density fluctuations
- Fast sweeping
- Nuclear fusion energy

Dedication

To my beloved wife Adriana, my son André and to my Parents for their unconditional support throughout all these years.

Acknowledgments

The successful completion of this thesis would not have been possible without the cooperation and help of many people. I would like to thank my supervisors Maria Emília Manso and Fernando Serra who first lead me to an all new world of fusion research, and gave me the opportunity to work in the ASDEX and ASDEX Upgrade projects, and for all their constant advice, support, and encouragement.

I also want to express my deepest gratitude to all my colleagues in the Microwave Group, for all their help and advice and for the excellent work environment that they have provided. In particular, I would like to thank Dr. Paulo Varela and Sérgio Vergamota, who shared a large part of their lives with me during all these years, and for all the good moments we spent together that can't be and will be not forgotten. Thank you both! I would like also to have a word of gratitude to Dr. Luis Cupido for his indispensable technical collaboration.

A word of gratitude also to Max-Planck-Institut für Plasma Physik and to all their members. A great place to work!

I would also like to thank Centro de Fusão Nuclear of Instituto Superior Técnico for the opportunity to work in the Microwave Group, and Junta Nacional de Investigação Científica e Tecnológica and European Atomic Energy Community for the financial support.

Last but not the least, I would like to thank my family for all their love and support, in particular to my wife Adriana without whose constant support and encouragement, even when my mood wasn't on it's best, I may have never finished this long term project of my life.

Lisbon, December, 2006

António Guilherme Pereira Ehrhardt Gonçalves Silva

Contents

List of Figures

List of Tables

Everything should be made as
simple as possible but not simpler.

Albert Einstein, *In Albert Einstein,*
Creator and Rebel by Banesh Hoffman
1972 (New York: Viking)

1 Introduction

1.1 Thermonuclear fusion

The planet increasing demand for energy is the motivation for the search of new energy sources. These sources must be clean, safe and at reach of all nations, the developed ones and the emerging ones. Nuclear fusion is the power behind all of the bright stars of the sky, including our sun. If successfully achieved on earth in a controlled manner, fusion represents a potentially unlimited source of energy, and with those three most wanted characteristics [1].

And what is fusion? Take two light atoms and fuse them to form a heavier atom. In the end, you end up with less mass than the one from the original reactants, but you have obtained some energy. It is not an easy process, and we have to look for the most interesting fusion reactions, the ones with high probability of occurrence, and for which the reacting elements are easily and abundantly available on earth. Looking for all the possible fusion reactions, the one between deuterium and tritium (D–T), or

$$ {}_1D^2 + {}_1T^3 \rightarrow {}_2He^4 + {}_0n^1 + 17.6\,(\mathrm{MeV}) \tag{1.1} $$

is one of the easiest to attain because it has a high probability of occurrence at one of the lowest energies. From all the released energy most of it, some 14.1 MeV, goes with the neutron, and the rest (3.5 MeV) is left with ${}_2He^4$, an α particle (see figure 1.1).

The deuterium exists on every glass of water, but the tritium is very difficult to be obtained. Only very small amounts exists on a few labs in the world, but fortunately only a few grams are needed to start the fusion reaction, and the rest of it is generated within the process by recombination of the released neutrons with the lithium protection blanket. A thermonuclear fusion reaction is possible if we heat the deuterium-tritium gaseous fuel to very high temperatures ($\sim 10^8$ Kelvin), fully ionizing both elements. This mixture of positively charged ions and negatively charged electrons is called plasma. Since we are dealing with charged particles, magnetic fields can be used to confine this hot mixture,

[1] The structural materials of the fusion reactor will become activated for an estimated period of about 100 years.

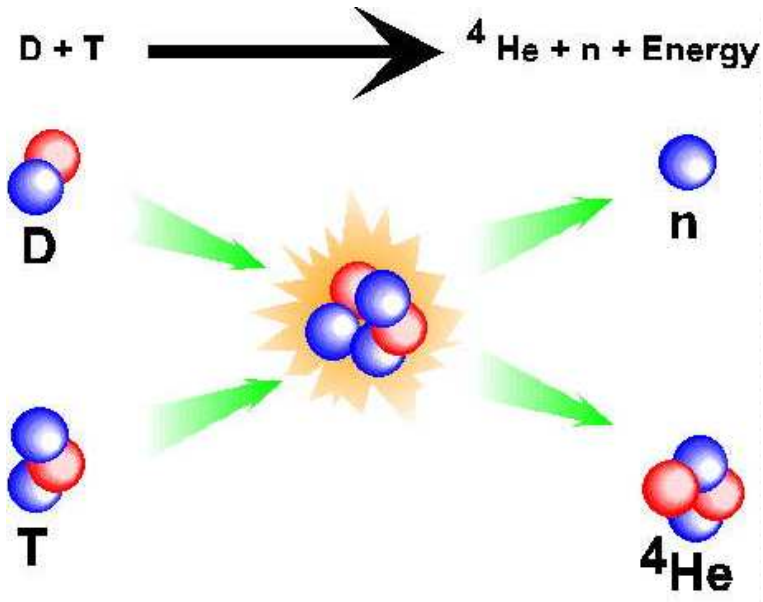

Figure 1.1: D-T fusion reaction

preventing it from running against the walls of what container is in, avoiding the immediate re-cooling. This is the principle behind the magnetic confinement concept, where the plasma particles are magnetically confined. The tokamak is one of the most promising fusion devices that uses this principle. The word tokamak comes from the Russian words **TO**roidal **KA**mera and **MA**gnitnaya **KA**tushka, meaning toroidal chamber and magnetic coil. The device was invented in the former Soviet Union in the early 60s, and is one of the most successful devices for thermonuclear fusion experiments and future reactors.

Figure 1.2 shows a schematic view of a tokamak. The toroidal geometry of the tokamak is defined by the distance between the center of the toroidal chamber and the center of the plasma column R_0, and the radius of the plasma column r. The total magnetic field has two main components: the toroidal field, B_ϕ, created by the external toroidal field coils and varying radially with the reciprocal of the distance to the center of the torus; the poloidal field B_θ, created by the plasma current I_p that flows in the poloidal direction. The combination of these two components of the magnetic field generates a nest with helical trajectory twisted around the plasma current as shown on figure 1.2. A transformer action generated by the primary circuit that setup a flux change through the torus, induces a toroidal electrical field, creating the plasma current. In a transformer it is only for a limited time that an increasing current can be generated in the primary winding so that a current can be driven in the plasma. This is why a tokamak does not work in continuous, but in pulsed mode. In order to achieve steady state operation in a future tokamak power plant, investigations are being conducted on methods of generating

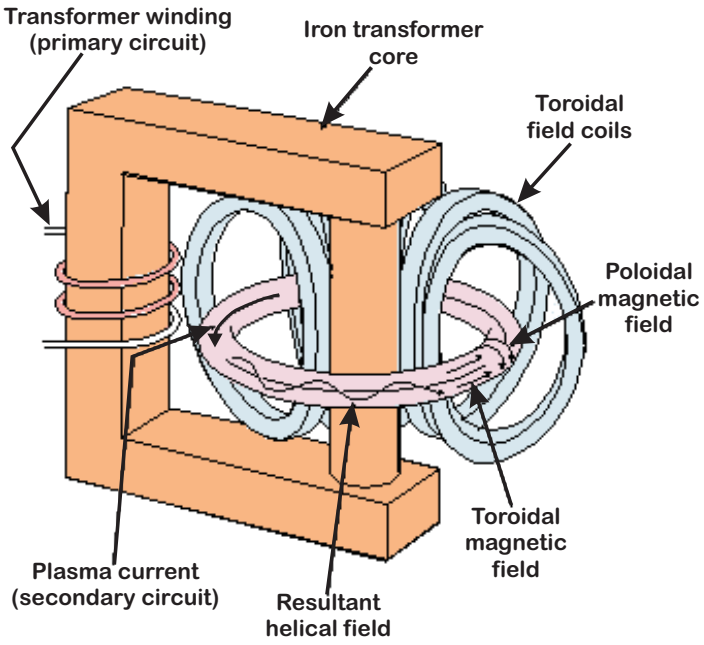

Figure 1.2: Schematic view of a tokamak.

current in continuous mode, e.g. by means of high-frequency waves. The plasma must be kept away from the torus walls to control the heat exhaust from the plasma to the wall and avoid an impurity flux from the wall to the plasma core, as a result of the plasma-wall interaction that leads to a wall erosion. This represents one major problem for fusion and can be solved by two different techniques: a) define a boundary by means of a physical limiter placed on a poloidal position; b) a modification of the magnetic field to generate a magnetic divertor.

To make the thermonuclear fusion possible the plasma must be self-sustained, i.e. you just have to put in fuel. The ignition condition must be reached, and to do so the energy released from the plasma must be retained for some time. Imagine a match that you attempt to lit. If the head of the match burns for time enough to ignite the wood (your fuel), you have succeeded. But if the wind blows turning off the head you will fail. The cross-section, σ, of the reactions depend on the relative energies of the primary nuclei [1]. For relatively low energies (<100 keV), σ is determined by the amount of energy required to overcome the Coulomb forces. The D–T reaction has the highest σ of all possible fusion reactions at the lowest energy ($\approx$100 keV). In an equilibrium state the particles in the plasma exhibit a Maxwell-Boltzman energy distribution function. Fortunately, the actual temperature of the plasma can be significantly lower (in the range of 10 to 20 keV) than the energy required to overcome the Coulomb forces since the fusion reactions

are predominantly produced by high energy ions in the "tail" of the distribution. For a D–T fusion plasma the so-called triple fusion product, $n_i \tau_E T_i$, sets the requirements for ignition. Where n_i is the plasma ion density, T_i is the ion temperature and τ_E is the ratio of the total energy in the plasma over the total power supplied to maintain the plasma, also called energy confinement time. In the case of parabolic density profiles the peak ignition requirement is

$$n_i \tau_E T_i > 5 \times 10^{21} \, (\mathrm{keV\,s\,m^{-3}}) \, . \tag{1.2}$$

From equation (1.2) τ_E is the key quantity and can only be improved by reducing the plasma losses, in particular the electron bremsstralung, radiation of impurities in the plasma, and the energy and particle flow out of the plasma. All of these are strongly associated to the evolution of the electron density profile and to the presence of localized fluctuations. Is therefore of great importance to have diagnostics with the capability to measure density profiles and their associated density fluctuations with high spatial and temporal resolutions, to progress towards the better knowledge of all mechanisms involved in a fusion plasma.

1.2 The ASDEX Upgrade Tokamak

The ASDEX Upgrade divertor tokamak (**A**xially **S**ymmetric **D**ivertor **EX**periment) went into operation at Garching in 1990, and at present, it is Germany's largest fusion device. It is the successor of the successful ASDEX, which was in operation between 1980 and 1990. The pioneer divertor design configuration of the ASDEX tokamak demonstrated the advantageous impurity control capabilities of this configuration when compared to the limiter configuration, leading to the discovery of the so-called H-mode regime, which is characterized by an enhancement of the energy confinement.

The main role of the divertor is to remove the outer boundary layer of the plasma and deposit it in target plates. This cool particles (compared with the plasma core) can than be pumped out of the vessel. As a result, the tokamak walls are preserved and better thermal insulation is achieved, improving the confinement time.

The divertor principle was also adopted on the ASDEX Upgrade tokamak, and later it was also introduced on Join European Torus (JET), which has been previously design to be a limiter tokamak. On both machines different divertor configurations have been tested, in an extremely relevant set of experiments for the design of the future International Thermonuclear Experimental Reactor (ITER), which will also incorporate the divertor concept. The ASDEX Upgrade tokamak also uses a reactor-like setup of external vertical field coils which are used for divertor plasma shaping. The main technical parameters of

Major plasma radius R_0	$1.65\,m$
Minor horizontal plasma radius r	$0.5\,m$
Plasma height b	$0.8\,m$
Ellipticity b/r	1.8
Triangularity δ	$0.4\,/\,0.4$
Plasma volume V_{plasma}	$13\,m^3$
Vessel volume V_{vessel}	$32\,m^3$
Plasma surface S_{plasma}	$42\,m^2$
Magnetic field B	2.7 T
Plasma current I_p	2 MA
Pulse duration	< 10 s
Heating power P_H	up to 18 MW
Plasma temperature T_e, T_i	2–3 keV
Plasma quantity	3 mg
Electron density n_e	$< 30 \times 10^{19}\,m^{-3}$

Table 1.1: ASDEX Upgrade main parameters.

ASDEX Upgrade are listed in table 1.1.

The main plasma physical targets are:

Divertor physics - Optimization of the divertor concept. Comparison of different divertor geometries. Uses a reactor-relevant arrangement of vertical field coils, placed outside the toroidal field coils, forming the divertor shape of the plasma with an X-point. Very detailed setup of diagnostics in the divertor region permit comprehensive studies.

Plasma wall interaction - Heat and particle flow can lead to erosion of the wall material, introducing impurities in the plasma. Use of graphite wall and metallic (e.g. tungsten) wall.

Plasma edge related operation - Various operation boundaries of a fusion plasma have its source at the plasma edge. Physics of the structure of a transport barrier at the plasma edge; causes for the limitation of the plasma density; physics and transport properties of the "Edge Localized Modes" (ELMs), and the connection of the edge parameters to the overall plasma confinement, are subjects under investigation.

Transport investigations - The excellence of the plasma confinement is one of the key factors to determine the size of a fusion reactor in order to ignite. The ASDEX data have been used in a common international data base aiming to the prediction

of the confinement for ITER. The local transport is investigated by measurement of the transport coefficients. Study of non-local transport.

Particle fueling - The central particle refilling can be achieved by ejecting pellets into the plasma. These are frozen hydrogen or deuterium balls accelerated to several $m \cdot s^{-1}$. At ASDEX Upgrade several different injection systems are under investigation. This is a crucial subject for future fusion reactor devices.

Internal transport barrier - The confinement can considerably improved if the turbulent radial transport can be suppressed. This is achieved in the bulk plasma by the formation of the so-called internal transport barriers (ITB). An ignited reactor with a sustained ITB can be smaller and therefore cheaper than with a conventional concept. Stationary ITBs are under investigation on ASDEX Upgrade.

Magnetohydrodynamic stability - Magnetohydrodynamic (MHD) instabilities impose a sever limitation to the operation of the present devices in stable confinement scenarios. The understanding of the physical mechanisms of the instabilities like neoclassical tearing modes (NTM) or disruptions, are of crucial importance for the development of efficient and stable confinement scenarios, and therefore are a topic of investigation on ASDEX Upgrade.

1.3 This thesis

Local measurements of the electron density profile in tokamaks are of crucial importance. The investigation of the mechanisms that influence the transport and therefore the plasma confinement requires local electron density profile measurements with high spatial and temporal resolution. For the next large tokamaks like ITER, it became clear the need for density diagnostics requiring reduce access and with improved accuracy and spatial resolution electron density profiles. The ability to track fast density profile changes and control the plasma position during long discharges where the magnetic diagnostics have no possibilities to give accurate results are of crucial importance. Microwave reflectometry meets the above requirements. Basically, the electromagnetic waves propagate in the plasma and are reflected at a plasma layer where it equals a characteristic frequency of the plasma, the cutoff. From the phase shift that the waves undergo in the plasma column as a function of the probing frequency $\phi(F)$ the density profile can be determined; if a fixed frequency is used fluctuations studies can be performed from the temporal evolution of the phase $\phi(t)$. Microwave reflectometry has been widely used as ionosphere plasma diagnostic [2][3] and has been proposed in the early 60's as a method to measure electron

plasma density in laboratory plasmas [4][5]. However, only after recent technological microwave advances reflectometry was considered as an important diagnostic for fusion plasmas [6][7]. Reflectometric systems have been developed for large tokamaks as *Tore Supra* [8], *ASDEX* [9], *D-III* [10], and for *JET* [11]; and also in other magnetic fusion machines such as for the ATF *Torsatron* [12], the Wendelstein VII-AS *Stellerator* [13] and RFX *Reversed Field Pinch* [14].

Several techniques have been developed: swept narrow or broadband, fixed frequency, amplitude modulation of a continuous wave, pulse radar, pulse compression, noise correlation. All this techniques tried to overcome problems like pour quality transmission lines or plasma fluctuations. Reflectometry became a rapidly expanding field, but it is realized that further experimental and theoretical work must be carried out in order to fully exploit its great potentialities. Although a now well established microwave diagnostic for fusion plasma, reflectometry is still a broad area of research.

This thesis describes the design and implementation of the ASDEX Upgrade ultrafast broadband frequency modulated microwave reflectometry system. The main purpose of the scientific program is the study of the transport properties in the ASDEX Upgrade plasma, using reflectometry to measure electron density profiles and density fluctuations in the peripheral and scrape-off layer plasma in a wide range of plasma scenarios. The system was designed in such a way that some features required for the operation in the next step devices can be tested, contributing for the assessment of microwave reflectometry as a standard diagnostic for the nest fusion devices. Both broadband swept and fixed frequency operation are possible, probing plasma densities up to $15 \times 10^{19}\, m^{-3}$, from the high and low field sides of the plasma column. The routine operation is one of the main goals and this was only achieved for the first time with the development of the ASDEX Upgrade reflectometry system. To accomplish this the sweeping times must be smaller than the characteristic period of the plasma electron density perturbations, which implies the development of a system beyond the state of the art. In order to minimize the influence of density fluctuations during broadband operation fast frequency sweeping is used ($\leq 100\mu s$). The use of a combination of solid state Hyperabrupt varactor tuned oscillators (HTO) with frequency multipliers ensure fast sweeping in the required frequency range of 16-110 GHz. Special care was also taken on the design of the transmission lines, with decoupled in going and out going lines and one in-vessel hog-horn focused antenna per channel, minimizing the spurious reflections. A lot of effort was also be applied on the development of dedicated signal processing tools. The thesis is organized as follows. Chapter 2 consists of a review of the theory related to the propagation of microwaves in the tokamak plasma, and the experimental techniques that have been developed for

use in reflectometry. The basic principles of microwave reflectometry are presented. The different microwave reflectometry techniques are discussed in terms of there capability to achieve the measuring objectives for the diagnostic, and difficulty of implementation.The option for a frequency modulated broadband reflectometry system is justified. In chapter 3 the design and implementation of system is described. The tests of some critical microwave components are presented. The calibration and in-vessel testing are also included. On chapter 4 a set of experimental results obtained on different plasma scenarios are presented. They are meant to show the different capabilities of the diagnostic and evaluate the performance during a plasma discharge. Chapter 5 concludes with a brief description of the future work on this system and application of this diagnostic to future fusion experiments like ITER.

References

[1] John Wesson. *Tokamaks*. Clarendon Press · Oxford, 1987.

[2] K. G. Budden. *Radio Waves in the Ionosphere*. Cambridge University Press, 1961.

[3] V. L. Ginzburg. *The Propagation of Electromagnetic Waves in Plasmas*. Pergamon Press, Second edition, 1970.

[4] A.I. Anisimov, N.I. Vinogradov, V.E. Goland, and B.P. Konstantinov. Method of investigating electron spatial distribution in a plasma. *Soviet Physics*, 5(9):939–1074, February 1961.

[5] E. Mazzucato. Rep. matt-1151. Technical report, Princeton PPL, 1975.

[6] A. Cavallo and R. Cano. Proposal for density profile measurements by reflectometry in large tokamaks. Technical Report EUR-CEA-FC-1337, EURATOM, January 1982.

[7] F. Simonet. *Étude de la reflectométrie hyperfrequence en modes ordinaire et extraordinaire pour la mesure du profil radial et des fluctuations locales de la densité électronique dans les tokamaks*. PhD thesis, Université de Nancy I, 1985.

[8] P. Millot and F. Simonet. A broadband microwave reflectometer for TORE SUPRA. In *Proceedings on* 14^{th} *European Conference on Controlled Fusion and Plasma Physics*, pages 1303–1305. European Physical Society, 1987.

[9] M. E. Manso, F. Serra, J. Mata, J. Barroso, J. Comprido, C. Teixeira, P. Caetano, P Luz, A. Monteiro, A. Silva, J. Mendonça, J. Neves, J. Pereira, S. Ramos, A. Almeida, L. Cupido, and P. Marques. A microwave reflectometric system for the ASDEX tokamak. In *Proceedings on* 15^{th} *European Conference on Controlled Fusion and Plasma Physics*, volume 12B, pages 1127–1130. European Physical Society, 1988.

[10] T. Lehecka, W. A. Peebles, N. C. Luhmann, S. R. Burns, and E. Olson. Reflectometry systems for the DIII-D tokamak. *Review of Scientific Instruments*, 59(8):1620–1622, 1988.

[11] R. Prentice, A. C. C. Sips, J. A. Fessey, and A. E. Costley. First measurements of electron density profiles on JET with a multichannel reflectometer. In *Proceedings on* 17^{th} *European Conference on Controlled Fusion and Plasma Heating*, volume 14B, pages 1500–1503. European Physical Society, 1990.

[12] E. Anabitarte. Density fluctuation measurements on ATF using a two-frequency reflectometer. In *Proceedings on* 17^{th} *European Conference on Controlled Fusion and Plasma Heating*, page 1492. European Physical Society, 1990.

[13] J. Sanchez, H. J. Hartfuss, E. Anabitarte, A. P. Navarro, and WVII-AS Team. Reflectometry observations of density fluctuations in Wendelstein VII-AS stellarator. In *Proceedings on* 17^{th} *European Conference on Controlled Fusion and Plasma Heating*, page 1572. European Physical Society, 1990.

[14] M. Moresco. Internal report. Technical report, Univ. Padova, 1990.

2 Microwave Reflectometry

On a fusion plasma material probes can only be used at very low density edge plasma regions, due to the high temperature of the fusion plasma. Therefore, non-perturbing methods of diagnostic, like the ones that uses laser beams or those based on the properties of propagating microwaves in the plasma, must be employed.

Microwave reflectometry is a radar technique that was first used for ionospheric sounding [1][2], and started to be applied to measure the electron density profile in fusion plasmas in 1985. The principle of operation is based on the fact that a propagating electromagnetic wave in an inhomogeneous plasma is reflected at some critical density layer, where the local refractive index goes to zero. The electron density at the cutoff is obtained directly from the wave frequency. The position of the reflecting layer is obtained from the time delay of the wave propagating from the source and back to the receiver. This chapter is dedicated to a review of the theory and experimental techniques that have been developed for use of reflectometry in fusion plasmas.

2.1 Propagation of millimetre waves in a magnetized plasma

The electromagnetic wave equation for a dielectric medium such as magnetized plasma contains many terms and the solution is difficult to interpret. For these reason approximations are introduced to make the problem more tractable. It is also not within the scope of this work the study of general propagation of waves in plasmas, and here will only be considered the perpendicular propagation of a wave to the magnetic field lines in the tokamak, which is relevant for reflectometry analysis. The approximations utilized are:

Cold plasma approximation - In the absence of electromagnetic perturbations the plasma particles stay in their equilibrium positions and in the presence of a perturbing field they will oscillate around those positions. This is valid as long as the thermal movements are negligible when compared to the oscillations induced by the

electromagnetic field. The plasma is considered a fluid of electrons and ions coupled by means of the wave's electromagnetic field, which is true when the thermal effects are not important and the phase velocity of the wave v_ϕ is large when compared with the thermal velocity v_{th}. This means that are no dissipation losses and that the energy of the wave is constant.

High frequency approximation - When the frequency of the electromagnetic wave is much higher than the cyclotron frequency of the plasma ions, the wave-induced movement of the ions can be neglected due to ions inertia. This is equivalent to make $m_i \to \infty$. Only the electrons will contribute to the medium polarization.

Slab model - The dielectric constant only varies in the direction of propagation, which is the equivalent to say that the plasma is only inhomogeneous in the direction of propagation and homogeneous in the other directions.

2.1.1 The wave equation

The *Maxwell* equations describe the macroscopic behaviour of the electromagnetic field. They express the relations between the magnetic field **H**, the electric field **E**, the magnetic density **B** and the electric density **D**, and can be written as [3]:

$$\nabla \cdot \mathbf{D} = \rho \tag{2.1}$$

$$\nabla \cdot \mathbf{B} = 0 \tag{2.2}$$

$$\nabla \times \mathbf{E} = -\frac{\partial \mathbf{B}}{\partial t} \tag{2.3}$$

$$\nabla \times \mathbf{H} = \mathbf{J} + \frac{\partial \mathbf{D}}{\partial t} \tag{2.4}$$

ρ is defined as the electric charge density and **J** is the electric current density . Equation (2.1) is known as *Gauss's theorem* and shows that electric flux starts and ends on charges. By equation (2.2) the magnetic flux lines are closed. The *Faraday's law* in equation (2.3) an electric field can be induced by a time-varying magnetic filed. At last equation (2.4) shows that the source of the magnetic field is the current and its coupled to the electric field. We should also consider the so called material equations:

$$\mathbf{D}(\mathbf{r}, t) = \varepsilon_o \mathbf{E} \tag{2.5}$$

$$\mathbf{B}(\mathbf{r}, t) = \mu_o \mathbf{H} \tag{2.6}$$

Equations 2.5 and 2.6 are valid for vacuum without sources available in the medium,

and where μ_o is the magnetic permeability and ε_o the dielectric constant. If we now consider a material medium, the presence of an electromagnetic field will change the charge and currents distribution given rise to electric and magnetic dipoles. We have now the electric polarization vector $\mathbf{P}$ and the magnetic polarization vector $\mathbf{M}$, which are related to $\mathbf{E}$, $\mathbf{H}$, $\mathbf{B}$, and $\mathbf{D}$ by the constitutive relations:

$$\mathbf{D} = \varepsilon_o \mathbf{E} + \mathbf{P} \tag{2.7}$$

$$\mathbf{B} = \mu_o (\mathbf{H} + \mathbf{M}) \tag{2.8}$$

And the *Maxwell* equations are now:

$$\nabla \cdot \mathbf{E} = \frac{\rho_T}{\varepsilon_o} \tag{2.9}$$

$$\nabla \cdot \mathbf{B} = 0 \tag{2.10}$$

$$\nabla \times \mathbf{E} = -\frac{\partial \mathbf{B}}{\partial t} \tag{2.11}$$

$$\nabla \times \frac{\mathbf{B}}{\mu_o} = \mathbf{J}_T + \varepsilon_o \frac{\partial \mathbf{E}}{\partial t} \tag{2.12}$$

with:

$$\mathbf{J}_T = \mathbf{J} + \nabla \times \mathbf{M} + \frac{\partial \mathbf{P}}{\partial t} \tag{2.13}$$

$$\rho_T = \rho - \nabla \cdot \mathbf{P} \tag{2.14}$$

In equation (2.13) the current-density term $\partial \mathbf{P}/\partial t$ is called the polarization current, and the term $\nabla \times \mathbf{M}$ is called the magnetization current. Also in equation (2.14) another charge-density term given by $-\nabla \cdot \mathbf{P}$ is present which expresses the fact that besides the free charge-density, there is a bound charge-density in the dielectric [4]. If we now consider a linear relation between polarization and fields (we are analysing a low power probing application), the polarization vectors $\mathbf{P}$ and $\mathbf{M}$ can be expressed by:

$$\mathbf{P} = \varepsilon_o \boldsymbol{\chi}_e(\mathbf{r}) \cdot \mathbf{E} \tag{2.15}$$

$$\mathbf{M} = \boldsymbol{\chi}_m(\mathbf{r}) \cdot \mathbf{H} \tag{2.16}$$

With $\boldsymbol{\chi}_e$ and $\boldsymbol{\chi}_m$being the electric and magnetic susceptibility tensors. We can now use equations (2.7) and (2.8) to write:

$$\mathbf{D} = \varepsilon_o(\mathbf{I} + \boldsymbol{\chi}_e) \cdot \mathbf{E} = \boldsymbol{\varepsilon} \cdot \mathbf{E} = \varepsilon_o \mathbf{K} \cdot \mathbf{E} \tag{2.17}$$

$$\mathbf{B} = \mu_o(\mathbf{I} + \boldsymbol{\chi}_m) \cdot \mathbf{H} = \boldsymbol{\mu} \cdot \mathbf{H} = \mu_o \mathbf{K}_m \cdot \mathbf{H} \tag{2.18}$$

where $\boldsymbol{\varepsilon}$ and $\boldsymbol{\mu}$ are the plasma dielectric and magnetic permeability tensors. The plasma is an ionized medium and the presence of an electromagnetic wave creates dipolar moments. It can be characterized by the dielectric tensor $\boldsymbol{\varepsilon}$, which implies that $\mathbf{J}$ is included in $\partial\mathbf{P}/\partial t$ making $\mathbf{J} = 0$ in *Maxwell* equations.

From *Maxwells* equations in an inhomogeneous isotropic medium [5], and assuming a cold plasma approximation (which implies that the absorption of the wave away from resonance can be ignored) the wave propagation equation can be derived:

$$\nabla^2 \mathbf{E}(x, y, z, t) - \frac{\boldsymbol{\varepsilon}(x, y, z)}{c^2} \cdot \frac{\partial^2 \mathbf{E}(x, y, z, t)}{\partial t^2} = 0 \tag{2.19}$$

Where $\boldsymbol{\varepsilon}(x, y, z)$ is the dielectric constant of the medium and c the velocity of light in vacuum. Considering plane waves propagating in an infinite, uniform medium (using the geometry of figure 2.1) with a time dependence $\exp(\jmath\,\omega t)$, the frequency of the electromagnetic wave is independent from the spatial position and this can be expressed by:

$$\mathbf{E}(x, y, z, t) = \mathbf{E}(x, y, z) \cdot \exp(\jmath\,\omega t) \tag{2.20}$$

with ω the angular frequency of the electromagnetic wave. We have now a three dimensional wave equation, and if we considered the slab approximation, the medium varies only in the $\mathbf{z}$ direction, then equation (2.19) can be written:

$$\begin{aligned} \frac{\partial^2 E_x}{\partial z^2} + k_o^2 \varepsilon_X(z) E_x = 0 \\ \frac{\partial^2 E_y}{\partial z^2} + k_o^2 \varepsilon_O(z) E_y = 0 \end{aligned} \tag{2.21}$$

where $k_o = \omega/c$ is the wavenumber, $\varepsilon_X = n_X^2$ and $\varepsilon_O = n_O^2$ are the dielectric constants for the two characteristic propagation modes, designated by extraordinary and ordinary modes, respectively. E_x and E_y are the wave electric field components. A characteristic wave is a plane wave that can be propagated in an anisotropic medium without suffering any changes to is polarization state, and the relation between the frequency ω and $\mathbf{k}$ must satisfy the dispersion relation. In an homogeneous anisotropic magnetoplasma a large number of different type of waves can propagate, but for reflectometry only linearly polarised waves whose direction of propagation is perpendicular to the magnetic field are

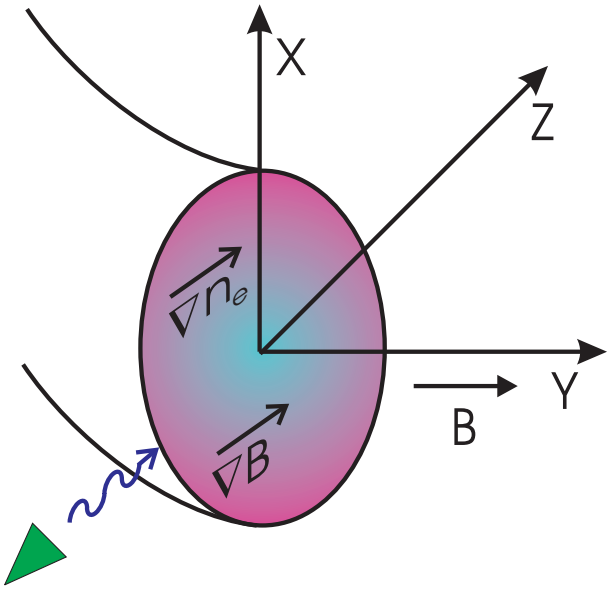

Figure 2.1: System of coordinates for the wave propagation in a magnetized plasma. Direction of the electron density and magnetic field gradients.

interesting for plasma probing. When perpendicular propagation to the magnetic field is considered together with the high frequency approximation, the Appleton-Hartree relation becomes [6]:

$$n^2_{O,X} = 1 - \frac{2(1-X)X}{2(1-X) - Y^2 \pm Y^2} \tag{2.22}$$

with $X = \omega^2_{pe}/\omega^2$ and $Y = \omega_{ce}/\omega$. Where the plus $(+)$ signal corresponds to the ordinary wave and the minus $(-)$ to the extraordinary wave.

From equation (2.22) we obtain for the two modes:

$$n^2_O = 1 - X = 0 \tag{2.23}$$

$$n^2_X = 1 - (1-X)\frac{X}{1-X-Y^2} = 0 \tag{2.24}$$

or

$$X = 1, \qquad \text{ordinary mode} \tag{2.25}$$

$$(1-X)\frac{X}{1-X-Y^2} = 1, \qquad \text{extraordinary mode} \tag{2.26}$$

In terms of electron plasma frequency f_{pe} and electron cyclotron frequency f_{ce} equa-

tion (2.22) can be written as:

$$n_O^2 = 1 - \frac{f_{pe}^2}{f^2} \tag{2.27}$$

$$n_X^2 = 1 - \frac{f_{pe}^2(f^2 - f_{pe}^2)}{f^2(f^2 - f_{pe}^2 - f_{ce}^2)} \tag{2.28}$$

where:

$$f_{pe} = \sqrt{\frac{n_e e^2}{4\pi^2 \varepsilon_o m_e}} \tag{2.29}$$

$$f_{ce} = \frac{eB_o}{2\pi m_e} \tag{2.30}$$

and n_e is the electron density, m_e is electron mass, e is the electron charge and B_o is the total magnetic field.

2.1.2 The full wave solution

The search for solutions of equations 2.21 has been a topic of intense research but no solution could be found for a medium with a generic profile of the dielectric constant $\varepsilon(z, f) = n^2(z, f)$.

The equation (2.21) can be written in a more general form

$$\frac{d^2E(z)}{dz^2} + k_o^2 \varepsilon(z, f) E(z) = 0 \tag{2.31}$$

For $\varepsilon(z, f) > 0$ the solution is of the form [7]:

$$E(z) = \alpha e^{-ik_o\sqrt{\varepsilon(z,f)}\cdot z} + \beta e^{ik_o\sqrt{\varepsilon(z,f)}\cdot z} \tag{2.32}$$

which is a linear combination of two independent oscillating solutions. The solution consists of two wave type solutions, with opposite directions of propagation (given by the + and − sign), but whose wavenumber in the medium of dielectric constant $\varepsilon(z, f)$ is $k(z, f) = k_o\sqrt{\varepsilon(z, f)}$. Thus, the wavelength of an electromagnetic wave propagating through a dielectric medium depends on the value of the dielectric constant of the medium.

If we now consider the case of $\varepsilon(z, f) < 0$ the equation (2.31) becomes [7]

$$\frac{d^2E(z)}{dz^2} - k_o^2 |\varepsilon(z, f)| E(z) = 0 \tag{2.33}$$

This has a solution in the form

$$E(z) = \alpha e^{-k_o\sqrt{|\varepsilon(z,f)|}\cdot z} + \beta e^{k_o\sqrt{|\varepsilon(z,f)|}\cdot z} \tag{2.34}$$

For waves incident in the positive z direction, physically β must equal zero, because if not, at large z, the magnitude of the electric field approaches infinity. Equation (2.34) becomes

$$E(z) = \alpha e^{-k_o\sqrt{|\varepsilon(z,f)|}\cdot z} \tag{2.35}$$

Thus the solution for $\varepsilon(z, f) < 0$ is that of an exponential damped wave, known as an evanescent wave.

The point where $\varepsilon(z, f) = 0$ is the so called *cut-off*. It is the point from which the most energy in the wave is reflected. However, for a wave propagating in a dielectric with $\varepsilon(z, f) \to 0$ continuously, reflection takes place gradually in the medium. This is known as reflection from the gradient. But this amount of power is small ($< 10\%$) until $\varepsilon(z, f)$ is close to zero. Close to the cut-off also the phase velocity of the propagating wave goes to infinity ($v_f = c/n \to \infty$). This region marks the boundary between the region of propagating waves and evanescent waves.

When the refraction index goes to infinity ($\varepsilon(z, f) \to \infty$) there is a resonance, and the wave energy can be absorbed by the medium.

If the electron density and the magnetic field profiles are known then the characteristics of a wave in a plasma can be derived. That is, the amplitude and the wavelength of the wave at different positions in the plasma can be determined. Furthermore the structure of the wave in the plasma can also be calculated, that is where it propagates to, where it is reflected from and where it is evanescent. However the problem is that to be able to calculate this information, the relevant plasma profiles like the electron density and magnetic field, must be known. For use as a plasma diagnostic however, it must be possible to relate the electron density and magnetic field inside the plasma to some measurable quantity of the reflectometer probing wave, like the phase of the reflected wave at some point out of the plasma. Complete solutions to the wave equation must be found so that the problem can be inverted. That is when a wave is launched into a plasma, it propagates through the plasma, is reflected at the reflecting layer and propagates out again. The phase change that the reflected wave undergoes in propagating through the plasma can be determined.

We have seen that a full wave solution for the wave equation must be oscillatory in space for $\varepsilon(z, f) > 0$, and exponentially damped for $\varepsilon(z, f) < 0$. The solution must also assure continuity in the transition between this two regions. To illustrate the results that

can be expected with a full wave approach we will solve the wave equation for a particular case of a linear dielectric constant profile [1].

The solution for a linear dielectric constant profile

Consider the linear dielectric profile of the form

$$\varepsilon(z, f) = 1 - \frac{z}{z_c(f)} \tag{2.36}$$

Combining with equation (2.31) gives the differential equation:

$$\frac{d^2E(z)}{dz^2} + k_o^2 \left(1 - \frac{z}{z_c(f)}\right) E(z) = 0 \tag{2.37}$$

If the linear transform $z \rightarrow \xi$ is used, where ξ is defined as

$$\xi = \left(\frac{\omega^2}{c^2 z_c}\right)^{1/3} (z_c - z) = \left(\frac{\omega z_c}{c}\right)^{2/3} \varepsilon(z, f) \tag{2.38}$$

the wave equation is transformed into the *Airy* equation

$$\frac{d^2E(z)}{d\xi^2} + \xi E(z) = 0 \tag{2.39}$$

The *Airy* equation is a modified *Bessel* function equation. This has a solution for the electric field in terms of the *Airy* functions $A_i(\xi)$ and $B_i(\xi)$ given by [8]

$$E(\xi) = \alpha A_i(\xi) + \beta B_i(\xi) \tag{2.40}$$

In this α and β are constants that depend on the boundary conditions of the problem. In practice the wave is damped to zero for $\varepsilon(z, f) < 0$. This may be used to determine the appropriate values for α and β. This is because for $\xi < 0$ the second *Airy* function $B_i(\xi) \rightarrow \infty$ whereas $A_i(\xi) \rightarrow 0$. Thus, the correct solution is the one where $\beta = 0$.

$$E(z) = \alpha A_i \left[\left(\frac{\omega^2}{c^2 z_c}\right)^{1/3} (z_c - z)\right] \tag{2.41}$$

The value of α is determined by initial conditions such as the magnitude and phase of the probing beam at the edge of the plasma.

Although the solution above contains all the information about the wave structure, the concepts of incident and reflected waves are not explicit. This is because the solution

is a standing wave created by the continuous interference of the incident and reflected waves. In fact, in the full wave solution the non localised reflection process is implicit in the standing wave whist for the more intuitive propagating wave theory, reflection must be treated as a separate process to propagation.

2.1.3 The Wentzel-Kramers-Brillouin (WKB) solution

Approximate solutions of the wave equation in an inhomogeneous plasma are usually obtained which permit to extract the incident and reflected wave contributions, and would allow the prediction of quantities that are actually measured, like the phase of the wave.

One such solutions is given by the *Wentzel-Kramers-Brillouin (WKB)* approximation that corresponds to neglect the secondary multiple reflections occurring at each infinitesimal small width plasma layer. Under this assumption the wave electric field is given by [3]:

$$E(z) = A\frac{1}{\sqrt{n(z,f)}}e^{\pm \jmath\, k_o \int n(z,f)dz} \tag{2.42}$$

which contains in a explicit form the incident and reflected waves represented by the $\pm$in the exponential.

It can be seen from equation (2.42) that the amplitude of the wave electric field increases $1/\sqrt{n(z,f)}$ when the wave approaches the cutoff layer z_c, where $n(z,f) \to 0$. This reflects the swelling of the electric field close to the reflection layer. However, the wave amplitude remains finite at $n(z_c,f) = 0$, as inferred from the exact solutions. This is a case where the *WKB* does not hold. This problem can be partially solved by making the phase term in equation (2.42) equal to zero at the cutoff [2]. In this case the magnitude of the electric field is proportional to:

$$|E(z)| \propto \frac{\sin(k_o n(z,f))}{\sqrt{n(z,f)}} \tag{2.43}$$

which approaches zero when $n(z,f) \to 0$.

The phase of the wave is given by the exponential term in the equation (2.42). It should be noted that the effect of the plasma on the wave phase is to introduce a a delay at a rate proportional to the local refractive index. Therefore the phase of the reflected wave is determined by the radial profile of the refractive index from the plasma periphery ($z = z_0$) up to the reflecting layer ($z = z_c$), according to:

$$\Delta\phi = 2k_o \int_{z_o}^{z_c} n(z,f)dz \tag{2.44}$$

The factor 2 is due to the fact that the wave propagates to and from the reflecting layer.

Validity conditions

In the region away from the reflecting layer, the *WKB* approximation can be used as long as the vacuum probing wavelength, λ_0, is smaller than the density gradient characteristic length [9]:

$$L(z) \gg \frac{\lambda_0}{2\pi} \tag{2.45}$$

where $L(z) = [(1/n_e)(dn_e/dz)]^{-1}$. In the regions where this condition breaks there is also some partial reflection. As it was previously referred, the *WKB* approximation is also not valid where $n(z, f) \to 0$ and the probing wavelength, $\lambda \to \infty$. In this region, the incident and reflected waves remain coupled by the reflection process, and the concept of independent propagating incident and reflected waves is no longer valid. The exact solution of the wave equation should be used to describe the wave propagation in this region.

Phase of the reflected wave and propagating regions

To derive the phase of the reflected wave we should consider the full propagation path of the wave that starts at the antenna mouth and goes up to the reflecting layer in the plasma. This path is divided in four regions as plotted in figure 2.2.

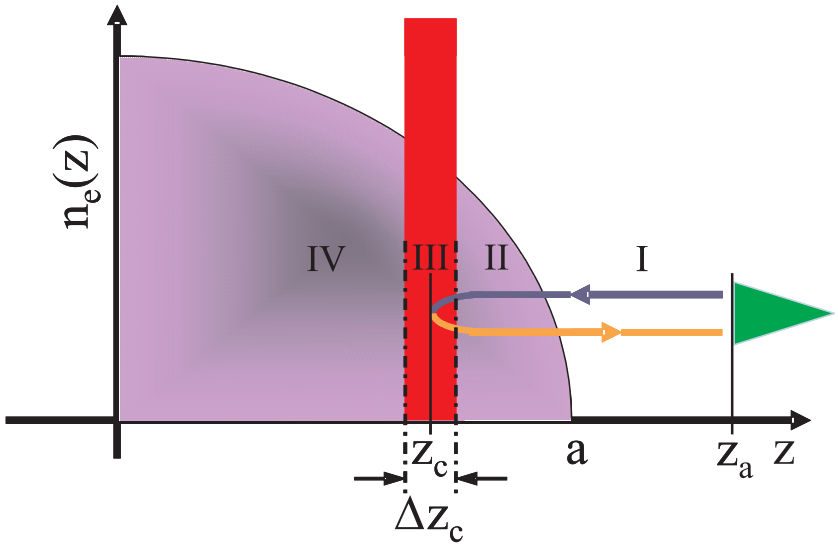

Figure 2.2: Schematic representation of incident and reflected waves in different regions: (I) vacuum; (II) propagating zone in the plasma; (III) reflecting layer; (IV) region not accessible with waves. z_c is the cutoff layer position and Δz_c the width of the reflecting layer. z_a is the antenna mouth position.

Region I - Propagation in vacuum between z_a and a. The electric field of the wave in this region is given by:

$$E_I(z) = \alpha_I e^{-\jmath\, k_o z} + \beta_I e^{\jmath\, k_o z} \tag{2.46}$$

Region II - The probing wave frequency is above the plasma characteristic frequency and the wave can freely propagate in the region . Using the the *WKB* approximation the electric field is:

$$E_{II}(z) = \frac{\alpha_{II}}{\sqrt{n(z,f)}} e^{-\jmath\, k_o \int_a^z n(z,f)dz} + \frac{\beta_{II}}{\sqrt{n(z,f)}} e^{\jmath\, k_o \int_a^z n(z,f)dz} \tag{2.47}$$

Region III - In this region the refractive index goes rapidly to zero and the *WKB* approximation is no longer valid. If the variation of the dielectric constant can be approximated to a linear profile, we can use the previous otained in section 2.1.2 and the electric field is given by:

$$E_{III}(z) = \alpha_{III} A_i(\xi) + \beta_{III} B_i(\xi) \tag{2.48}$$

Region IV - The probing frequency is always below the plasma characteristic frequency and the refractive index is imaginary, which implies that we have an evanescent wave. The *WKB* approximation is valid in this region and the electric field is:

$$E_{IV}(z) = \frac{\alpha_{IV}}{\sqrt{n(z,f)}} e^{-\jmath\, k_o \int_{z_c}^z n(z,f)dz} + \frac{\beta_{IV}}{\sqrt{n(z,f)}} e^{\jmath\, k_o \int_{z_c}^z n(z,f)dz} \tag{2.49}$$

The constants α_i and β_i can be found by imposing continuity conditions between the adjacent regions. These conditions lead to an equation system that can be solved [10] resulting in the phase that the wave undergoes by propagating from the antenna in the plasma and back to the antenna [2]

$$\phi = \frac{4\pi f}{c}(z_a - a) + \frac{4\pi f}{c} \int_{z_c}^{a} n(z,f)dz - \frac{\pi}{2} \tag{2.50}$$

The first term represents the propagation in vacuum and the second term the phase due to the plasma. The correction factor $\pi/2$ accounts for the non-metallic character of the reflection in the plasma, and results from the existence of a reflection region instead of a reflection point [1].

2.2 The microwave reflectometry as a fusion plasma diagnostic

In 1961, it was suggested to use microwave reflectometry to measure electron density profiles in tokamak plasmas [11]. Since the delay time for the reflected signal is very small, in the range of a few nanosecond and is difficult to be accurately measured, it was proposed to measure the phase difference of the probing wave in relation to a reference wave. At the beginning only fixed frequency or very narrow band probing was used due to the technological limitations of the available sources. But investigating the electron density profile requires a large number of different probing frequencies. Some years later the advent of broadband swept microwave sources and the progresses made on the design of broadband microwave components, uncovered all the interesting possibilities of this technique. In 1982, the first swept frequency microwave reflectometry was proposed to measure the electron density profile of a fusion plasma in tokamaks [12]. The first electron density profiles measured by microwave reflectometry were obtained a few years later in the TFR [9] and JET [13] tokamaks. Over the last decade, major advances have been achieved and microwave reflectometry as become a valuable diagnostic tool, mainly due to the high temporal and spatial resolutions it provides, and to the relatively reduced machine access it requires, compared to other diagnostic techniques, like Interferometry or Thomson Scattering. Due to these advantages, microwave reflectometry is now considered one of the key microwave diagnostics for ITER, not only to measure the density profile but also as a complement to the magnetic diagnostics during long-pulse operation.

2.2.1 Accessibility regions

Until now we have been mainly considering the existence of a reflecting layer in the plasma, but the propagation of a wave in the plasma is also conditioned by the existence of resonance regions where the energy of the wave is totally absorbed, creating regions that are not accessible to the probing waves.

The ordinary mode cutoff

In section 2.1.1 it is shown the existence of a propagating ordinary mode (O-mode) that is not affected by the presence of the magnetic field, and the corresponding refractive index is given by equation (2.27). When the frequency of the wave is $f > f_{pe}(z)$ the refractive index is real and the wave can propagate in the plasma. On the other side when $f < f_{pe}(z)$ the refractive index becomes imaginary and the wave can no longer

propagate in the plasma and becomes evanescent. In the region where the refractive index becomes zero the wave is reflected and a critical density n_c can be defined that can be related to the probing frequency by:

$$f_c = \sqrt{\frac{n_c e^2}{4\pi^2 \varepsilon_o m_e}} \tag{2.51}$$

By sweeping the frequency of the probing wave we can recover the electron density profile. This frequency is plotted in figure 2.3.

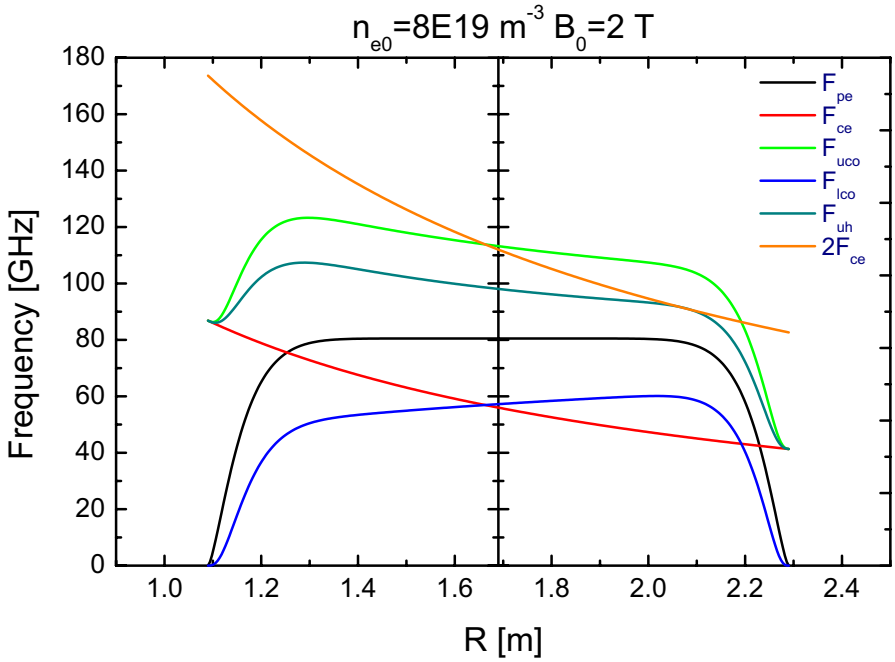

Figure 2.3: Accessibility regions. F_{pe} plasma frequency; F_{uco} and $F_{lco}$are the X-mode upper and lower cutoff frequency; F_{ce} and $2 \times F_{ce}$ are the electron cyclotron frequency and its second harmonic; F_{uh} is the upper hybrid resonance frequency.

The electron cyclotron frequency resonance can create regions that can not be probed by this mode when both frequencies are very close, and the thermal effects become important.

The extraordinary mode cutoff

In the extraordinary mode (X-mode) the reflection occurs for $n_X(z, f) = 0$. From equation (2.28) two solutions can be found

$$f_{uc} = \sqrt{f_{pe}^2 + \frac{f_{ce}^2}{4}} + \frac{f_{ce}}{2} \tag{2.52a}$$

$$f_{lc} = \sqrt{f_{pe}^2 + \frac{f_{ce}^2}{4}} - \frac{f_{ce}}{2} \tag{2.52b}$$

being one the upper cutoff and the other the lower cutoff. The resonances for this mode are the f_{ce} and the upper hybrid f_{uh} defined by:

$$f_{uh}^2 = f_{pe}^2 + f_{ce}^2 \tag{2.53}$$

The propagating regions for this mode are the one above f_{uc} and the other above f_{lc} but below f_{uh}. These frequencies are plotted in figure 2.3.

2.2.2 Basic configuration of a reflectometry system

A typical reflectometer set-up is presented in figure 2.4. It consists of an oscillator, a detector and transmission lines to guide the signal from the oscillator to the launching antenna and from the receiving antenna to the detector. A sample of the incident signal is used as a reference signal. To probe the complete density profile, a broadband sweepable source or many separate fixed frequency sources should be used. For present-day fusion devices, reflectometers with frequencies in the range of 18 to 110 GHz are utilized for probing the plasma in the O and X modes.

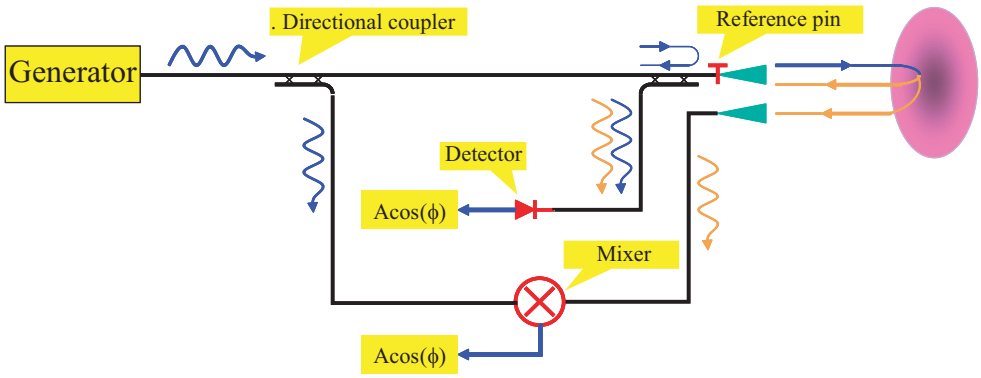

Figure 2.4: Typical reflectometer configuration.

2.2.3 Characteristic parameters of reflectometry systems

The accuracy of profile measurements can be characterized in terms of the parameters used in radar systems: range resolution, spatial sampling, precision. However, it has to be taken into account that the wave propagation in vacuum and in plasma are quite different, due to the fact that the phase delay in the plasma depends on the plasma refractive index along the propagation path, whereas in vacuum it depends solely on the distance from the antenna to the reflecting layer.

Range resolution

The optimal range resolution is the ability to distinguish between two different close targets, which in vacuum is expressed by:

$$\Delta R = \frac{c}{2\,\Delta F} = \frac{c\,\Delta\tau}{2} \tag{2.54}$$

with ΔF being the RF bandwidth and $\Delta\tau$ the width of the radar pulse in time delay measurements. Range resolution is essential to resolve the spacing between two adjacent plasma layers. In FM-CW radar systems, range resolution depends on the transmitted bandwidth, the processed overlap between the transmitted and received frequency sweeps, the receiver frequency resolution, and the frequency sweep linearity. Frequency sweep non-linearity is often the limiting factor in FM-CW radar range resolution. To obtain high resolution in vacuum ΔF should be made as large as possible; however, in the plasma ΔF is limited as different frequencies are reflected at different plasma positions depending on the shape of the density profile.

Range acuracy

The range acuracy parameter δR, characterizes the accuracy of each position measurement and depends on the signal to noise ratio, S/N, of the detected signal and the effective bandwidth β. It can be written as:

$$\delta R = \frac{c}{\beta\sqrt{2S/N}} \tag{2.55}$$

with $\beta^2 \approx 2B/\Delta\tau$, B is the video pulse bandwidth and $\Delta\tau$ is the pulse width. High accuracy implies both large β and S/N, but as the effective bandwidth depends on the RF bandwidth (see [14]) it cannot be increased significantly. The signal to noise ratio depends on the distance to the cut off layer (geometric attenuation), the curvature of the plasma refractive index surfaces, the shape of the density profile and plasma movements

as well as turbulence. The effect of plasma movements can be diminished to a certain extend with an adequate antenna design and turbulence effects can decrease by applying improved reflectometry techniques. Plasma geometry - density profile shape and fine structure - imposes requirements on spatial sampling.

2.2.4 Spatial sampling

The basic quantity to invert the density profile is:

$$\tau_g(F) = \frac{1}{2\pi}\frac{d\phi}{dF} \tag{2.56}$$

in the frequency range zero to F_α , where F_α is the frequency of the wave that is reflected at the highest density layer to be probed. The plasma and its fluctuations determines the k-spectrum of the $\tau_g(F)$ signal. According to the sampling theorem in order to avoid ambiguity due to aliasing, the plasma should be sampled at N locations separated by $\Delta r = 2\pi/k_m$. The wave number k_m is the maximum wave number in the k-spectrum of the $\tau_g(F)$ signal. In order to measure the detailed structure of the density profile and to avoid propagating errors in the inverted profile, k_m should be high enough, which implies both high number of measuring points and small Δr. To illustrated this situation we have simulated the use of narrowband and broadband probing in the presence of a density perturbation located around 42 cm. This perturbation varies according to [15]:

$$r_p(t) = w \cdot \left(\frac{1 + \cos\left(m\theta + \omega_{rot}t + \varphi\right)}{2}\right) \tag{2.57}$$

where w is the width of the island, ω_{rot} the frequency of rotation of the island and $m\theta$ and φ are the poloidal and toroidal angles. The model used is plotted in figure 2.5. The position of the point r_p evolves in time with equation (2.57), and a linear density profile is used between $r_p(t)$ and r_s, that is matched to a general parabolic profile. In this way we have a different profile for each time.

The group delay is calculated for narrowband (red) and broadband (green) (figure 2.6(a)) and the profile is inverted for the two techniques (figure 2.6(b)). One can see that if the narrowband reflectometry group delay includes the perturbation the profile never recovers from the error, but in the case of broadband the profile recovers after some time. This is due to the high spatial sampling of the broadband reflectometry, and the integration involved in the process of inverting the profile.

The value for Δr is limited to the theoretical thickness of the reflecting layer which for O-mode can be writen as [9]:

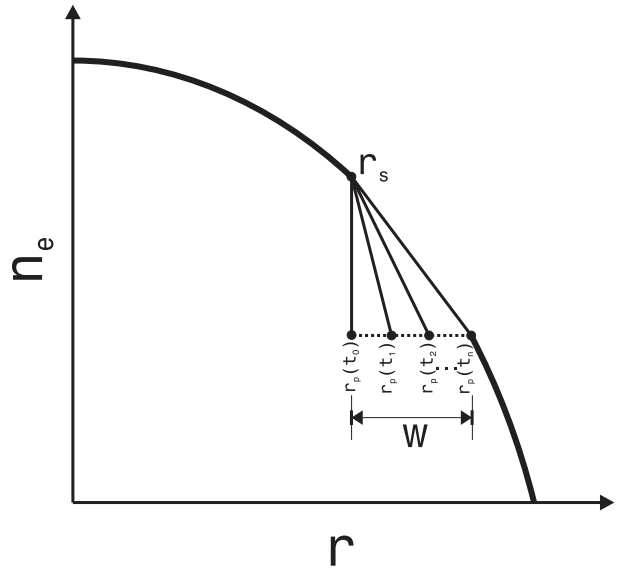

Figure 2.5: Model of the perturbation used in figure 2.6(a). The point r_p evolves in time with equation (2.57). A linear profile is considered between r_p and r_s.

$$\Delta x_c \simeq 15.64 \times 10^4 \left[\left(\frac{dn_e}{dx} \right)_{x=x_c} \right]^{-1/3} \tag{2.58}$$

2.2.5 Plasma turbulence

Plasma turbulence leads to diffraction and scattering of the probing microwaves which may cause significant decrease of the signal to noise ratio or even prevent any reflected signal to be detected. Temporal effects of turbulence can be significantly diminished by probing the complete density profile in time intervals smaller than the typical periods of plasma fluctuations. As will be discussed in section 2.3 each technique has its limits to time required to probe the plasma. However, no matter how fast the plasma can be probed spatial turbulence effects cannot be avoided. The spatial structure on the density distribution, which is an intrinsic effect of the fusion plasma, may change the cut off layer from a plane reflector to a lumpy surface made of small sub-reflectors. The interference of the contributions from each element can give a signal with strongly variable amplitude compared with frequency, just like a grating. A numerical analysis assuming a rippled reflecting surface shows that the attenuation can reach 45 dB making profile measurements very difficult [16]. In these cases heterodyne detection techniques with improved sensitivity can be a possible solution. In order to deal with the problem of plasma turbulence several radar techniques and different detection schemes have been developed, as presented in the following.

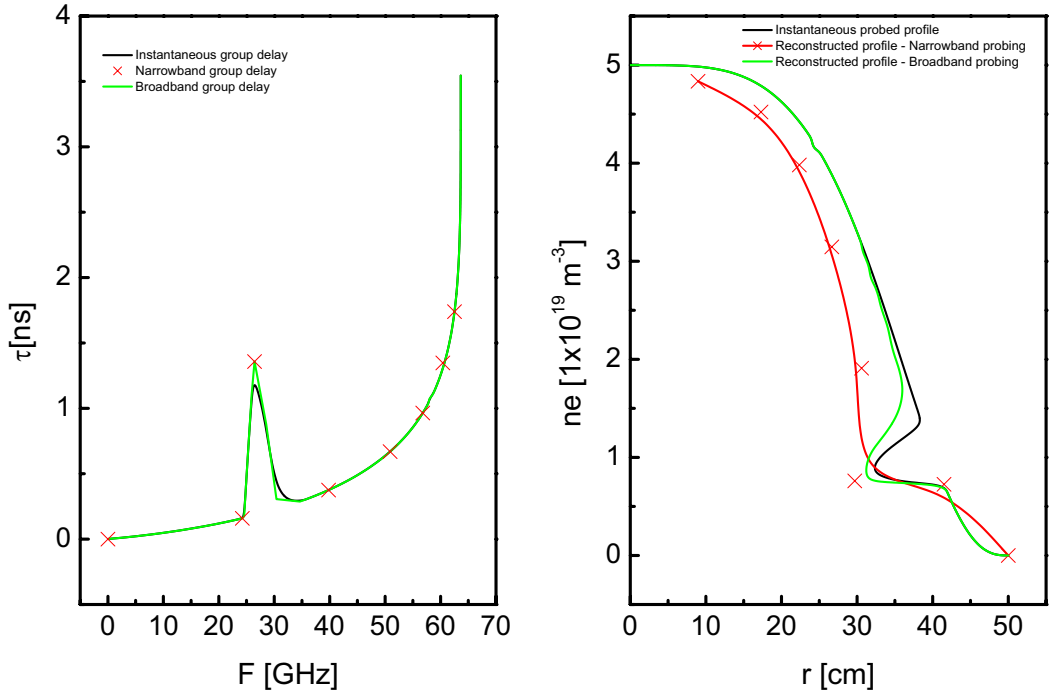

(a) Group delay. The black curve is the instantaneous group delay; red crosses is the narrowband group delay;green curve is the group delay from broadband reflectometry.

(b) Black curve is the instantaneous probed profile. Reconstructed electron density profiles for: narrowband red; broadband green.

Figure 2.6: Comparison between narrowband and broadband reflectometry in the presence of a density perturbation localized around r=42 cm.

2.2.6 Basic reflectometer detection techniques

Many detection techniques can be employed that determines the sensitivity and the information that can be obtained with the reflectometer, namely the possibility to measure or not phase and amplitude separately.

Single homodyne detection

The most simple detection scheme is the one shown in figure 2.4 that employs a single detector. The reference signal given by $V_R(t) = A_1 \sin(\omega t)$, and the signal reflected from the plasma, $V_P(t) = A_2 \sin(\omega t + \phi(t))$ are mixed on the detector. $\phi(t)$ is the phase change induced by the plasma and by the difference in optical path length between the reference path and the plasma path. The detector used in this scheme is mostly operated in the regime where the response is linear to the input power (squared-law detector). As the detector has a low-pass characteristic, all high frequency components are filtered out.

It is shown in section 3.2.5 that the output signal from the detector is then given by:

$$Video_{out}(t) = \frac{A_1^2(t) + A_2^2(t)}{2} + A_1 A_2(t) \cos(\phi(t)) \tag{2.59}$$

The measured signal in this detection scheme depends on both phase and amplitude of the reflected signal, meaning that the phase measurements are not unique. The amplitude of the signal will depend on the phase difference between the reference and the plasma signal.

When the single homodyne detection scheme is used for fluctuation measurements, the dependence of the detector output voltage on the cosine of the phase rather than on the phase itself, has to be taken into account in the signal interpretation.

Quadrature-phase detection

To measure the absolute phase difference between the plasma signal and the reference signal, two mixers can be combined into a so-called quadrature-phase detection scheme, as shown in figure 2.7.

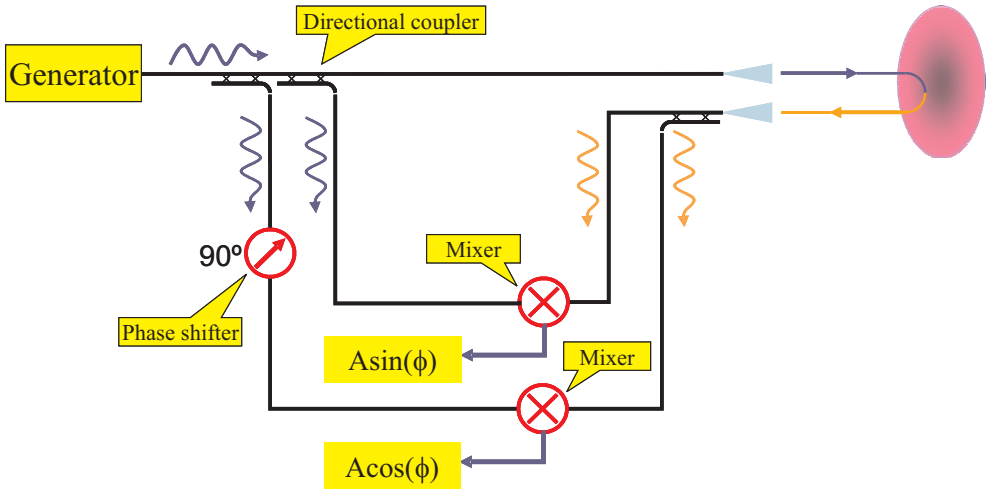

Figure 2.7: Quadrature-phase detection.

In this scheme the reference signal is split in two equal parts. Both parts are fed to the two mixers, one directly and the other after introducing an extra phase shift of $\pi/2$. The signal reflected from the plasma is also split in two equal parts with no extra phase

shift. The output signal of the two detectors will be:

$$VideoI_{out}(t) = \frac{A_1^2(t) + A_2^2(t)}{2} + A_1 A_2(t) \sin(\phi(t)) \quad (2.60a)$$

$$VideoQ_{out}(t) = \frac{A_1^2(t) + A_2^2(t)}{2} + A_1 A_2(t) \cos(\phi(t)) \quad (2.60b)$$

and the sine and cosine of the signal can be measured independently. The DC component in the two signals has to be removed before any calculation can be performed, reducing equations 2.60a and 2.60b to:

$$VideoI_{out}(t) = A_1 A_2(t) \sin(\phi(t)) \quad (2.61a)$$

$$VideoQ_{out}(t) = A_1 A_2(t) \cos(\phi(t)) \quad (2.61b)$$

The absolute power is given by the sum of the two squared signals, while the absolute phase can be calculated from the inverse tangent of the ratio of the two signals. For reliable operation of this detection scheme, balanced detectors having exactly the same power dependence have to be employed. A limitation to this system is the fact that the phase shift of $\pi/2$ is only valid for one frequency or frequencies which the wavelength is an multiple integer and so the operation in mode even in narrowband is not possible. The video bandwidth of the detectors can be very large, more than several megahertz. This makes this scheme very useful for fluctuation studies which are often extending into this frequency range.

Heterodyne detection

To increase the dynamic range of reflectometers, heterodyne detection techniques can be used. For this detection scheme, two oscillators are used, as in figure 2.8 [17]. One oscillator is used as a transmitting source, the other one as a reference source. The two oscillators are kept at a constant frequency difference, often by a phase lock loop (PLL). The signal from the reference oscillators is used as a local oscillator for a mixer. The signal from the other oscillator is fed to the RF-input of the mixer after undergoing an interaction with the plasma, resulting the IF_{Plasma} signal. The output power of the mixer (IF-port) depends linearly on the RF input power. The phase information in the RF signal is retained in the IF signal. For absolute phase measurements, a second mixer is used as a reference. On this reference mixer, signals from the transmitter and the reference oscillator are mixed before plasma interaction resulting the IF_{Ref} signal. These two signals can be fed to a quadrature detector like the one described before, but as the IF signal frequency is kept constant by the PLL, there are no limitations to the probing

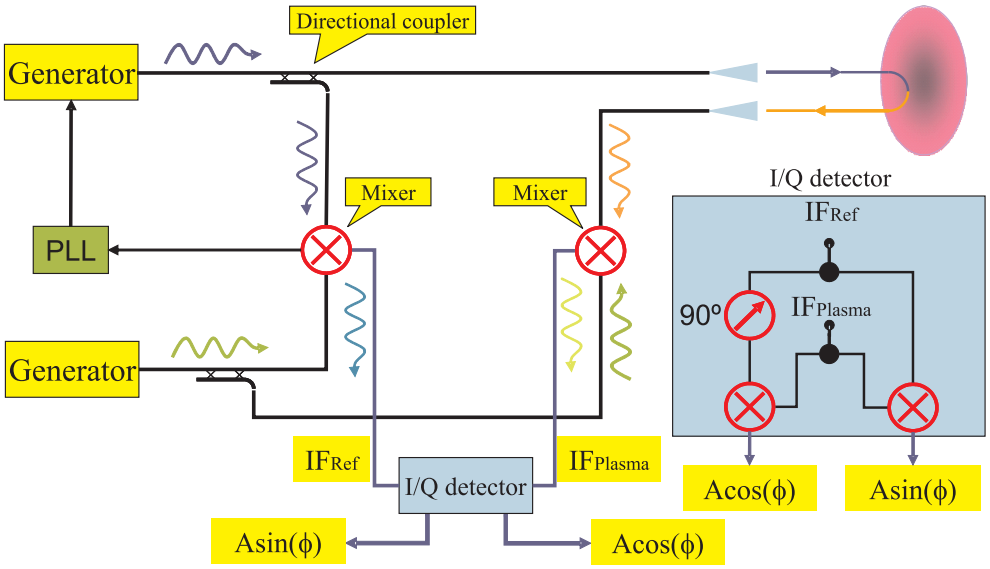

Figure 2.8: Heterodyne quadrature-phase detection.

source.

If the reference signal is obtained from a reflection induced on the transmission line, like if one uses a pin, the quadrature detector can no longer be used and a single detection scheme is used like the one shown in figure 2.9.

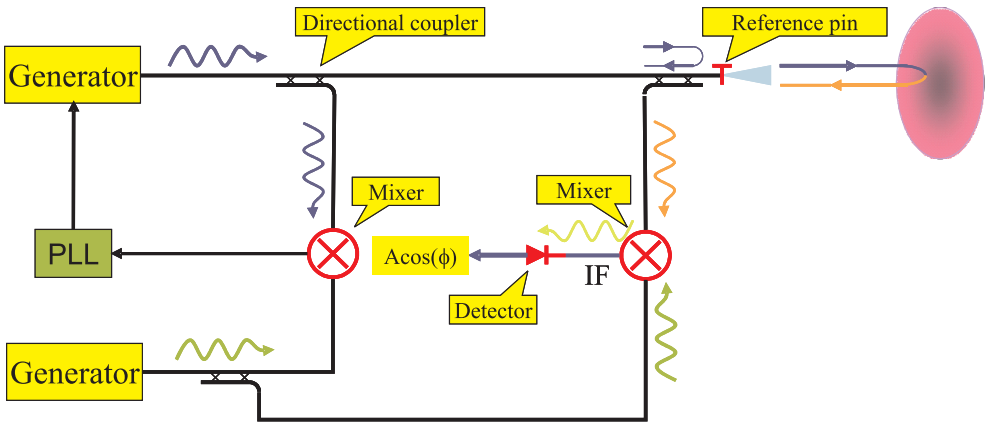

Figure 2.9: Heterodyne single-ended detection.

An alternative way of designing a heterodyne detection scheme is shown in [18].

The lowest detectable signal will depend on the noise temperature and bandwidth of the receiver system only, and can be as low as -130 dBm in a bandwith of 1 MHz. Using limiting amplifiers in the IF stage, it is possible to directly measure the phase difference between the reference signal and the plasma signal with a phase comparator. A major advantage of heterodyne detection is the extremely high dynamic range. A disadvantage

is that the phase comparator need a considerable time to restore from fringe jumps that occurs when the phase change becomes larger than 2π.

2.3 Reflectometry techniques for profile measurements

In parallel with the application of various detection schemes, different radar techniques were applied to measure the plasma.

2.3.1 Frequency modulation of a continuous wave

The basic principle is the measurement of the fringe frequency f_b resulting from the beating between the reference and the plasma signals. This give directly the group delay $\tau_g(t)$ needed for profile inversion according to:

$$f_b(t) = \tau_g(t)\,\frac{dF}{dt} \tag{2.62}$$

where dF/dt is the ing rate. Two approaches have been used: broadband and multiple narrow band swept systems. The broadband systems named FM-CW (Frequency Modulated Continuous Wave), uses continuous frequency over a wide range of frequencies in order to probe a large region of the plasma profile. The first FM-CW broadband profiles were obtained with a slow sweeping (5 ms) O-mode reflectometer on the TFR [9]. On the Petula-B tokamak the density profile has been measured in 200 μs with an X-mode reflectometer [19]. Using also the X-mode, profiles were obtained on the TJ-1 tokamak with a time resolution of 850 μs [20]. The ASDEX O-mode reflectometer used for the first time the much more stable Yttrium-iron garnet (YIG) solid state sources, with sweep times of 2 ms [21][22]. The O-mode reflectometer at Tore Supra could sweep in 1 ms [23][24]. The DIII-D X-mode reflectometer with a sweep time of 500 μs [25]. All these systems employed backward wave oscillators (BWO) as microwave sources with the exception of the ASDEX reflectometer.

In the narrowband approach several discrete frequencies are simultaneous swept over some small frequency range. The narrow band method was only implemented on JET [26][27][28], but experiments showed that broadband systems are more adequate due essentially to the continuous probing and the possibility to apply powerful digital data analysis techniques to the continuously recorded signal. One of the problems with discrete probing is illustrated in section 2.2.4, which is related to the lack of adequate spatial smapling.

FM radar systems are usually divided into channels corresponding to standard microwave bands but all frequencies can, in principle, be launched through a single waveguide at the cost of a more complicated system, namely using complex transmission lines. The detected signal, usually $A\cos\phi$ is recorded for further digital processing which is a great advantage because it is very flexible and data analysis can be adapted to the target density profile.

These first systems had the main limitation of the slow sweeping time resulting in a strong interference between the profile measurements and the plasma turbulence as well as profile deformations due to magnetic islands. To overcome this limitation ultrafast frequency sweeping ($10\,\mu s$ to $50\,\mu s$) has been developed first on ASDEX Upgrade [29][30], followed by the ones on DIII-D [31] and Tore Supra [32].

2.3.2 Pulse compression

This technic is applied in advanced military radar, and is based on the fact that is possible to decompose a pulse in time, in a set of n frequencies [33]. The principle of this method is launching in sequence a set of discrete waves towards the plasma contained within a total bandwidth ΔF. For each frequency F_i the amplitude and the phase, $A(F_i)$ and $\varphi(F_i)$, respectively, are measured by a heterodyne detection technique. An inverse Fourier transform is then applied to the complex array $A(F_i)\,e^{j\varphi(F_i)}$ in the frequency domain. The temporal response is, in principle, equivalent to an echo from a Gaussian shape pulse of duration $\Delta t = 1/\Delta F$. The method is very sensitive to spurious reflections, in particular from the transmission line and requires very stable and reproducible microwave sources. As the measurement can be performed in a time interval T greater than the reconstructed pulse width Δt and more energy is emitted from the source, a higher signal to noise ratio than in standard pulse radar is obtained and therefore better precision can be achieved. The improvement is expressed by the compression factor $T/\Delta t$. Pulse compression radar applied to reflectometry was only possible recently due to the advent of fast frequency synthesisers. As its application of this technique to reflectometry is very recent and only few experiments were made [34], more tests are needed to assess its operational limits and performance.

2.3.3 Amplitude modulation of a continuous wave

In both AM and dual frequency reflectometry systems the measured quantity is the time delay between reflected signals with closed spaced frequencies, launched simultaneously.

The time delay is derived directly from the differential phase, as follows:

$$\tau = \frac{1}{2\pi}\frac{\Delta\varphi}{f_m} \tag{2.63}$$

where f_m is the modulation frequency in the AM case and the frequency difference in the dual frequency method. In AM systems the modulation of microwave carrier generates a spectrum:

$$\begin{aligned} E(t) &= E_0\left[1 + m\cos\left(2\pi f_m t\right)\right]\cos\left(2\pi f t\right) \\ &= E_0\cos\left(2\pi f t\right) + \frac{1}{2}mE_0\cos\left[2\pi\left(f - f_m\right)\right]t + \frac{1}{2}mE_0\cos\left[2\pi\left(f + f_m\right)\right]t \end{aligned} \tag{2.64}$$

The phase delay between the modulating envelopes of the launched and reflected beams gives the required time delay. For the dual frequency systems, the phase delay between both frequencies is directly proportional to the time delay. Both systems can be swept in frequency to probe the complete density profile. Parasitic reflections can be a problem for these systems. In order to guarantee that plasma reflection is the dominant one, which is an essential requirement for accurate time delay measurements can be, in principle, achieved with separate emitting and receiving antennas. Amplitude modulation systems have been installed and operated in several machines like TJ-1 [35], TFTR [36], PBX-M [37] [38], W7-AS [39] and TdeV [40].

2.3.4 Pulse radar

This method is based on the standard radar technique where the time of flight of a short pulse reflected from the plasma is measured. In order to measure the complete density profile various pulses at different frequency carriers have to be launched in the plasma. Pulse radar reflectometry uses short microwave pulses with typically 1 ns duration. As the pulses are short its frequency spectrum has a considerable bandwidth. For a Gaussian pulse the spectrum has usually a Gaussian distribution with $f \pm \Delta f/2$, where f is equal to the inverse of the pulse width. With pulse radar each time of flight measurement is performed typically in a few ns which means that the plasma fluctuations are almost "frozen" during the time needed for the pulse to be reflected. But as spatial turbulence cannot be avoided the pulses suffer from broadening and non linearity which decrease significantly the accuracy of time delay measurements. Also pulse radar is not compatible with long lengths of fundamental wave guides leading to a significant broadening of the

probing pulses. Systems were implemented on RTP[41] [42], T-11M [43] and START [44].

2.3.5 Profile inversion

In section 2.1.3 we have derived the phase shift that a probing wave undergoes propagating in and out of the plasma. The result suggests two modes of operation: frequency sweeping and fixed frequency. When the frequency of the probing wave is swept over a broad range in a short time interval the position of the cutoff layer progresses radially to measure the density profile, $n_e(z)$. When the frequency of the wave is kept fixed a density layer of the plasma is probed over large time window and phase variations of the probing wave can be related to the local density fluctuations.

We can express the dependence of the refractive index in a more generic form, that is including the magnetic field and equation (2.50) becomes

$$\phi(t) = \frac{4\pi f(t)}{c} \int_{z_c}^{a} N\left[B(z,t), n_e(z,t), f(t)\right] dz - \frac{\pi}{2} \tag{2.65}$$

O-mode

By replacing the equation (2.27) for the O-mode refractive index in equation (2.65) we obtain:

$$\phi(t) = \frac{4\pi f(t)}{c} \int_{z_c}^{a} \sqrt{1 - \frac{f_{pe}^2(z)}{f^2(t)}} dz - \frac{\pi}{2} \tag{2.66}$$

To recover the position of the reflecting layer the integral equation (2.66) must be inverted. In this case it can be done by using the *Abel* inversion integral [9]:

$$z_c(f_c) = a - \frac{c}{2\pi^2} \int_0^{f_c} \frac{d\phi/df}{\sqrt{(f_c^2 - F^2)}} dF \tag{2.67}$$

We should note the relation of the layer position to the rate of variation of the phase to the probing frequency. This is the *group delay* and represents the delay that the wave undergoes when going in and out of the plasma, being defined by

$$\tau_g = \frac{1}{2\pi} \frac{d\phi(f)}{df} \tag{2.68}$$

X-mode

Due to the complexity of the refractive index for this mode (see equation (2.27)), it is not possible to analytical invert the phase integral. In these case a numerical algorithm must

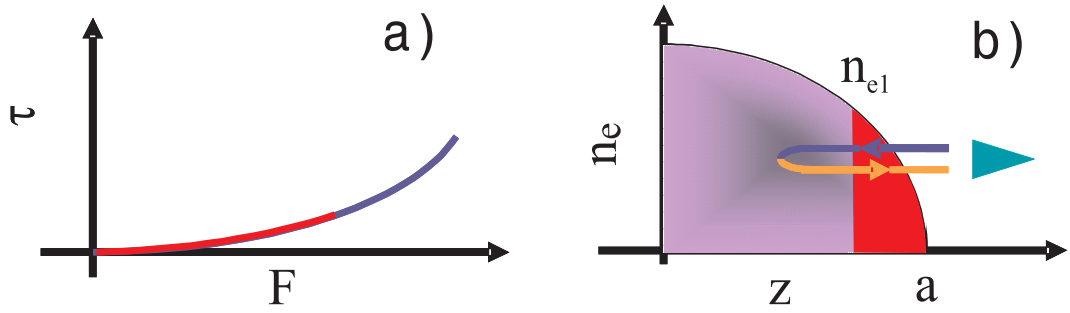

Figure 2.10: Non-probed profile regions. a) Schematic representation of the group delay; red line represents the added contribution to the measured group delay to initialise the density profile. b) Schematic representation of the electron density profile;n_{e1} is the first probed density.

be used to recover the position of the reflecting layer. One such algorithm was proposed by [45]. The process depends on the correct knowledge of the magnetic field and this is the weakness of this mode of operation. On the other side if the electron density profile is known we can use X-mode to derive the magnetic field profile.

Determination of the group delay

The correct determination of the *group delay* is the key issue for recovering *good* electron density profiles. But this is not an easy task due to the efect of plasma trubulence. Some of the described reflectometry techniques, like pulse radar, try to give directly this quantity, while others, like FM-CW, work on the recorded data and extract the group delay with more or less sophisticated data analysis techniques. In the ASDEX Upgrade reflectometer broadband system a time-frequency analysis is used, together with the *Floyd's* best-path algorithm applied to a graph whose nodes are taken from the spectrogram of the reflected signals [46].

Profile initialisation

From equation (2.67) we can see that the position of a reflecting layer is obtained by integrating the group delay, $\tau_g(f)$, of waves reflected at densities ranging from zero to the highest probed density. With O-mode frequencies below $\approx 10\,GHz$ can not be probed because the condition that validate the *WKB* approximation breaks.

It is therefor necessary to initialise the O-mode group delay (red line on figure 2.10 (a)) that corresponds to the non-measured profile, the red area in figure 2.10 (b).

Three approaches can can be used to solve this:

1. Data from other density diagnostics with relevant data on the profile edge.
2. X-mode data.

3. Use a model for the group delay that corresponds to the initial part of the plasma edge.

The last two options were used to process the ASDEX Upgrade data. The application of the X-mode data is described in section 4.4.

An initialisation model is proposed in [47]. The model uses as input the measured group delay and extrapolates the curve down to zero exponentially as

$$2\pi\tau(f) = A\left(\frac{f}{F_1}\right)^{2/s} \tag{2.69}$$

the parameters s and A are determined imposing boundary conditions. It is shown [47] that for densities of the order $10\times$ the first probed density the contribution from the initial model to the density profile is negligible. This initialisation method is being used in the routine evaluation of density profiles of the ASDEX Upgrade broadband reflectometer system.

References

[1] K. G. Budden. *Radio Waves in the Ionosphere*. Cambridge University Press, 1961.

[2] V. L. Ginzburg. *The Propagation of Electromagnetic Waves in Plasmas*. Pergamon Press, Second edition, 1970.

[3] K. C. Yeh and C. H. Liu. *Theory of Ionosferic Waves*. Academic Press, 1972.

[4] C. C. Johnson. *Field and wave electrodynamics*. McGraw-Hill, 1965.

[5] T. H. Stix. McGraw Hill Book Company, 1962.

[6] M. A. Heald and C. B. Wharton. *Plasma Diagnostics with Microwaves*. John Wiley & Sons, 1965.

[7] P. S. Epstein. Reflection of waves in an inhomogeous absorbing medium. In *Proceedings of the National Academy of Sciences*, volume 16, pages 627–637, October 1930.

[8] M. Abramovitz and A. Stegun. *Handbook of Mathematical Functions*. Dover Publications, 1965.

[9] F. Simonet. Measurement of electron density profile by microwave reflectometry on tokamaks. *Review of Scientific Instruments*, 56(5):664–669, 1985.

[10] F. Simonet. *Étude de la reflectométrie hyperfrequence en modes ordinaire et extraordinaire pour la mesure du profil radial et des fluctuations locales de la densité électronique dans les tokamaks*. PhD thesis, Université de Nancy I, 1985.

[11] A.I. Anisimov, N.I. Vinogradov, V.E. Goland, and B.P. Konstantinov. Method of investigating electron spatial distribution in a plasma. *Soviet Physics*, 5(9):939–1074, February 1961.

[12] A. Cavallo and R. Cano. Proposal for density profile measurements by reflectometry in large tokamaks. Technical Report EUR-CEA-FC-1337, EURATOM, January 1982.

[13] Amanda E. Hubard. *Measurement of Electron Density on JET by Microwave Reflectometry*. PhD thesis, Imperial College of Science and Technology, 1987.

[14] Merrill Skolnik. *Introduction to radar systems*. McGraw Hill Book Company, Second edition, 1981.

[15] M. E. Manso, A. Silva, F. Serra, J. Matias, J. Mendonça, H. Zohm, Klüber, and F. Söldner. Changes in the density profile due to the m=2 tearing mode in ASDEX. In *Proceedings on* 17^{th} *European Conference on Controlled Fusion and Plasma Heating*, pages 837–840. European Physical Society, 1990.

[16] G. D. Conway. Scattering of reflectometer signals from rippled surfaces. *Review of Scientific Instruments*, 64(10):2782–2788, October 1993.

[17] C. A. J. Hugenholtz. *Microwave Interferometer and Refelctometer Techniques for Thermonuclear Plasmas*. PhD thesis, Technische Universiteit Eindhoven, 1990.

[18] H.J. Hartfuss, T. Geist, and M. Hirsch. Heterodyne methods in millimetre wave plasma diagnostics with applications to ECE, interferometry and reflectometry. *Plasma Phys. Control. Fusion*, 39(11):1693–1769, November 1997.

[19] H. Bottollier-Curtet and G. Ichtchenko. Microwave reflectometry with the extraordinary mode on tokamaks: Determination of the electron density profile of petula-b. *Review of Scientific Instruments*, 58(4):539–546, April 1987.

[20] E. Anabitarte, E. G. Bustamante, M. Calderon, J. Sentiles, A. Navarro, and J. Sanchez. Determination of the electron density profile and its fluctuations by broad-band microwave reflectometry in the TJ-1 tokamak. *J. Phys. D: Appl. Phys.*, 21(9):1384–1390, September 1988.

[21] M. Manso, F. Serra, J. Barroso, J. Comprido, C. Teixeira, A. Monteiro, A. Silva, J. Neves, J. Pereira, L. Cupido, A. Cardoso, C. Costa, and A. Garrett. Broadband microwave reflectometry on ASDEX. In *Proceedings on* 16^{th} *European Conference on Controlled Fusion and Plasma Physics*, pages 1517–1520. European Physical Society, 1989.

[22] M. Manso, F. Serra, A. Silva, J. Matias, F. Nunes, J. Leitão, J. Mata, P. Varela, S. Vergamota, and F. Söldner. Localized density measurements on ASDEX using microwave reflectometry. In *Proceedings on* 17^{th} *European Conference on Controlled Fusion and Plasma Heating*, pages 1560–1563. European Physical Society, 1990.

[23] P. Millot and F. Simonet. A broadband microwave reflectometer for TORE SUPRA. In *Proceedings on* 14^{th} *European Conference on Controlled Fusion and Plasma Physics*, pages 1303–1305. European Physical Society, 1987.

[24] F. Clairet, M. Paume, and J. Chareau. Electron density profile measurements by microwave reflectometry on tore supra. In *Proceedings on* 21^{st} *European Conference on Controlled Fusion and Plasma Physics*, volume 18B, pages 1172–1175. European Physical Society, June 1994.

[25] E. J. Doyle, T. Lehecka, N. C. Luhmann Jr., W. A. Peebles, and DIII-D Group. X-mode broadband reflectometric density profile measurements on DIII-D. *Review of Scientific Instruments*, 61(10):2896–2898, October 1990.

[26] C. A. Hugenholtz and A. J. Putter. RR 86-170. Technical report, FOM–Instituut voor Plasmafysica Rijnhuizen, Nieuwegein, 1986.

[27] R. Prentice, A. E. Costley, J. A. Fessey, and A. E. Hubbard. Basic and advanced diagnostic techniques for fusion plasma. In *Proc. Course and Workshop*, page 451, Varenna, 1986. CEC.

[28] R. Prentice, A. C. C. Sips, J. A. Fessey, and A. E. Costley. First measurements of electron density profiles on JET with a multichannel reflectometer. In *Proceedings on* 17^{th} *European Conference on Controlled Fusion and Plasma Heating*, volume 14B, pages 1500–1503. European Physical Society, 1990.

[29] A. Silva, L. Cupido, M. Manso, F. Serra, F. X. Soeldner, P. Varela, C. Correia, C. Fernandes, C. Loureiro, A. Moreira, J. Neves, R. Pereira, J. Santos, and the ASDEX Upgrade Team. Fast sweep multiple broadband reflectometer for ASDEX Upgrade. In *Proceedings of the* 17^{th} *Symposium on Fusion Technology*, pages 747–750, Rome, 1993. North-Holland.

[30] A. Silva, M. E. Manso, P. Varela, F. Serra, Cupido, M. Albrecht, and F. X. Soeldner. First density measurements with microwave reflectometry on ASDEX Upgrade. In *Proceedings on* 20^{th} *European Conference on Controlled Fusion and Plasma Physics*, volume 17C, pages 1107–1110. European Physical Society, 1993.

[31] K. W. Kim, E. J. Doyle, T. L. Rhodes, W. A. Peebles, and C. L. Rettig. Development of a fast solid-state high-resolution density profile reflectometer system on the DIII-D tokamak. *Review of Scientific Instruments*, 68(1):466–469, January 1997.

[32] Ph. Moreau, F. Clairet, J.M. Chareau, M. Paume, and C. Laviron. Ultrafast frequency sweep heterodyne reflectometer on the tore supra tokamak. *Review of Scientific Instruments*, 71(1):74–81, January 2000.

[33] Merrill Skolnik. *Radar Handbook*. McGraw Hill Book Company, Second edition, 1991.

[34] C. Laviron, P. Millot, and R. Prentice. First experiments of pulse compression radar reflectometry for density measurements on JET plasmas. *Plasma Phys. Control. Fusion*, 37:975–987, 1995.

[35] E. de la Luna, V. Zhuravlev, B. Brañas, J. Sanchez, and T. Estrada. Density profile measurements by amplitude modulation reflectometry on the TJ-1 tokamak. In *Proceedings on* 20^{th} *European Conference on Controlled Fusion and Plasma Physics*, volume 17C, pages 1159–1162. European Physical Society, 1993.

[36] G.R. Hanson, J.B. Wilgen, T.S. Bigelow, I. Collazo, A.C. England, M. Murakami, D.A. Rasmussen, C.E. Thomas, J.R. Wilson, and H.K. Park. Microwave reflectometry for edge density profile measurements on tftr. *Plasma Phys. Control. Fusion*, 36:2073–2082, 1994.

[37] E. de la Luna, G. Hanson, J. Sanchez, J. B. Wilgen, V. A. Zhuravlev, M. Ono, and R Kaita. Edge density profile measurements by amplitude modulation reflectometry on PBX-M tokamak. *Plasma Phys. Control. Fusion*, 37:925–935, 1995.

[38] First results with amplitude modulation reflectometry on the PBX-M tokamak. Luna, e. de la and sanchez, j. and zhuravlev, v. a. and garcía-cortés, i. and hanson, g. r. and wilgen, j. b. and harris, j. h. and dunlap, j. and kaita, r. and leblanc, b. and tynan, g. r. and schmitz, l. and blush, l. and the PBX-M Team. *Review of Scientific Instruments*, 66(1):403–405, 1995.

[39] M. Hirsch. Amplitude modulated heterodyne reflectometer for density profile and density fluctuation profile measurements at W7-AS. *Review of Scientific Instruments*, 67(5):1807–1813, May 1996.

[40] D. Pinsonneault, B. Quirion, J. L. Lachambre, and C. Legros. Edge density profile measurements in TdeV using amplitude modulation reflectometry. *Review of Scientific Instruments*, 68(1):990–993, 1997.

[41] C.A.J. Hugenholtz and S.H. Heijnen. Pulse radar technique for reflectometry on thermonuclear plasmas. *Review of Scientific Instruments*, 62(4):1100–1101, April 1991.

[42] S. H. Heijnen, M. de Baar, M. J. van de Pol, and C. A. J. Hugenholtz. Measurements with a high resolution pulsed radar reflectometer. In *Proceedings on* 20^{th} *European Conference on Controlled Fusion and Plasma Physics*, volume 17C, pages 1143–1146. European Physical Society, 1993.

[43] V. F. Shevchenko, A. A. Petrov, V. G. Petrov, and U. A. Chaplygin. Plasma study at T-11M tokamak by microwave pulse radar reflectometer. In *Proceedings on* 20^{th} *European Conference on Controlled Fusion and Plasma Physics*, volume 17C, pages 1167–1170. European Physical Society, 1993.

[44] V. F. Shevchenko, T. Edlington, M. Gryaznevich, I. Jenkins, A. Sykes, J. Tomas, and M. J. Walsh. First density profile measurements by multifrequency pulse radar reflectometry in START. In *Proceedings on* 22^{nd} *European Conference on Controlled Fusion and Plasma Physics*, volume 19C, pages 421–424. European Physical Society, 1995.

[45] Hervé Bottolier-Curtet. *Réflectométrie hyperfréquence pour la determination de la densité électronique et de ses fluctuations sur le tokamak PETULA-B.* PhD thesis, Université de Paris-XI. Orsay, 1986.

[46] P. Varela. *Automatic time-frequency analysis for plasma density profile evaluation from microwave reflectometry.* PhD thesis, Universidade Técnica de Lisboa - Instituto Superior Técnico, 2002.

[47] P. Varela, M. E. Manso, A. Silva, J. Fernandes, and F. Silva. Initialization of plasma density profiles from reflectometry. *Review of Scientific Instruments*, 66(10):4937–4942, October 1995.

3 The ASDEX Upgrade microwave reflectometry system

3.1 System design

The design of the system has taken into account the physics studies to be performed with the diagnostic and its implementation in the machine aiming to the best performance. A key issue for investigation on ASDEX Upgrade with microwave reflectometry is the plasma electron density evolution at the edge region, namely the effect of fast transient phenomena such as Edge Localized Modes (ELMs), where reflectometry can give an important contribution due to its high spatial and temporal resolutions. The system aims at measuring electron density profiles with high spatial ($\leq 1cm$) and temporal resolutions ($\leq 50\mu s$) as well as fluctuations, with special focus in the peripheral and scrape-off layer (SOL) at the low field (LFS) and high field (HFS) plasma side. From the point of view of the hardware it is very important to minimize the access to the Tokamak vessel due to the severe space constrains. Among the different available reflectometry techniques (as described in chapter 2), we selected the broadband FM-CW technique because it offers continuous probing of the plasma and allows a posteriori data processing which can be adjusted to optimise automatically range resolution and average bandwidth for each plasma conditions. This option is also based on the successful measurements obtained previously in ASDEX with the FM-CW technique [1]. FM-CW systems requires fast sweeping to minimize the effect of plasma turbulence and while in ASDEX the sweeping time was 2 ms on ASDEX Upgrade a much faster sweep should be used due to the higher levels of turbulence expected in particular in regimes with high power heating.

Electromagnetic access

The plasma local parameters such as density and magnetic field determine the wave accessibility to the plasma. The waves are reflected at the cutoff frequencies where the plasma refractive index approaches zero value. The cutoff frequencies for ordinary and extraordinary waves are given by equations 2.51 and 2.52. A limiting factor for wave propagation

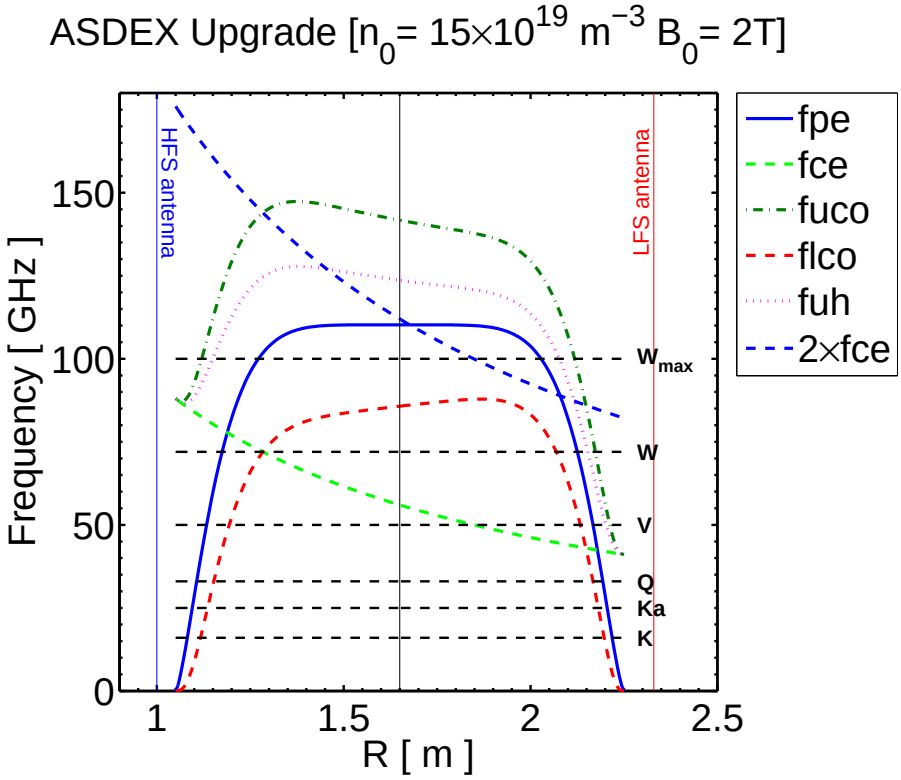

Figure 3.1: For a simulated plasma with $n_{e0} = 15 \times 10^{19} m^{-3}$ and $B_0 = 2T$ the curves show the radial dependence of: the O-mode cutoff (fpe); the X-mode upper (fuco) and lower (flco) cutoff; the upper hybrid resonance (fuh) and the electron cyclotron resonance (fce) and its second harmonic (2×fce). The frequency limits of the different standard millimetre-wave bands needed to cover the foreseen density ranges are also represented by the horizontal dash lines. Red and blue vertical lines show the position of the LFS and HFS antennas.

is the wave absorption that may occur close to the electron cyclotron frequency (fce) and its harmonics which may prevent the probing of some plasma regions. In order to study the wave accessibility we performed simulations studies for typical density and magnetic radial profiles of the ASDEX Upgrade plasma. In figure 3.1 we show the result of the simulations for a plasma with density at the center $n_{e0} = 15 \times 10^{19} m^{-3}$ and magnetic field of $B_0 = 2T$. From this study we could estimate the millimetre-wave bands required to probe the fusion plasma as presented both in figure 3.1 and table 3.1.

The plasma frequencies relevant to the access are displayed in figure 3.1: (i) plasma frequency (fpe) that corresponds to the O-mode cutoff; (ii) the X-mode upper (fuco) and lower (flco) cutoffs; (iii) the electron cyclotron resonance (fce) and its second harmonic (2×fce). When the probing frequency is close to fce or its harmonics absorption may occur but this corresponds to narrow regions of the plasma. Also, as the effect scales with the temperature it is only significant for high temperature scenarios. The upper hybrid resonance (fuh) may as well cause absorption of the X-mode probing waves for

some narrow region when the corresponding frequencies are very close to the incident frequency.

The frequency bands and modes of propagation of the diagnostic are presented in table 3.1.

Millimetre-wave band	LFS	HFS
K (16–25)	O	O
Ka (25–36)	O	O
Q (33–50)	O/X	O
V (50–72)	O/X	O
W (75–108)	O	–

Table 3.1: Chosen frequency domains of operation (O – O-mode, X – X-mode).

O-mode was selected to probe most part of the plasma column because it provides a better localization of the reflecting layers because the data depends solely on the plasma density (no need of the approximated magnetic data). The range of densities between $n_e = 0.32 \times 10^{19} m^{-3}$ and $n_e = 12.3 \times 10^{19} m^{-3}$ is probed with O-mode in the frequency range 16–100 GHz. The edge densities are covered with X-mode waves reflected in the upper cutoff corresponding to the frequency range 33 - 72 GHz. The use of the upper cutoff places the first reflected frequency around 40 GHz for a typical magnetic field $B_0 = 2T$, which allows to use X-mode data to initialise the LFS O-mode profiles, as demonstrated in section 4.4. Only the LFS was equipped with X-mode channels due mainly to the severe space constrains at the HFS. The frequency values of table 3.1 were adjusted to allow some frequency overlapping of consecutive millimetre-wave bands which facilitates the matching of data between consecutive bands.

Spatial resolution

The spatial resolution of the diagnostic is not easy to estimate due to the effect of plasma turbulence which in some situations can distort significantly the plasma reflected signal. A first estimate was obtained based on the density gradient at cutoff region and the probing wavelength negleting the effect of plasma turbulence. In O-mode operation and assuming a parabolic density profile with density at the centre $n_{e0} = 0.5 \times 10^{19} m^{-3}$, the estimated spatial resolution for the density profiles range typically from $\Delta x_p \leq 1\,cm$ at the edge region ($x/a \geq 0.8$) and $\Delta x_p \geq 1.5\,cm$ at the bulk plasma ($x/a \leq 0.3$). In the case of X-mode, with the same plasma parameters and for $B_0 = 2\,T$, the spatial resolution should be $\Delta x_p \approx 0.5\,cm$ for the edge and $\Delta x_p \approx 1\,cm$ for the bulk plasma. It should be noted

that the experimental results as shown in chapter 4 indicate that the spatial resolution at the edge is around 1 cm in spite of the effect of plasma turbulence.

For the central plasma region in the cases where the density profiles in the centre are rather flat (like in H-mode or low density plasmas), the width of the reflecting layer with O-mode probing can become quite large ($\Delta x \approx 5\,cm$). Additional difficulties are encountered in the probing of the plasma central region with O-mode due to the weakening of the plasma signals caused by the refractive effects associated with the high curvature of the refractive index surfaces.

Validity of the theoretical approach

The theoretical approach relies on the validity of the WKB approximation in the propagation region. The critical parameter for the WKB approximation is the ratio between the local inhomogeneity scale length (L) and $\lambda_0/2\pi$ where λ_0 is the wavelength in vacuum (see chapter 2). Several studies have been performed [2] [3], which show that significant departures from the WKB solution, (corresponding to reflections from density gradients exceeding 6° or 10%), occur only for $L \leq 0.6\lambda$.

As an example, for $L \approx 2\,cm$, near the plasma edge, the WKB solution is valid for probing waves with $\lambda \approx 3\,cm$ which corresponds to frequencies $F \approx 10\,GHz$; therefore densities below $n_e \approx 0.12 \times 10^{19} m^{-3}$ should not be probed with O-mode. As the probing frequencies of the ASDEX Upgrade reflectometer are always above $F = 16\,GHz$ (O-mode), this limitation will not pose any problem.

With X-mode the lowest frequencies are $F \geq 33\,GHz$, so $\lambda \approx 0.9\,cm$; in this case the WKB approximation should be satisfied for the all range of probed densities.

Therefore we can conclude that the theoretical approach (cold plasma approximation), is valid for the gradient and the edge regions of the ASDEX Upgrade plasma; in very flat density profiles the central plasma region may not be accessible with O-mode and X-mode should rather be utilized.

3.2 Experimental set-up

Our approach to the diagnostic design was to build a robust system with high performance in terms of spurious signals, optimised as much as possible for the several plasma configurations of the ASDEX Upgrade plasma, with flexible and high measuring capability. In order to meet those goals the following options were taken:(i) in vessel antennas; (ii) electronics placed close to the machine; (iii) fast swept operation for density profile measurements; (iv) full remote control of the diagnostic. The option to place the antennas

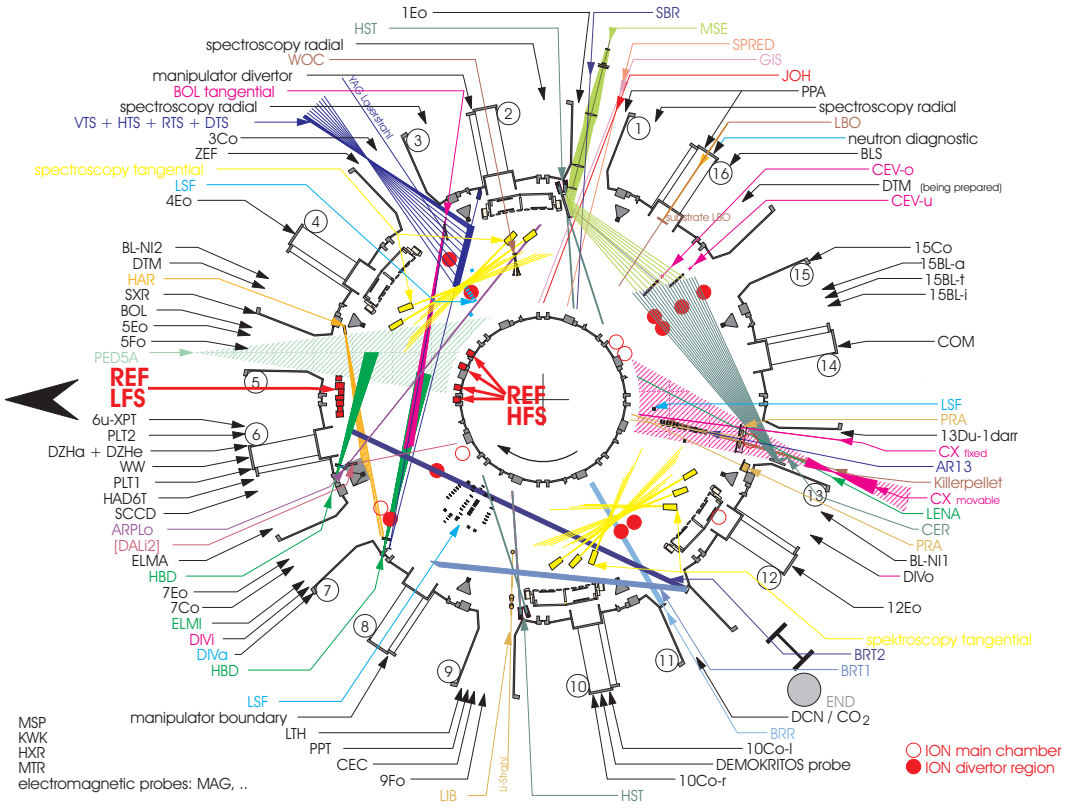

Figure 3.2: Diagram showing the in vessel assign positions to the reflectometry system around the torus (red small rectangular box). The LFS antennas are in sector 5. The HFS antennas are in sector 4 and 5.

inside the vessel guarantees that no obstacles are interposed between the antennas and the probed plasma, and therefore the risk of generating spurious signals is minimized. In order to keep transmission losses low, short waveguide paths ($\approx 3\,m$) where selected which was possible by placing the millimetre-wave sources and the detection sections in the torus hall close to vessel. This implies that all components are insensitive or have very little sensitivity to the strong magnetic stray field present in the torus hall.

All channels but the LFS W band are in fundamental waveguide to avoid higher order mode generation in the complex waveguide paths inside the vessel, in particular in the access to the HFS where the space constrains are more severe (see figure A.7). For the LFS W band we use a combination of oversized circular waveguides for the routing outside the vessel and fundamental waveguides inside the vessel. This arrangement keeps the transmission losses low and minimizes spurious reflections for the more complicated part of the routing.

Figure 3.2 presents the distribution of the different ASDEX Upgrade diagnostics. The in vessel positions assigned to the millimetre-wave reflectometry system, are displayed as well as those of other systems (ex: heating systems) along the torus. The figure reflects

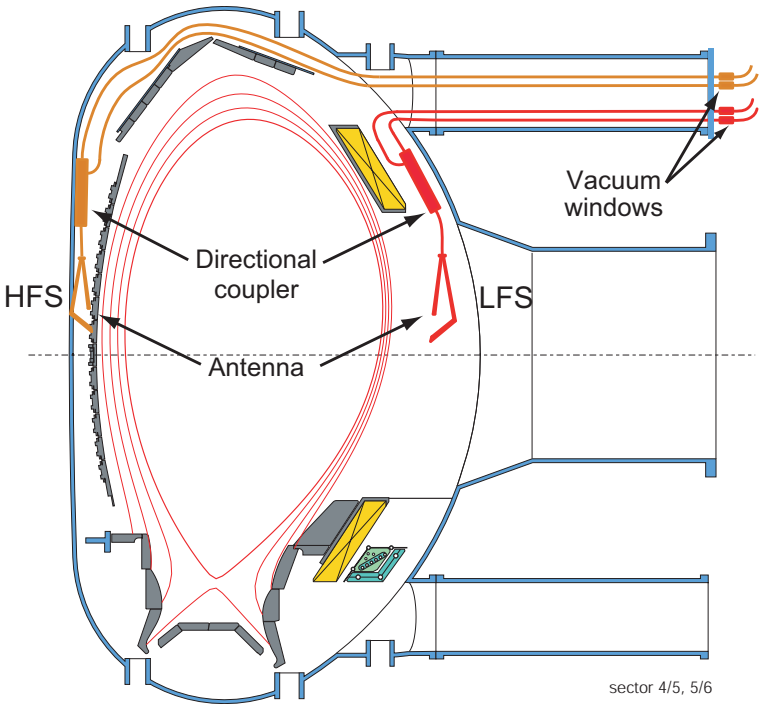

Figure 3.3: Cross-sectional view of the ASDEX Upgrade tokamak showing schematically the localization of hog-horn antennas and directional couplers in the high-field (HFS) and low-field sides (LFS).

the difficulties to find space for any diagnostic and to gain access to the plasma. In fact, although a fusion device is a big machine, access space is very reduced, due to the installation of cooling pipes, thermal, magnetic, and voltage sensors, and an ever growing number of diagnostics plus plasma heating systems, all of them *competing* for a better access to the plasma. The space limitations are more strict at the HFS and for this reason only four millimetre-wave bands could be installed with the sacrifice of the W band that should probe the highest densities and as a result the maximal probed density is limited to $n_e = 6.64 \times 10^{19} m^{-3}$.

The access of the waveguide bundle to the vessel is made by a C upper port situated in sector 6. From here they go down to the LFS antennas and directional couplers or up behind the upper divertor to gain access to the HFS. This can be seen schematically in figure 3.3. All waveguides are equipped with 0.3 mm thickness mica vacuum seals with the exception of the W band oversized waveguides in which 8 mm thickness quartz windows inclined to the *Brewster* angle are used. This configuration assures a low insertion loss; 0.1 to 0.2 dB for the mica windows; and $\leq$ 2 dB for the quartz windows.

Mono-static versus bi-static configuration

Single antenna (mono-static) instead of a double antenna (bi-static) arrangement was selected due to the advantages offered by the mono-static configuration: the signal reception is always optimised and the space needed for emission/reception is minimized. This is crucial for the HFS where the space constrains are most severe. High directivity directional couplers are used inside the vessel close to the antenna to efficiently separate the in- and out-going signals (DC in schematic annex A), and in addition to prevent the effect of spurious reflections from the vacuum windows (VW in schematic annex A) plus DC breaks (DB in schematic annex A). The DC breaks were included to guarantee galvanic isolation between the vessel and the cubical. The reference is generated by metallic pins placed close to each antenna flange and in this way the reflected and reference signals suffer identical phase shifts in the common path between the antenna and the detector, thereby cancelling the spurious phase contributions. The in-vessel reference has also another advantage which is to avoid the use of a compensation line that might introduce erroneous phase contributions due to thermal expansion and it would require a pre discharge calibration. Furthermore, the in-vessel reference reduces the signal beat frequency to the relevant plasma component minimizing the degradation of the ideal range resolution because it reduces the effective processed transmitted bandwidth [4] and is also less demanding for data acquisition. The disadvantage of this configuration comes from the possibility of the directional couplers being damaged after being exposed to high power radio frequency spurious radiation from auxiliary plasma heating systems, namely the *Electron Cyclotron Radio Frequency Heating* (ECRH), while it is not easy to effectively protect them.

With a bi-static configuration no directional couplers are required and therefore the system can be easily protected by installing in-line millimetre-wave switches. The disadvantages are: (i) at least two times of in-vessel space is required as compared to the mono-static configuration. This is a severe problem for the HFS and even could be a problem for the installation of the system at the LFS because the space assigned to broadband reflectometry is bounded by two ECRH launchers; (ii) it is more difficult to optimise the system in terms of reception; (iii) it needs an external delay line to generate the reference which implies that received and reference signals undergoes different paths and therefore could suffer different phase shifts due to thermal expansion, inducing phase errors.

Taking into account the above considerations and considering that at the time the diagnostic was designed the risk imposed by spurious radiation was minimal (later on the risk was significantly increased after the upgrade of the ECRH system) our option was to use a mono-static antenna arrangement with antenna and directional couplers inside the

vessel.

3.2.1 Antennas

Considering the successful results on ASDEX tokamak [1] we have decided to use focused hog-horn antennas in all the reflectometer channels probing the LFS and the HFS of the plasma, with the exception of the Q band X-mode channel in which a standard pyramidal horn is used, due to space limitations.

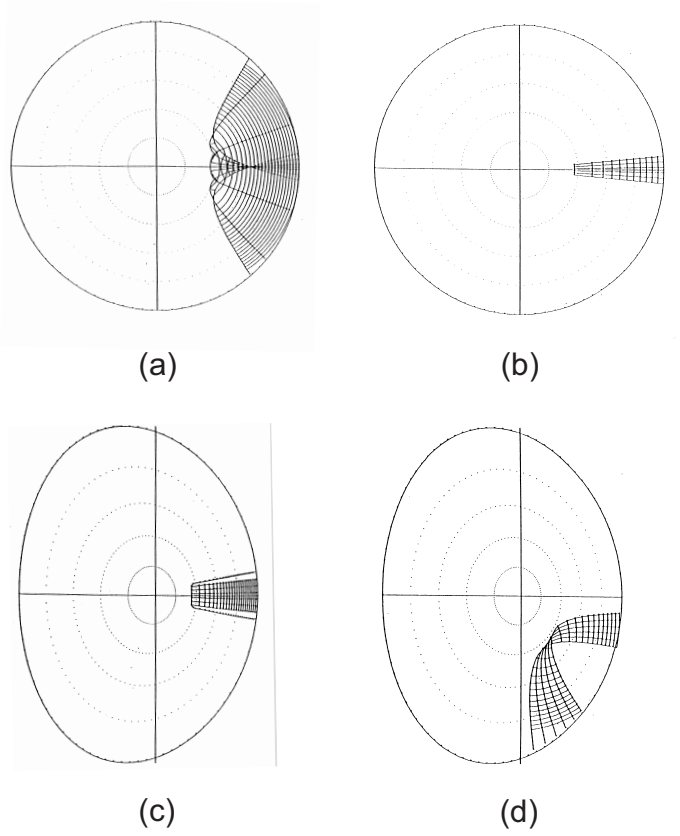

Figure 3.4: Ray tracing calculations for a typical plasma configurations: (a) Antenna focused behind the probing layer and (b) antenna focused beyond the probed layer; (c) Antenna at the plasma mid-plane and (d) and with vertical displacement of the plasma column of 10 cm.

Ray tracing studies[1] were performed to determine the focusing range and the localization of the antennas in both single null and double null experiments [6] [7]. Numerical results (see figure 3.4 a and b) indicate that the antennas: (i) should be focused beyond the probed layers, otherwise refraction occurs previous to the plasma cutoff causing unwanted divergence of the incident waves; (ii) should face the plasma mid-plane in both plasma

[1]Using a modified version of the RAYIC code [5] by A. Moreira.

geometries which implies different positioning for single null and double null configuration (see figure 3.4 c and d).

Taking in consideration the different plasma regions to be probed by the different millimetre-wave bands (see figure 3.1) and the results of the above study we have selected the focusing distance for each antenna as presented in table 3.2.

Frequency band	K		Ka		Q		V		W	
	LFS	HFS	LFS	HFS	LFS	HFS	LFS	HFS	LFS	HFS
Focusing dist. (cm)	30	30	40	40	40	40	50	50	50	-
Gain (dB)	20	20	28	20	25	25	27	27	25	-

Table 3.2: Focusing distance and gain value used in the design of each antenna.

The antennas are localized at optimised positions for a single null configuration (the most common configuration), at z=14 cm for the LFS and z=7 cm for the HFS close to the plasma mid-plane. The position of the different antennas is shown in figure A.6. The configuration of the antennas was later tested experimentally for different vertical plasma positions (as it will be shown in section 4.1) demonstrating the great tolerance of the diagnostics to vertical displacements of the plasma column.

Design of the antenna

Hog-horn antennas with elliptical focusing mirrors were first proposed for millimetre-wave plasma diagnostics by Moresco [8]. A hog-horn antenna has two main parts (figure 3.5): a pyramidal horn (in blue) and an elliptical reflecting mirror (orange). Pyramidal horn antennas are aperture antennas obtained by simultaneously enlarging the original wave guide along the electric field and magnetic field planes [9]. These antennas are specially suitable for applications such as plasma diagnostics, where high concentration of energy in a small region and high directivity in both main planes, are required. The *Fraunhofer* zone (far field) of those antennas is situated for distances from the aperture in the order of $R > 2\,D^2/\lambda$ (only if $D > \lambda$), where D is the maximum linear dimension of the antenna aperture. From the theory of aperture antennas the beam width is in the order of $2\,\lambda/D$, and the probing zone must be in the *Fraunhofer* zone (distance zone) in order to avoid phase interference. Therefore the beam width becomes $bw \approx 2D^2/\lambda \tan(2\lambda/D)$, and considering the condition that $D > \lambda$ then $\tan(2\lambda/D) \approx (2\lambda/D)$. This implies that the beam width is four times as large as the antenna aperture dimension, which would limit the space resolution of the measurements [8]. To improve this resolution, the *Fraunhofer* zone can be brought closer to the antenna by decreasing its dimensions (D). However, this decrease would cause a degradation of the radiation diagram: the beam width would be small at

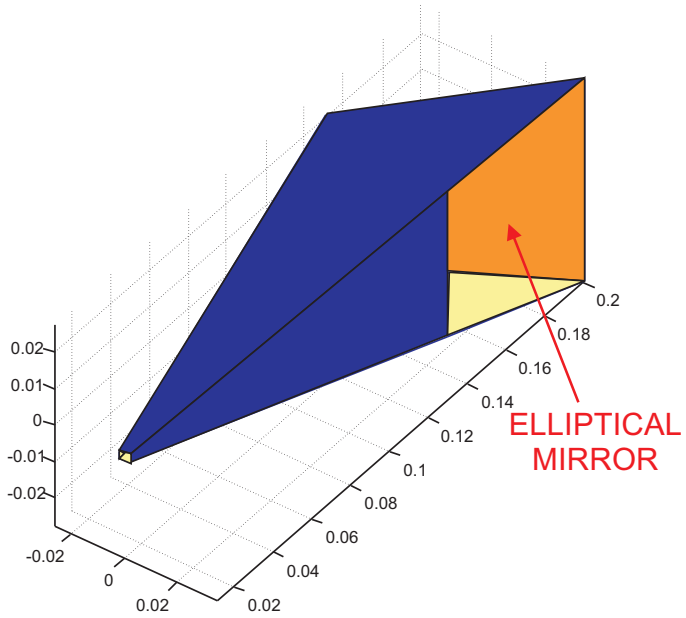

Figure 3.5: Sketch of an Hog-horn antenna.

the beginning of the probing zone but would broaden as the distance increases, leading to a gain reduction. Hence, it may occur that the required values by the experiments for the beam width plus divergence angle of the main lobe are not compatible with the far field condition. High space resolution and small beam divergence are opposite requirements that cannot be met by simple aperture antennas. A typical solution is to use focalised antennas which can improve the space resolution by bringing the far-field region closer to the antenna, within the plasma probing distance.

There are two main approaches to achieve the focusing effect: lenses and reflecting mirrors. For plasma diagnostics with antennas inside the fusion vessel, as in the reflectometry system on ASDEX Upgrade, the use of lenses is not appropriate because the dielectric material utilized in the lenses is likely to be coated by plasma impurities. This is why focused hog-horn antennas are a better approach.

Hog-horn antennas has significant advantages for plasma diagnostic as they reproduce, at their focal point, the same characteristics (gain, directivity, beam width, etc) of the far field zone of a non-focalized horn antenna with the same aperture dimensions.

The ellipsoid which contains the mirror of the antenna is obtained by turning the generating ellipse around the axis that passes through its focal points. It is known, from geometrical optics that this surface concentrates in one of its focal points, every ray that leaves the other focal point and all these rays travel the same distance. Thus, to determine the geometrical focal point of the antenna, the feed of the pyramidal horn is coincidental with one of the focal points of the ellipsoid. The horn then acts as a primary source for

the reflecting mirror (figure 3.6).

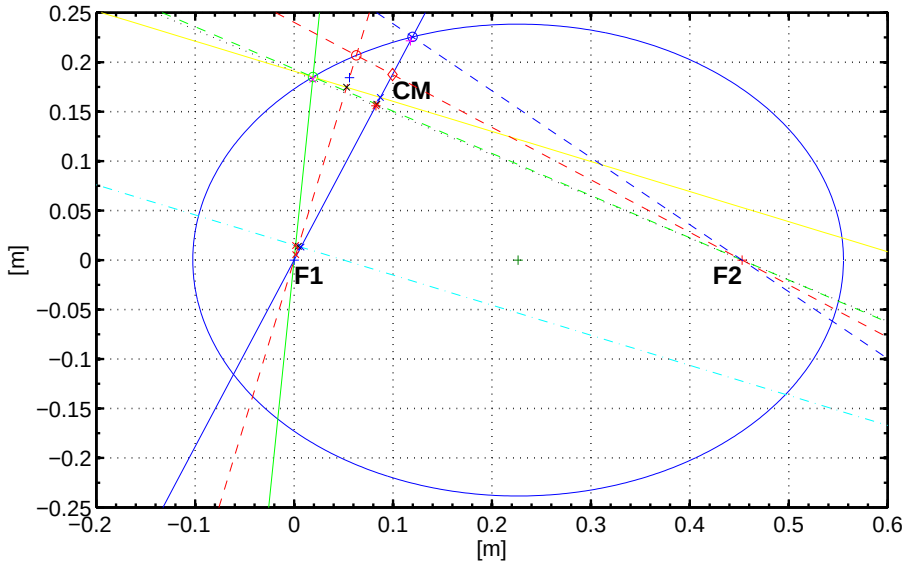

Figure 3.6: Schematic construction of an hog-horn antenna. **F1** and **F2** are the focus of the ellipsoid. **CM** is the projection of the central point of the mouth of the pyramidal horn in the mouth of the hog-horn. The antenna focal distance is defined as the distance between **CM** and **F2**.

A first design of the antennas for the ASDEX Upgrade diagnostic was performed as described in [10]. The software developed in that work, however, revealed some strong limitations and a new code was written that was able to fulfill the experimental requirements: focal distance limited to some tenths of a meter plus the size of the antenna limited to two tenths of a meter (to meet the space limitations mainly at the HFS). This new code that was written using *Matlab*© calculates first a standard gain horn having as input a selected gain value and the dimensions of the feeding waveguide in order to determine an optimum horn taper for each frequency band. The associated ellipsoid mirror is obtained using a geometric procedure that takes into consideration the required focal distance and meets the condition that the line from **CM** (projection in the antenna mouth of the central point of the optimum gain pyramidal horn figure 3.6) to **F2** is perpendicular to the mouth of the hog-horn antenna. The antenna focal distance is the distance between these two points. A file is then generated with the data for construction to input into a *CAD* program. The programme evaluates the electrical field phase and amplitude distributions at the antenna mouth. The radiation diagram is evaluated using a radiation pattern code for rectangular apertures *ABRECT*.

Optimum gain pyramidal horn. The calculations follows the design procedure described in [9]. The desired gain and the dimensions a and b of the rectangular feed

waveguide are known. The remaining dimensions (a_1, b_1, ρ_e, ρ_h, p_e *and* p_h) of the pyramidal horn can be determined (see figure 3.7), leading to the optimum gain horn. The

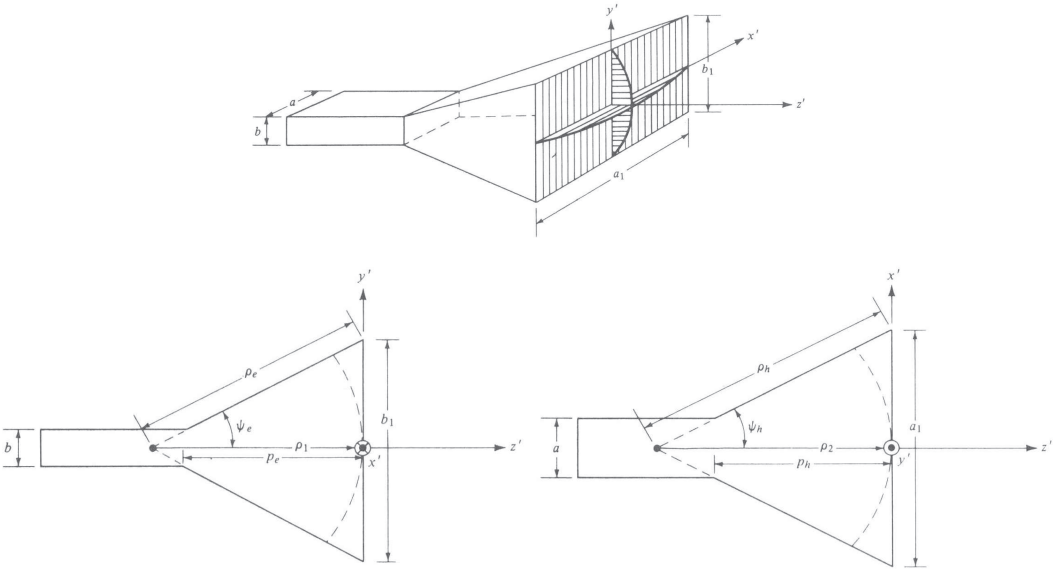

Figure 3.7: Pyramidal horn and the coordinate system [*Balanis*].

design equations are derived by selecting in a first step the values of a_1 and b_1 that lead, respectively to the optimum directivities for the E- and H-plane sectoral horns. For a pyramidal horn to be physically realizable p_e and p_h must be equal which leads to:

$$\left(\sqrt{2\chi} - \frac{b}{\lambda}\right)^2 (2\chi - 1) = \left(\frac{G_0}{2\pi}\sqrt{\frac{3}{2\pi}}\frac{1}{\sqrt{\chi}} - \frac{a}{\lambda}\right)^2 \left(\frac{G_0^2}{6\pi^3}\frac{1}{\chi} - 1\right) \tag{3.1a}$$

$$\frac{\rho_e}{\lambda} = \chi \tag{3.1b}$$

$$\frac{\rho_h}{\lambda} = \frac{G_0^2}{8\pi^3}\left(\frac{1}{\chi}\right) \tag{3.1c}$$

First the value of χ that satisfies 3.1a is found by a numerical process which uses as a first guess $\chi_1 = G_0/\left(2\pi\sqrt{2\pi}\right)$. With the value of χ we use 3.1b and 3.1c to find ρ_e and ρ_h, respectively. We can now find a_1 and b_1 using 3.2a and 3.2b.

$$a_1 = \sqrt{3\lambda\rho_2} \cong \sqrt{3\lambda\rho_h} = \frac{G_0}{2\pi}\sqrt{\frac{3}{2\pi\chi}}\lambda \tag{3.2a}$$

$$b_1 = \sqrt{2\lambda\rho_1} \cong \sqrt{2\lambda\rho_h} = \sqrt{2\chi}\lambda \tag{3.2b}$$

The last missing values, p_e and p_h, can be found from equations 3.3a and 3.3b.

$$p_e = (b_1 - b)\left[\left(\frac{\rho_e}{b_1}\right)^2 - \frac{1}{4}\right]^{1/2} \tag{3.3a}$$

$$p_h = (a_1 - a)\left[\left(\frac{\rho_h}{a_1}\right)^2 - \frac{1}{4}\right]^{1/2} \tag{3.3b}$$

The elliptical mirror. Having the optimal gain pyramidal horn designed the second step is to determine the reflecting elliptical mirror. Since the reflecting mirror is a piece of a revolution ellipsoid surface, in the ellipsoid equation 3.4 we have $b = c$, and all the points of the surface can be found by spinning a 2D ellipse, with parameters a and b, around the **x** axis.

$$\frac{(x - x_0)^2}{a^2} + \frac{(y - y_0)^2}{b^2} + \frac{(z - z_0)^2}{c^2} = 1 \tag{3.4}$$

The ellipsoid has two essential points: the focus points **F1**(-c,0,0) and **F2**(c,0,0) with $c = \sqrt{a^2 - b^2}$ for $a > b$. A well known propriety of this conical surface states that the sum of the distances d1 and d2 from any point in the surface to **F1** and **F2** respectively, is constant. This means that all the rays propagating from the focus point **F1** towards any point of the ellipsoid shaped mirror are reflected at the second focusing point **F2** and travel the same distance. Keeping this geometrical rule in mind and making the feed of a pyramidal horn coincidental with one of the focus points, we guarantee that all rays launched from taper and reflected in the mirror will reach the other focus point and travel the same distance. Therefore, all rays will arrive at the focus point in phase. Notice that the feeding point is the point where the four ends of the taper would intercept each other. It is a virtual point situated somewhere inside the waveguide attached to the antenna.

Knowing the required position of the second focus point (the actual antenna focusing point), an ellipsoid solution can be found. To do this some other conditions need to be met. One of the edges of the pyramidal horn mouth (bounded by points **A** and **B** in figure 3.8) is always coincidental with the ellipsoid (point **A** in figure 3.8) while the remainder of the horn is extended until it intercepts the ellipsoid, point **C**. As previously mentioned it is crucial that the centre ray (the dashed red line in figure 3.8) that goes trough **CM** is always perpendicular to the hog-horn mouth (bounded by points **D** and **C** in figure 3.8) because it is easier to adjust the antenna at its operating position. We should note that the hog-horn mouth is defined by points **C** and **D** and not by **B** and **C**. The gap between **B** and **D** gives a safety margin of 1 cm to enable the propagation of all rays reflected by the mirror.

At this point the program creates a file with a set of construction points like the

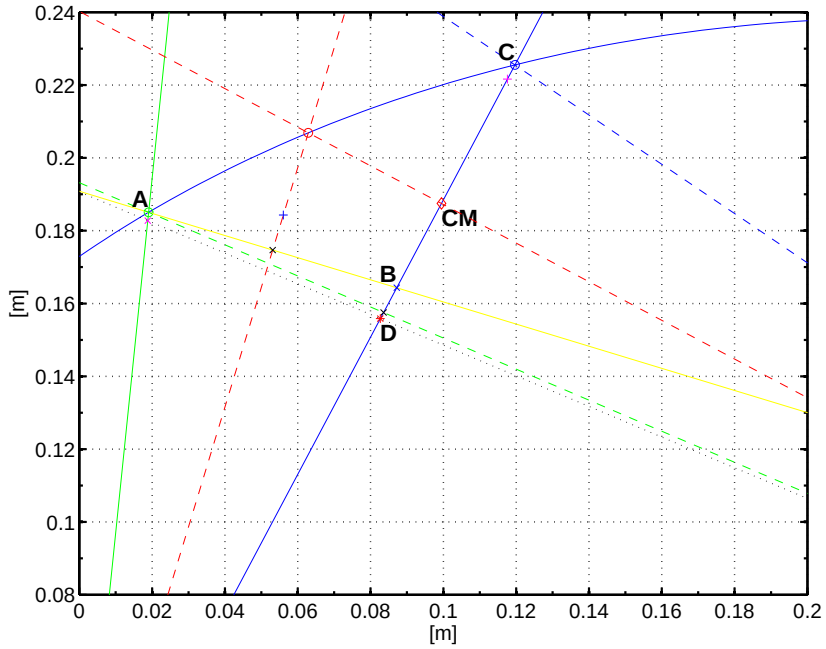

Figure 3.8: Schematic detail of the region where the taper intercepts the ellipsoid mirror. The **BD** segment of the taper is removed to unblock all reflected rays.

ones shown in figure 3.9 together with the ellipsoid equation, that can be used by a *CAD* program to generate the blue prints of the antenna.

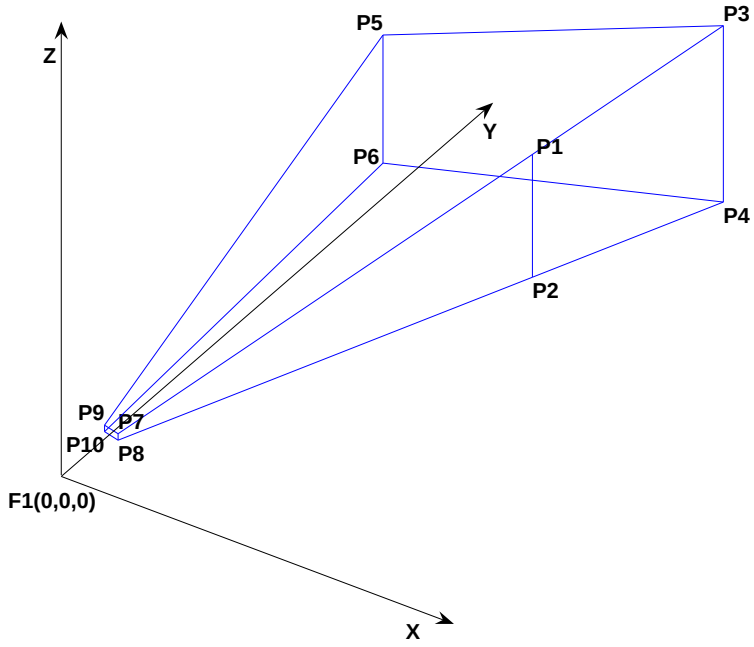

Figure 3.9: Set of construction points and used geometry.

Antenna mouth electrical field distribution and the radiation patterns. Once the antenna is designed, it is necessary to find the amplitude and phase distributions at the hog-horn mouth. After the electric field distribution is known it is possible to determine the far-field radiation characteristics of the antenna. A way of obtaining the far-field radiation pattern is by using a ray-tracing technique.

To find the field amplitude distribution at the hog-horn mouth we create a matrix with the electric field amplitude at the optimal gain pyramidal horn mouth (taper). Each point in that matrix is related with a specific point in space somewhere in the plane defined by the taper mouth. For fundamental mode horn antenna the field amplitude follows a cosine distribution of the type:

$$E = E_0 \cos\left(\pi \frac{x}{a_1}\right) \tag{3.5}$$

A set of rays is launched from the feed point **F1** passing through each point associated with an electric field amplitude value in the matrix. In this way a field value is attributed to each ray. All rays will be reflected by the mirror surface into the antenna focusing point **F2**. The interception of the reflected rays with the plane defined by the hog-horn opening results in a series of new points. To each of these new points a field amplitude value is attributed according to the ray that originated it.

As all the rays at both focusing points are in phase in order to obtain the phase distribution we applied the ray-tracing method starting from **F2** which easy the computation. The considered set of rays launched from **F2** are those that corresponds to the previously determined points at the hog-horn mouth. These rays will travel different distances until they intercept the hog-horn mouth plane. The centre ray is the one with the shortest path. The phase associated with each point of the antenna mouth can be found by multiplying the propagation constant, **k** (vacuum propagation), by the difference in the path lengths, using the centre ray as the reference. This implies that points near the edges of the hog-horn mouth have greater phase shifts as they are further away from **F2**.

The *ABRECT* uses a matrix with equally spaced complex field values over a rectangular opening to calculate the radiation pattern. Linear surface interpolation along with several coordinate transformations is used to create a matrix with the necessary requirements. Because the hog-horn aperture is not rectangular the opening was bounded by the smallest possible rectangle and the gaps filled in with zeros. This distortion of the antenna mouth creates phase errors that are responsible for the observed shift of the maximum of the H-plane radiation pattern in figures A.9 to A.18. Table 3.3 resume the estimated half power beam width for the several antennas.

Frequency band	K		Ka		Q		V		W	
	LFS	HFS	LFS	HFS	LFS	HFS	LFS	HFS	LFS	HFS
Beam Width (°)	15	15	8	12	9	9	8	8	9	-
Gain (dB)	20	20	28	20	25	25	27	27	25	-

Table 3.3: Half power beam width for each antenna.

The adopted method provides a reasonable estimation of the far-field radiation pattern. Some error sources can be identified: this technique is based on geometric optics so the error increases when the frequency decreases; it does not account for diffraction effects or propagation modes besides the ones inside the taper. Antenna measurements performed in an anechoic chamber that would provide the experimental radiation diagram were not possible due to the short time between the construction of the antennas and its installation in the tokamak. However, the experimental results with plasma demonstrates that the antenna design is well adapted to the target plasmas even in the cases where the plasma column is displaced vertically and refraction effects are more severe than assumed in the numerical study.

The reference pin

As previously discussed the mono-static configuration implies that a reference signal is obtained close to the antenna. The set-up that provides the reference signal should be capable of reflecting 10 to 20 % of the incident waves over each complete frequency band (broadband set-up). Several materials (metallic, dielectric) and different configurations (pins, slots, round or flat) were tested. The best results were obtained with a metallic pin crossing the smallest waveguide dimension, aligned with the maximum of the electric field inside the waveguide for the fundamental mode TE_{10}. Different thickness were tested and the configuration which improves the frequency response flatness proofed to be around 25 % of the maximum dimension of the waveguide. Thinner pins tend to have higher reflection for the higher frequencies. By changing the penetration deep of the pin it is possible to finally adjust the reflected power.

A simulation performed with the *HFSS* code confirmed the experimental finding of the optimal thickness of 27 % and the values for the pin penetration: 28 % of the waveguide height for a -10 dB reflection and 11.5 % for a -20 dB reflection [11].

Reference pins were installed in all the antennas close to the waveguide connecting flange and were adjusted for optimised reflection. An example can be seen in figure A.7.

In-vessel instalation

The antennas and directional couplers where installed at their assigned in-vessel positions in sector 5 for the LFS and in sector 4 and 5 for the HFS. The antennas, directional couplers and waveguides are isolated from the vessel walls with *Kapton film* and ceramics, with the exception of the waveguides inside the C port. On every pair of waveguides a DC break was inserted. With these procedures we try to avoid any possible ground loops and to minimise the efect of *Eddy Currents* that can destroy both the waveguides and the millimetre-wave components inside the vessel. This can be clear seen in figure A.7 that shows the HFS setup for the K and Ka bands. The HFS is protected by the vessel heat shield tiles and the antennas view the plasma through small apertures specially made on the heat shield (left side figure A.7). The LFS is protected by a special construction that includes a set of carbon tiles (see figure A.8).

The radial position of the antennas mouth in relation to the vessel centre is resumed in table 3.4.

Frequency band	Position LFS [m]	Position HFS [m]	Position X [m]
K	2.375	1.001	-
Ka	2.328	0.989	-
Q	2.365	0.991	2.375
V	2.374	0.987	2.365
W	2.341	-	-

Table 3.4: Antennas mouth position in relation to the vessel centre.

3.2.2 Microwave sources

Solid state oscillators such as the Yttrium-iron garnet (YIG) [12] have been first used in reflectometry on ASDEX with much better results than previously utilized BWO oscillators [1] less stable and with higher noise level. In the ASDEX Upgrade reflectometry diagnostic we use for the first time Hyperabruct Varactor-Tuned Oscillators (HTO) [12], in the range 8 to 18 GHz, together with active and passive frequency multipliers to obtain the signals at the required frequency range: 16 to 100 GHz. This arrangement is described in table 3.5.

In figure 3.10 it is depicted the output frequency versus tuning voltage (in red) for one of the used HTO; the typical non linear frequency characteristic of this devices is displayed. The HTO output power versus tuning voltage is also plotted in figure 3.10 (in blue) exhibiting a large variation. This effect is reduced at the signals send to the

Frequency band	1^{st} Frequency [GHz]	Frequency Multiplier	Final Frequency [GHz]
K (16–25)	8–12.4	×2 A	16–24.8
Ka (25–36)	12.4–18	×2 A	24.8–36
Q (33–50)	8–12.4	×2 A ×2 A	32–49.6
V (50–72)	12.4–18	×2 A ×2 P	49.6–72
W (72–100)	12.4–18	×2 A ×3 PAM	74.4–108

Table 3.5: The HTO are only available up to 18 GHz and a scheme of frequency multipliers is used to generate the required probing frequencies. A–active multiplication; P–passive multiplication; PAM–passive multiplication with millimetre-wave power amplifier.

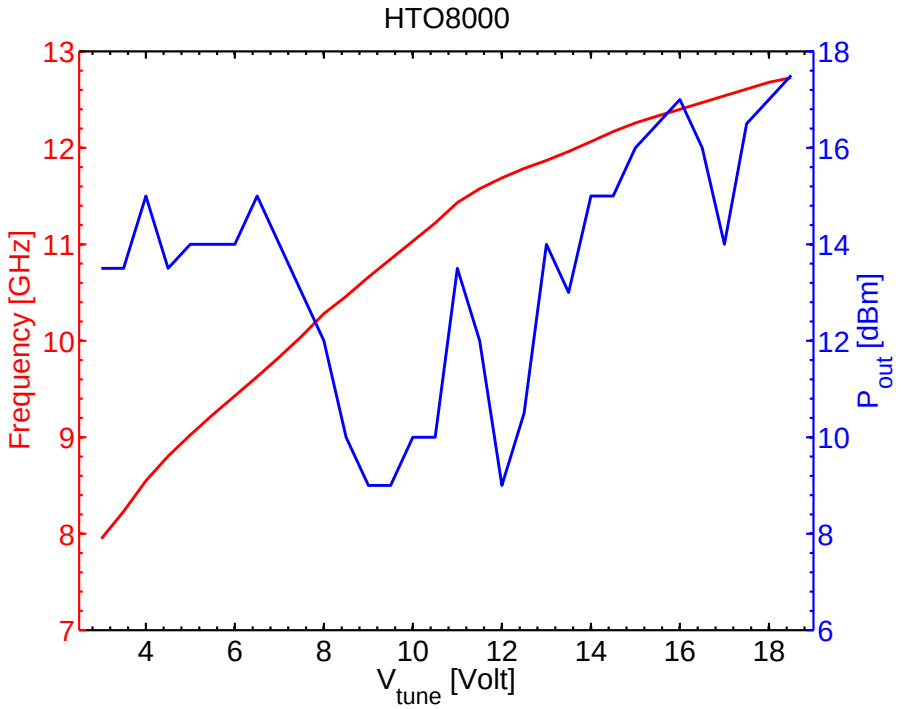

Figure 3.10: Plot of the HTO tuning voltage versus output frequency (red) and output power (blue).

plasma by the saturated active multipliers that follow the HTO. The HTO oscillators were selected for two main reasons: (i) they are not sensitive to the stray magnetic and electric fields and therefore the sources could be placed close to the Tokamak, connected to the machine port by short paths of fundamental waveguides; (ii) they can be swept in a short time scale ($\geq 20\mu s$) when driven with a proper source. We developed special drivers (DR1 see appendix A) for the generator units to enable ultra fast full band sweeping [13] which is crucial to minimize the effect of plasma turbulence on the distance measurements. Operational amplifiers are commercially available with large signal bandwidth but it was impossible to find an integrated circuit capable of assuring all the requirements of the

reflectometry application: large signal bandwidth >10 MHz (distortion < 0.1 %); product gain bandwidth > 300MHz; output swing 0–22V; slew rate > 5 V/μs when driving capacitive loads; and constant input/output delay . A discrete amplifier was developed using a classical operational amplifier topology (see figure 3.11). To minimize ringing and guarantee stability, frequency compensation is done using the C_f/R_f network. The drivers provide tuning voltages limited to the interval 3 - 20V to avoid any damage of the HTO tuning port due to an erroneous input signal. Tests of the drivers showed good linearity, large bandwidth ($\geq 20\,MHz$) and very small time delay ($\approx 4\,ns$).

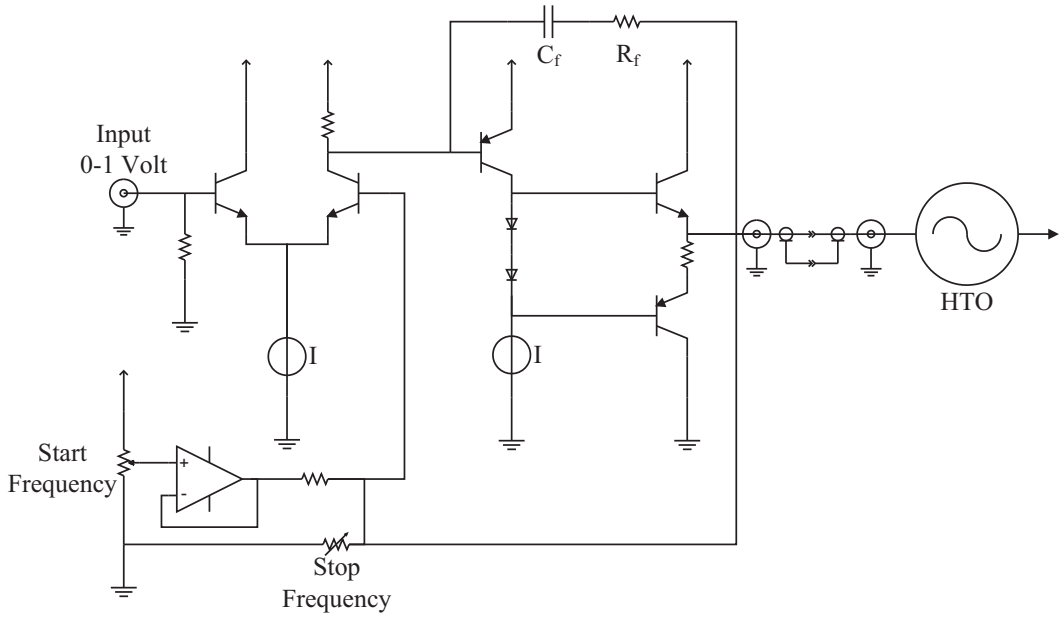

Figure 3.11: Fast tuning HTO driver using a classical operational amplifier topology.

The non linear frequency characteristic of the HTO is the only drawback of this configuration which imposes the need for a sophisticated dynamic frequency calibration procedure as described in section 3.2.4, plus post linearisation of the acquired signals before data processing for profile inversion.

The power at the output of the different frequency multipliers is $P \geq 15\,dBm$ for the K and Ka bands; $P \geq 10\,dBm$ for Q band; $P \geq 8\,dBm$ for the V bands and 10 dBm for W band.

3.2.3 The fast tuning ramp

To ensure proper synchronisation, the diagnostic should be run from a common clock placed at the control room, close to the signal digitisers modules. The long distance (some 90 m) between the control room and the HTOs, rises the problem of finding a

way to tune the microwave sources. A coaxial cable or an analogue optical link can be used to transmit a tuning ramp. The first solution is not adequate due to cable bandwidth limitations and signal contamination by electric noise. The second option allow to overwhelm these problems but the commercially available devices do not meet the necessary requirements on linearity and offset stability. Generating a synchronised ramp close to the HTOs seems to be the right approach to the problem. The high temporal resolution measurements to be performed with the ASDEX-Upgrade reflectometry system, imply the following requirements on the operation of the HTO devices: (i) generation of a ramp signal between 0 and 1 Volt, in $20\mu s$, with up to 2048 levels and a linearity better than 0.05%; (ii) synchronism between the ramp generation and data acquisition;(iii) galvanic isolation between the ramp generator and the clock source, which are separated by some 90 m; and (iv) the ramp generator should work in burst mode[2]. To accomplish all the diagnostic requirements we have decided to implement the sweeping system in four modules: (i) the ramp generator, based on a very fast digital-to-analog converter, with a settling time less than $10ns$; (ii) the clock transmitter;(iii) the clock receiver; and (iv) a ramp to triangular wave selection module. Figure 3.12 shows a block diagram of the complete set-up.

The ramp module

The heart of this module is the DAC650 from BURR-BROWN. It is a 12 bit digital-analogue-converter, with a unique design to achieve very fast settling time and high resolution. A mixed technology of gallium arsenide for speed and silicon for accuracy, is used. To generate a ramp a set of counters are incremented for each clock pulse. At the end a reset is made pre-setting the device for a new ramp.

The board in figure B.4 has an ECL (Emitter Coupled Logic) clock ,a TTL (Transitor-Transitor Logic) clock, a reset and a load inputs. Through a front connector it is possible to write a 12 bit word to set a fixed output voltage. In the same connector a 6 bit word can address the board; it is therefore possible to have several boards sharing the same data bus (a dip switch sets the address).

The timing circuit. An arrangement of monostables[3] generates all the necessary timing signals to assure that a valid word is set to the DAC input.

The clock circuit. All clock signals go to a logical OR. The TTL ones are first

[2]In opposition to continuous mode, a burst of pulses is send for every trigger.

[3]Type of multivibrator circuit in which one of the states is stable, but the other is not – the circuit will flip into the unstable state for a determined period, but will eventually return to the stable state. Such a circuit is useful for creating a timing period of fixed duration in response to some external event.

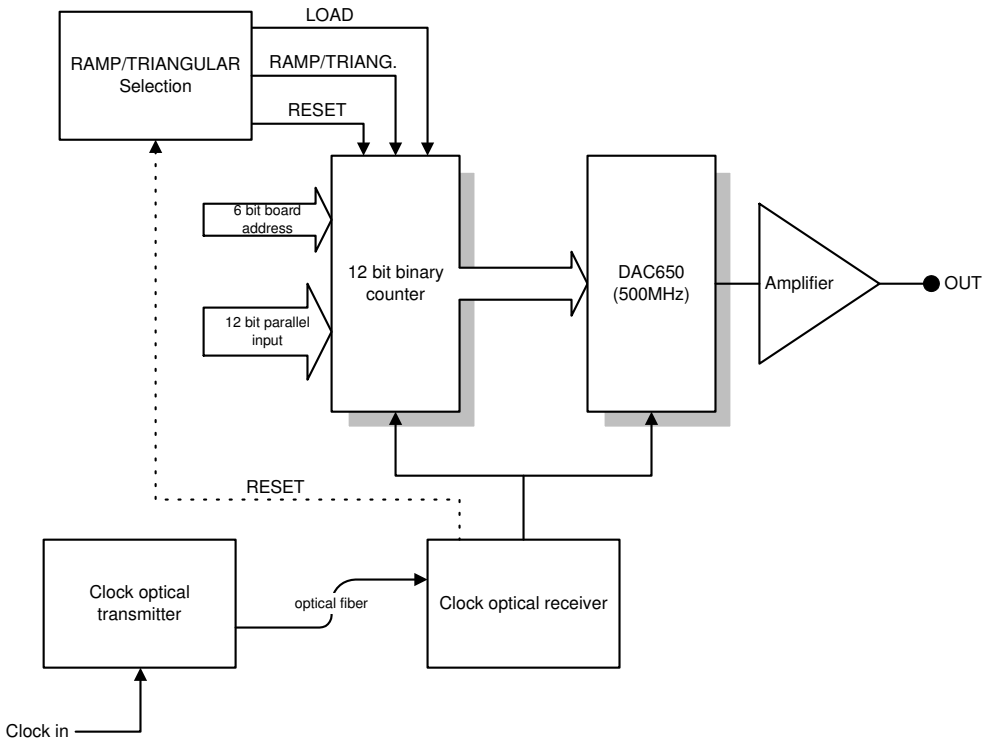

Figure 3.12: Block diagram of the tuning ramp generator.

converted to ECL.

The counter. A set of three ECL counters are incremented to generate a 12 bit word. It is possible to load a word on these counters. To fix the starting voltage, a set of dip switches is used (offset word) to write a word on two latches. The external word uses another pair of latches and overrides the offset word. Before reaching the DAC, they are first converted from TTL to ECL. Every time a reset signal is applied, the output voltage returns to the initial voltage.

The output stage. The DAC650 shows a output impedance of 50Ω. At the output we have placed a fast amplifier (U9), with the ability to drive some 100mA. The gain is given by -R3/50Ω. Changing the R3 value it is possible to compensate the load. The offset can be fine adjusted in the range ± 10 mV, using R14 and U14.

The clock transmitter

The ECL clock signal is transmitted from the control room to the DAC board placed in the diagnostic cubical inside the tokamak room via a mono-mode 100μm fiber, using the optical transmitter circuit plotted in figure B.1. This module is build around an optical hybrid transmitter, the HLP118. This device is design to operate with is counterpart the

HPL118 and forms a high data rate optical link (DC to 200 Mbits/s). The DC coupling is an important feature for operating in bursts.

The clock receiver

In figure B.2 is plotted the schematic of the clock receiver. This module includes the HPL118, an optical hybrid receiver. The recovered clock is fed to a line driver resulting in four outputs. A set of monostables generates a 300 ns pulse to reset the DAC, some $3\,\mu s$ after the end of the clock burst.

Triangular / ramp control module

The schematic of the triangular / ramp control module is displayed in figure B.3. With this module we can program the operation mode of the ramp generator to output a single up ramp or an up-and-down ramp (triangular wave). A set of monostables generate the necessary timing pulses.

Test results

Static and dynamic tests were performed to evaluate the DAC stability and linearity. We found an offset error < 0.40 mV, full scale error < 1.10 mV, null offset error < 0.0 mV, the gain error < 1.5 mV and linearity error < 3.9 mV. The full-scale settling times is less than 10 ns . Figure 3.13 shows the output ramp for a $20\,\mu s$ up-and-down sweep. Please

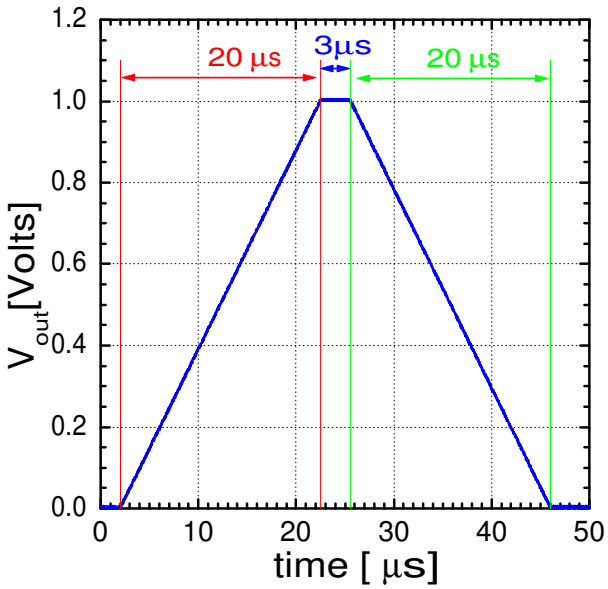

Figure 3.13: Output of the fast tuning ramp generator for a $20\,\mu s$ up-and-down sweep.

note the $3\,\mu s$ flat top needed to setup generator before starting the down ramp.

3.2.4 Dynamic frequency calibration

The static frequency limits where set for all bands to the values shown in table 3.6 by adjusting the HTO drivers.

Frequency band	Fmin (GHz)	Fmax (GHz)
K	15.883	25.477
Ka	25.101	37.260
Q	34.760	49.981
V	48.730	73.199
W	71.860	100.118

Table 3.6: Static calibration frequency limits.

In FM-CW reflectometry technique the accuracy of the frequency calibration has a strong impact on the quality of the reconstructed electron density profiles and therefore a novel dynamic frequency calibration has been developed compatible with the ultrafast sweeping time scale used in the profile measurements. In fact with fast sweeping sources using sophisticated and fast electronics the risk of frequency deviation is significant. The deviation can be caused by thermal or post-tuning drifts, hysteresis, and aging or a combination of all these. The problem can be more relevant if the microwave sources do not have a linear frequency characteristic. To overcome of this problem we have included in the reflectometry system since its early phase of operation a dynamic calibration circuit based on frequency markers. This includes a comb signal, synthesized from a highly stable 0.5 GHz crystal oscillator and covering the frequency range 0.5 - 18 GHz, with amplitude spikes spaced by 0.5 GHz. Samples of both the probing and comb signals are mixed and the intermediate frequency signal of 125 MHz is band-pass filtered and afterwards amplified/detected in a logarithmic SDLVA (successive detection logarithmic video amplifier), resulting in a so called video signal. The calibration is performed automatically (without the need of dismounting the oscillators) by the direct measurement of the output frequency providing a calibration curve with up to 25 points. The circuit is represented in blue in figure 3.14 and the set of possible frequencies for the markers are shown in table C.1, where it is also indicated the first and the last markers for each band.

The above procedure proofed not to be capable of reproducing with enough detail the tuning characteristic of the HTO. This lack of detail originates the bumps in the group delay curve resulting from a reflection at a metallic mirror (see figure 3.17 (a)), which otherwise would be constant for the complete frequency band. We have used this

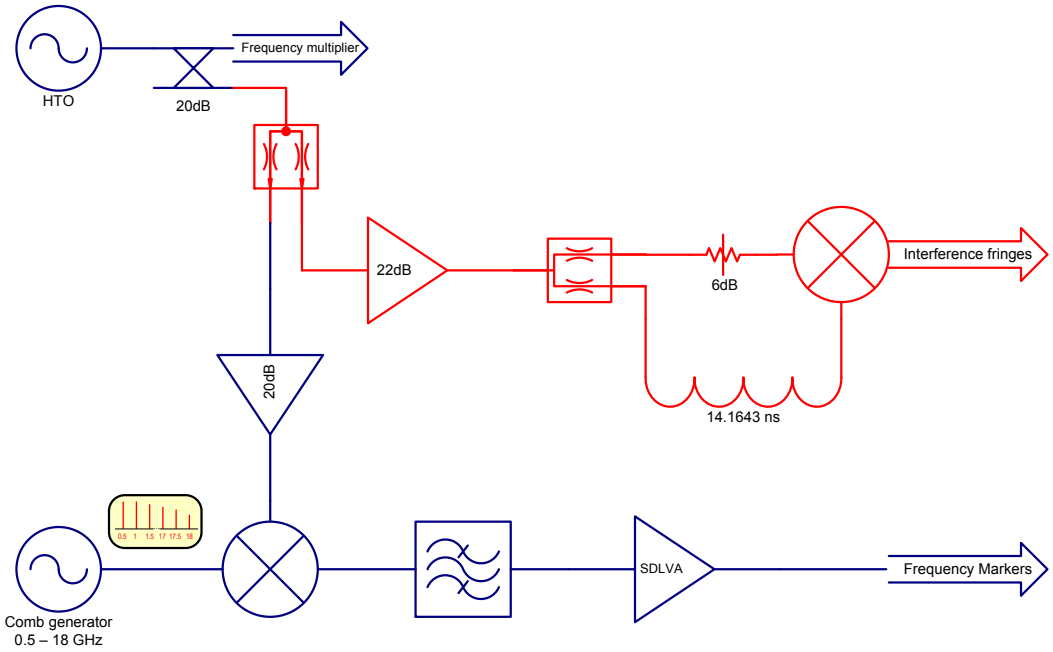

Figure 3.14: Block diagram of the dynamic calibration circuit.

information to obtain the detailed calibration curve. Equation (3.6) shows how to recover the real probing frequency step from the phase shift of a reflection at a metallic mirror placed at a distance d.

$$f_b = \frac{\Delta\varphi}{2\pi}\frac{1}{t_{sample}} \tag{3.6a}$$

$$\Delta F = f_b \frac{t_{sample}}{t_{delay}} \Rightarrow \Delta F = \frac{\Delta\varphi}{2\pi}\frac{1}{t_{delay}} \tag{3.6b}$$

$$t_{delay} = 2\,\frac{d}{c} \tag{3.6c}$$

On the ASDEX Upgrade reflectometry system a metallic reflection can only be obtained during vacuum breaks and therefore calibration would only be possible during limited periods which may not be sufficient. We overcome this major drawback of the method with a calibrated coaxial line. Such a line with $t_{delay} = 14.1643\,ns$ was added to the existing markers circuit, as shown in red in figure 3.14. In figure 3.15 it is depicted the data extracted in a calibration procedure, namely the interference signal (a), the frequency step (b) and the frequency markers (c). The instantaneous phase evolution of the signal in figure 3.15 (a) is obtained by *Hilbert Transform* [14] and the frequency step is obtained by using equation 3.6b. It is clear from the figure that the discrete markers cannot account for the fast changes of the tuning sensitivity of the HTO like the one

occurring around 21 μs. To obtain a continous calibration curve the start frequency must

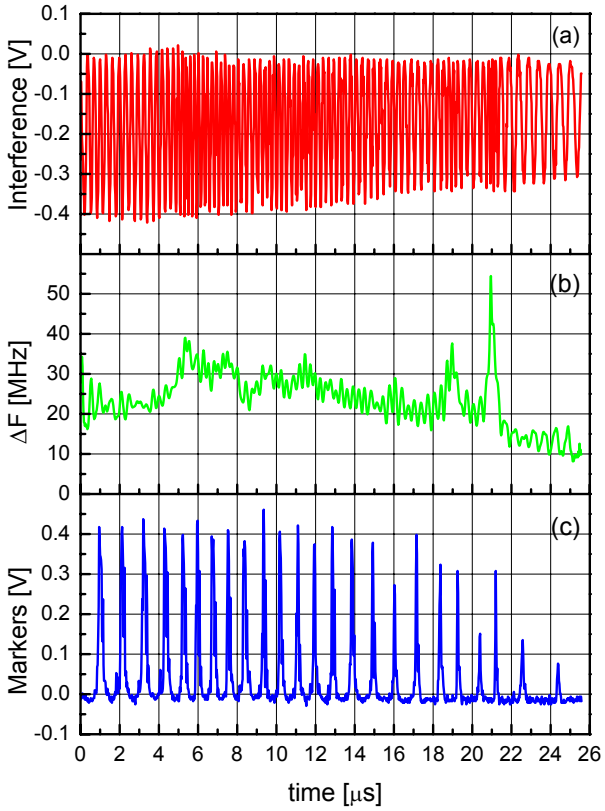

Figure 3.15: a) Interference signal. b) Frequency step from the interference signal. c) Frequency markers signal.

be given and we use for this purpose one of the first frequency markers. The resulting calibration curve is shown in figure 3.16. The improvement is enormous when comparing the two group delay curves in figure 3.17, where (a) is calibrated using only the frequency markers and (b) uses the delay line calibration. In (a) we have a maximum variation of 0.167 ns resulting in a oscillation of the position of the mirror of 24.9 mm, while in (b) the maximum variation is only 0.049 ns which results in a 7.4 mm oscillation of the position of the mirror.

In this way a very accurate frequency linearisation is obtained and it is possible to have a new calibration for each band every 10 sweeps during plasma operation. Using the novel frequency calibration procedure an accurate microwave contribution to the group delay was obtained for all density profile channels, thereby improving the matching between adjacent frequency bands and therefore the profile inversion.

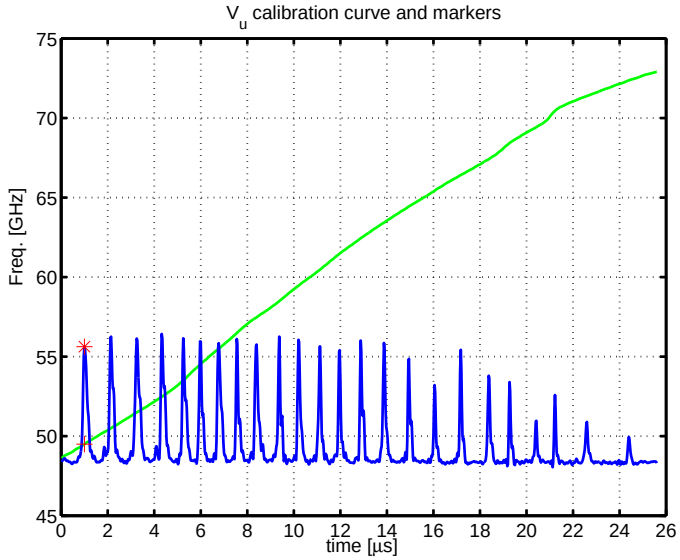

Figure 3.16: a) Markers signal (blue) with the chosen marker for start frequency (red) and the resulting calibration curve from figure 3.15(b)(green).

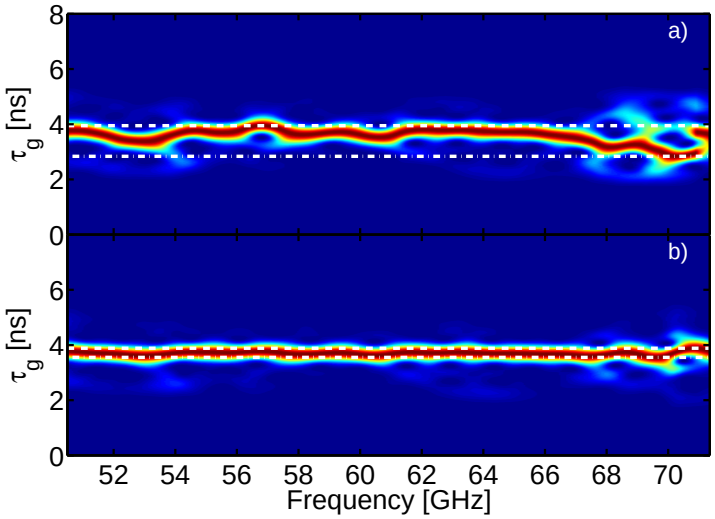

Figure 3.17: Group delay of a V band reflected signal in a metallic mirror placed 39.6 cm apart from the antenna: (a) frequency calibrated using only the markers; (b) using the the calibration obtained with the delay line. The white dashed lines represents the limits of deviation for the group delay.

3.2.5 Microwave components testing

Although all the components are important to guarantee the good performance of the diagnostic, there are few components of crucial importance that should be carefully tested. We have on the previous sections analysed the millimetre-wave sources and the antennas. We should also check the performance of the:(i) directional couplers, since they guarantee

the correct separation of the probing and the returning signal; detectors where the beat signal that contains the group delay information is detected.

Directional couplers

A directional coupler is a four port device as illustrated in figure 3.18. The three most

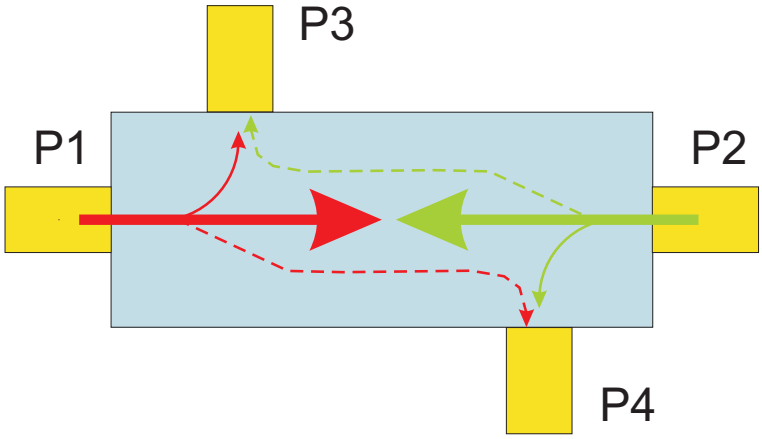

Figure 3.18: Four port directional coupler schematic. Dash lines represent the effect of finite *directivity*.

important parameters in the specification of a directional coupler performance are the *coupling*, *directivity* and *through loss* which can be defined as follows:

$$Coupling(dB) = 10\log\left(\frac{P1}{P3}\right) \tag{3.7a}$$

$$Directivity(dB) = 10\log\left(\frac{P3}{P4}\right) \tag{3.7b}$$

$$ThroughLoss(dB) = 10\log\left(\frac{P1}{P2}\right) \tag{3.7c}$$

where **P1** is the incident power in port **1** and **P2**, **P3** and **P4** are the output power at ports **2**, **3** and **4**, respectively, assuming that all ports are adapted with matched loads.

Equivalent relations can be established when **P2'** is the incident power in port **2**:

$$Coupling(dB) = 10\log\left(\frac{P2'}{P4'}\right) \tag{3.8a}$$

$$Directivity(dB) = 10\log\left(\frac{P4'}{P3'}\right) \tag{3.8b}$$

$$ThroughLoss(dB) = 10\log\left(\frac{P2'}{P1'}\right) \tag{3.8c}$$

In our application port **3** is terminated by a matched load. Port **1** connects to the millimetre-wave generator, port **2** is connected to the antenna and port **4** is connect to the detector. All selected couplers have a coupling factor of 3 dB because it can be shown that this option maximizes the reflected power at port **4**. We use high directivity couplers ($> 35\,dB$) because this reduces any signal coming directly form the source (port **1**) to the detector (port **4**), which would originate an additional reference (as can derived from equations 3.7b and 3.8b). The signal available in port **4** should be due to the reflection in the reference pin plus the plasma reflection. All the directional couplers were tested experimentally to evaluate its real performance. Since we cannot access port **3** because is terminated by an internal load, we must define a new quantity, the *isolation*:

$$isolation(dB) = 10\log\left(\frac{P1}{P4}\right) \tag{3.9a}$$

$$isolation(dB) = 10\log\left(\frac{P2'}{P3'}\right) \tag{3.9b}$$

Which can be related to *directivity* by:

$$isolation(dB) = Coupling(dB) + Directivity(dB) \tag{3.10}$$

To measure the *directivity* we start by measuring *isolation* using equation (3.9a), and then use equation (3.8a) to obtain the *coupling* and finally use equation (3.10). Table 3.7 resume the measured data, showing: minimum measured values for *coupling* and *directivity*; and maximum measured values for *through loss*.

Frequency band	Coupling [dB]	Directivity [dB]	Through loss [dB]
K	3.10	46	3.2
Ka	3.01	46	3.3
Q	3.05	43	3.3
V	3.08	40	3.5
W	3.05	38	3.9

Table 3.7: *Coupling*, *directivity* and *through loss* for the different directional couplers. O-mode, X-mode, HFS and LFS channels use the same type of directional coupler for the same frequency band.

We can conclude that all values are within the required specifications in particular the *directivity*.

Detectors

As mentioned before we use single ended detectors to recover the interference signal that contains the group delay information which is the relevant information to calculate the electron density profiles. This adopted detection scheme was imposed by the fact that it should be compatible with the reference pin arrangement. The main advantage is its simplicity. The disadvantage is that phase and amplitude effects are mixed. They can only be separated using an I/Q detection but this would require an heterodyne receiver which is not compatible with the pin arrangement. The mixed amplitude and phase variations is not a problem in most cases because the amplitude variations along the frequency sweeping varies in a slower time scale than the phase variations.

The detectors are *Silicon Low Barrier Schottky Diodes* for all bands including the V and W bands. In fact as we explain in section 3.2.7 we also use single detection for these bands in spite of the heterodyne scheme. The detectors are used at the intermediate frequency which is $\approx 1.2\,GHz$. The key detector specifications are the frequency range, open circuit voltage sensitivity, tangential sensitivity, square-law response and input power.

All detectors that were selected to operate in the frequency range of their millimetre-wave band of operation show a flat response throughout the frequency band.

The *open circuit voltage sensitivity* (usually expressed in mV/mW) gives an idea of how efficient is the detector to convert RF power to output voltage. This value is measured with the detector loaded with a high impedance, but in our application is much lower because the detection amplifier loads the detector with a low impedance with the objective of improving the detector video bandwidth.

The *tangential sensitivity* gives an idea of the minimum detectable power, and is defined as the lowest input power level for which the detector will have an 8 dB signal-to-noise ratio at the output of the video amplifier. In our case it ranges from -55 dBm to -45 dBm for the Q band.

The term *square-law response* simply means that the output voltage is proportional to the power or the input voltage squared. Most millimetre-wave detectors are inherently square-law from the tangential sensitivity power level up to about -15 dBm, which is in fact the region of operation on all our bands.

In our case the input signals are the reference signal, $V_R(t) = A_1 \sin(\omega t)$ (reflected on pin) and the one propagating and reflecting in the plasma, $V_P(t) = A_2 \sin(\omega t + \phi)$, where ϕ is the phase contribution due to the progation in the plasma. The detector output is

given therefore by [15]:

$$\begin{aligned}
\left[V_R(t)+V_P(t)\right]^2 &= \left[A_1\sin(\omega t)\right]^2+\left[A_2\sin(\omega t+\phi)\right]^2+ \\
&+ 2A_1A_2\sin(\omega t)\sin(\omega t+\phi), \\
&= \frac{A_1^2}{2}\left[1-\cos(2\omega t)\right]+\frac{A_2^2}{2}\left\{1-\cos\left[2(\omega t-\phi)\right]\right\}+ \\
&+ \frac{2A_1A_2}{2}\left\{\cos\left[(\omega t+\phi)-(\omega t)\right]-\cos\left[(\omega t+\phi)+(\omega t)\right]\right\} \quad (3.11)
\end{aligned}$$

Due to the presence of the RF bypass capacitor C (see figure 3.19) the second harmonic of the signal in equation (3.11) is suppressed and the detector video output is:

$$Video_{out}=\frac{A_1^2+A_2^2}{2}+A_1A_2\cos(\phi) \quad (3.12)$$

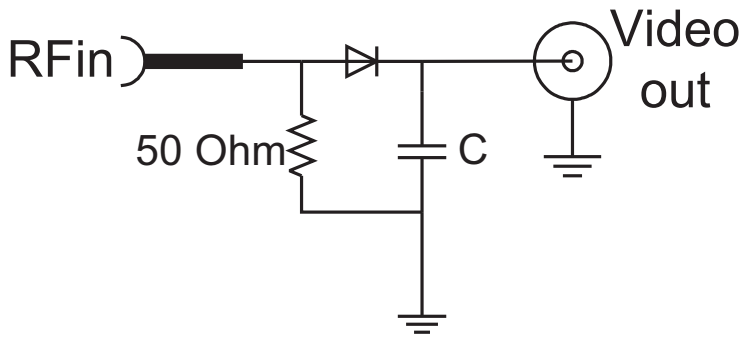

Figure 3.19: A simple square-law mixer-detector.

The frequency of the detected signal, beat frequency, given by:

$$f_b(t)=\left(\frac{1}{2\pi}\right)\frac{d\phi}{dt} \quad (3.13)$$

is proportional to the group delay of the probing waves, due to propagation and reflection in the plasma:

$$f_b(t)=\tau_g(t)\,\frac{dF}{dt} \quad (3.14)$$

where the quantity dF/dt is the sweeping rate of the probing wave. The correct estimate of the quantity f_b evolution over the complete frequency band of each channel is the key information in the reconstruction of the electron density profile with FM-CW broadband reflectometry.

To avoid detector destruction the input power should be below an absolute maximum of 20 dBm. In normal operation this is always the case but when high power radio

frequency spurious radiation from auxiliary plasma heating systems like ECRH reaches the system antennas, this absolute maximum can be easily overrun. That is why we have included in all waveguides 140 GHz notch filters (frequency operation of the ECRH system).

Figure 3.20 displays the Q band detector response when loaded with 1 kΩ impedance. The load is the input impedance of the detection amplifier and its value was chosen in order

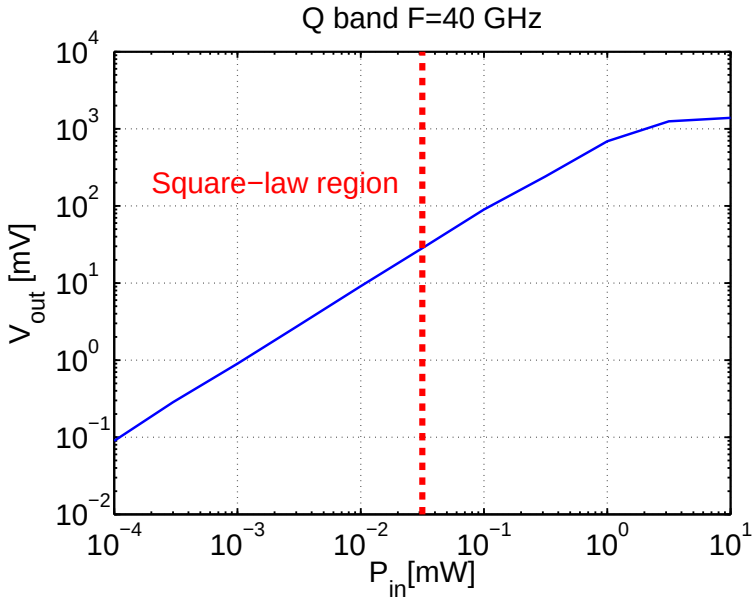

Figure 3.20: Q band detector response for a testing frequency of 40GHz.

set the best compromise between the detector video bandwidth and voltage sensitivity.

The square-law region of operation is also marked, corresponding to a input power ≤ 0.03 mW. For an input power above 0.03 mW the output voltage is no longer proportional to the power. For a 1 MΩ load the manufacture specifies a voltage sensitivity of 1200 mV/mW. From figure 3.20 the voltage sensitivity is ≈ 900 mV/mW, which reflects the expected reduction for a 1 kΩ load.

3.2.6 Signal detection and conditioning

In order to account for the very fast sweeping operation, we have developed detection amplifiers (AMP1 and AMP2 in figure A.1, A.2, A.3, A.4 and A.5) with enlarged bandwidth and detector loading plus amplification compatible with minimum noise requirements. The amplifiers include a four step programmable gain (see figure C.10) with a bandwidth of 40 MHz capable of accommodating the expected highest beat frequencies. When necessary, detector polarization is also included for enhanced sensitivity (≥ 6 dB).

For the connection between the detection amplifiers and the signal conditioning amplifiers (feeding the acquisition system) we designed dedicated analog optical links with a bandwidth of 150 MHz and S/N > 50 dB. The core elements of the optical boards are commercial hybrid modules; the connection between emitter and receiver uses a mono-mode 50 μm fiber.

The output of the optical links are fed into a conditioning amplifier (with continuous variable gain in the range 1/10 to 10, bandwidth 40 MHz), as shown in figure C.11, and to an analog filter (Low Pass Butterworth, 5^{th} order) with four different cutoff frequencies, to select the suitable bandwidth at the input of the ADC modules which avoids any aliasing effects (see figure C.12).

3.2.7 The heterodyne detection

When the probing frequencies are higher than 50 GHz the signal to noise ratio for homodyne detection can be very poor. This is due to a combination of less available power from the microwave sources, with higher waveguide losses plus the fact that the reflecting layers are located far away from the antennas than in lower frequency band. In a homodyne system the sensitivity is limited by the waveguide detector tangential signal sensitivity (TSS) and the detector load will set a compromise between bandwidth and sensitivity. With a heterodyne detection the sensitivity can be very close to the theoretical maximum but it is limited by the dual side band noise figure of the receiver mixer. As described in section 2.2.6 this technique needs a local oscillator to track the main signal with good accuracy. The two oscillators are phase locked to each other by means of a 10 MHz quartz phase locked loop (PLL), with an offset frequency equal to the intermediate frequency (IF). This technique or variations of it have been implemented on other reflectometer [16]. The IF value has been selected around 1.2 GHz . It should be high enough to accommodate the highest expected fringe beat frequency (50 MHz). The design includes ECL electronics and large bandwidth amplifiers for fast frequency and phase looking. Some stability problems had to be solved by using a careful design. The detection is single ended, as in a homodyne configuration, for compatibility with the reference pin scheme and follows the topology shown in figure 2.9 of section 2.2.6. Quadrature detection can be implemented as a further upgrade of the single ended circuit and full phase and intensity variation could be obtained, but the pin reference must be removed and a new reference scheme must be implemented by sampling a fraction of the probing signal. Laboratory tests showed a sensitivity improvement of about 42 dB for V band (50–75 GHz) and 30 dB for W band (75–100 GHz). The PLL capture range in IF is in the range 4 to 700 MHz, with an acquisition time below 50 ns, and sensitivity of -10 dBm at 192 MHz during lock

state condition. Both systems can sweep a full band in $20\mu s$.

3.2.8 Control system

As we refer in section 3.2 the system is placed close to the tokamak vessel which imposes the need for the implementation of a remote control. Remote operation is also of great importance as it permit the off-site operation of the reflectometry diagnostic, which is a pertinent capability for the next step fusion devices like ITER.

All functions of the reflectometry system can be activated from a workstation, namely the on/off switching of the generators, the set-up of the gain of each detection amplifier, the operation of the selection of the frequency bands [17]. A schematic representation of the control system is presented in figure C.1. Initially the heart of the system was a 386PC connected via RS232 to the workstation and to all other devices to be controlled: three 8031 I/O boards, one clock generator and five fixed frequency control boards. A menu driven program running on the PC worked as a command interpreter and generated the appropriate bit words for the different devices. Two of the 8031 I/O boards are placed inside the cubical near the machine. They are connected to one of the serial PC ports via an optical serial link and share the same port, using a daisy-chaine configuration. The two boards provide a total of 48 output bits and 16 input bits for the several control tasks (for example, power switching, selection of the amplifiers gain control). Schematics of I/O buffers are shown in figures C.4 and C.5. The third board is used for setting the cut-off frequency for the analog low-pass filters placed in the cubical at the control room. The five fixed frequency control boards (placed in the cubical close to the vessel) use a single serial port and the same daisy-chaine arrangement, to set the individual fixed frequencies and to change from sweep to fixed frequency operation. The fourth serial port is used to control and program the clock generator used for the acquisition system and the ramp generator. In addition a parallel port is used to switch the power of the hardware placed in the cubical close to the vessel and to generate a software trigger to the acquisition system when used during the tests (schematics in figures C.2 and C.3).

The operator of the diagnostic must have access simultaneously to the control and to the configuration of the acquisition time windows. The existence of the control PC forced the software to be spread between this PC and the control workstation creating the risk of a possible conflict of operating modes (ex: hardware configured to fixed frequency and the acquisition set to broadband operation). It was then decide to upgrade the workstation with the necessary hardware to take over the tasks previously performed by the PC [18]. This has simplified the configuration of the system and made it possible to run the operation software solely on the workstation avoiding any inconsistency. On

the new configuration a single daemon-server application runs on the workstation and is responsible for every task required by the operation of the diagnostic. Multiple users can connect to this server, through internet sockets, using a client application. Only one client can operate the diagnostic but all the others can monitor the current system status.

Recently this software was upgraded to accommodate the improvements made to the control hardware and in particular the firmware of all of the eight control boards was upgraded to use a high level language [19]. This makes the communication between the workstation and this boards more robust.

3.2.9 Data acquisition

Until September 1997 the acquisition system was based on four 100 Msamp/s CAMAC modules and five specially designed 250 Msamp/s transputer based VME modules [20]. This mixed arrangement imposed some limitations to the operation of the diagnostic. By the end of 1997 a new system based exclusively on VME modules has become operational. It includes three specially designed VME boards, each with four 250 Msamp/s channels or 1 Gsamp/s if the four channels are operated in an interleaved way [21]. Each channel presents a maximum vertical resolution of 8 bits. A commercial VME Pentium processor board running Linux supervises the system. Each channel can acquire continuously up to 3140 Kbytes of data or 3066 sweeps with 1024 points each. The trigger is generated by the ASDEX Upgrade central timer and the time base is in reference to this single event, making it possible to correlate the acquired data with the other diagnostics. Together with the control system this new acquisition made the operation of the diagnostic more flexible in terms of the acquisition windows. This is an important subject in very fast diagnostics with high temporal resolution, because memory is limited and a judicious selection of the acquisition time windows is needed to improve the flexibility of the measurements namely to accommodate changes of the acquisition time windows to record acquiring interesting plasma phenomenon with the best possible time resolution.

3.3 Assessment of the system performance without plasma

Each channel of the system was tested both in the laboratory and the in tokamak vessel. While the tests in the laboratory are crucial for the system development, testing at the Tokamak without plasma is essential to account for the performance of the complex waveguide routing. In both cases a metallic mirror was used as a reflector.

3.3.1 In-vessel testing

The in-vessel testing included the installation of a metallic mirror at several fixed distances d from the antenna mouth, the calibration of the reference pins and the measurement of the power in several points of the transmission lines. With the metallic mirror we could obtain the maximum precision in recovering the position of a target for each system channel.

In figures 3.21 to 3.24 it can be seen some of the results obtained with the Ka and W channels when the metallic mirror is placed at various distances.

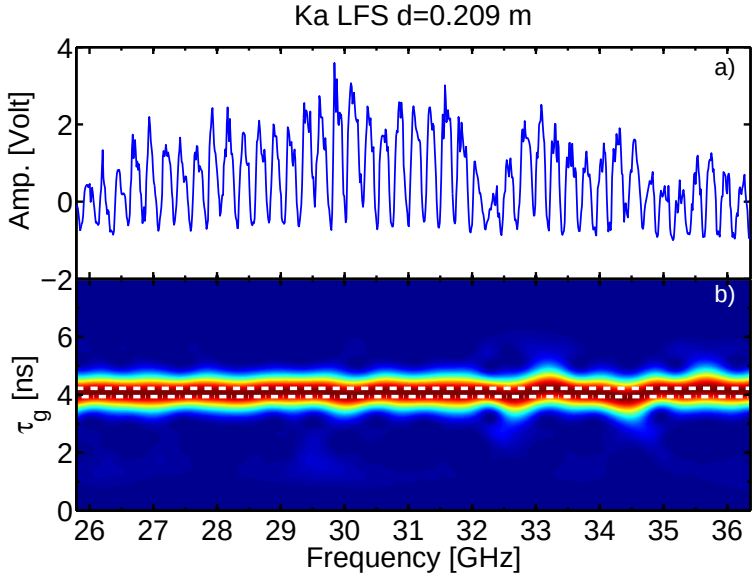

Figure 3.21: a) Ka band LFS signal obtained from a reflection in a metallic mirror placed at a distance $d = 0.209\,m$. b) Spectrogram of the signal in a); the white lines shows the maximum oscillation of the group delay.

The test with the in vessel mirror display the complete features of the system including the complex transmission that can cause spurious reflections or amplitude modulations (due resonance cavity effects), which will afterwords interact in a non-linear way with the signals reflected from the plasma decreasing strongly the accuracy of the inverted profiles.

The results in figures 3.21 to 3.24 exhibits the raw signals reflected from the metallic mirror as well as its corresponding spectrogram. These display the time resolved frequency spectra along each frequency band. The vertical scale is represented in group delay using equation (3.14). The displayed group delay has two contributions: one due to the mirror distance and the other associated with the waveguide path between the antenna mouth and the reference pin (section 3.3.2).

The signals exhibits amplitude modulations that are due mainly to the frequency response of the different millimetre-wave components (sources, amplifiers, etc.) plus the

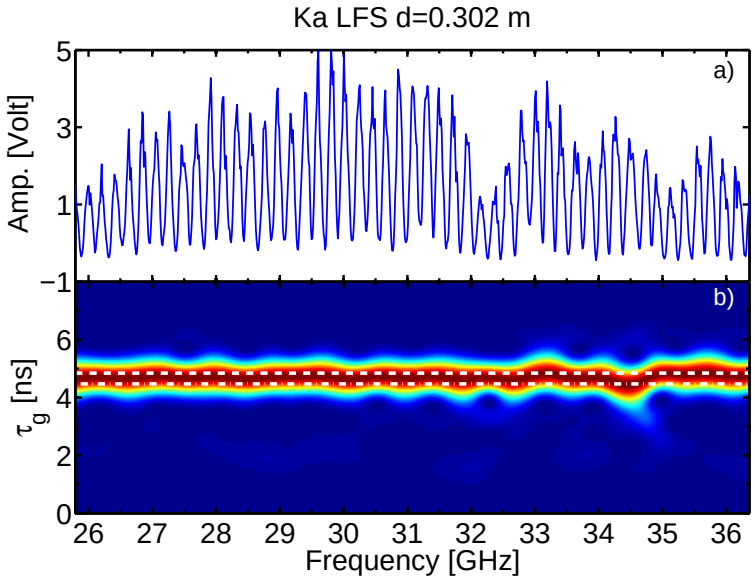

Figure 3.22: a) Ka band LFS signal obtained from a reflection at a metallic mirror placed at a distance $d = 0.302\,m$. b) Spectrogram of the signal in a); the white lines shows the maximum oscillation of the group delay.

transmission line effects. In spite of those modulations the spectrogram show that the signal energy is well concentrated along a line which gives a strong indication of the good system performance. The two white dashed lines bound the maxima and minima of the group delay spectral peak.

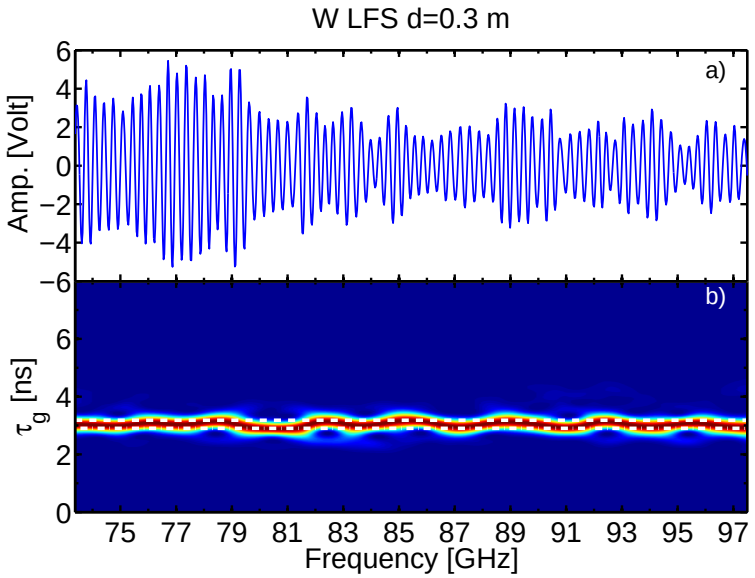

Figure 3.23: a) W band LFS signal obtained from a reflection at a metallic mirror placed at a distance $d = 0.3\,m$. b) Spectrogram of the signal in a); the white lines shows the maximum oscillation of the group delay.

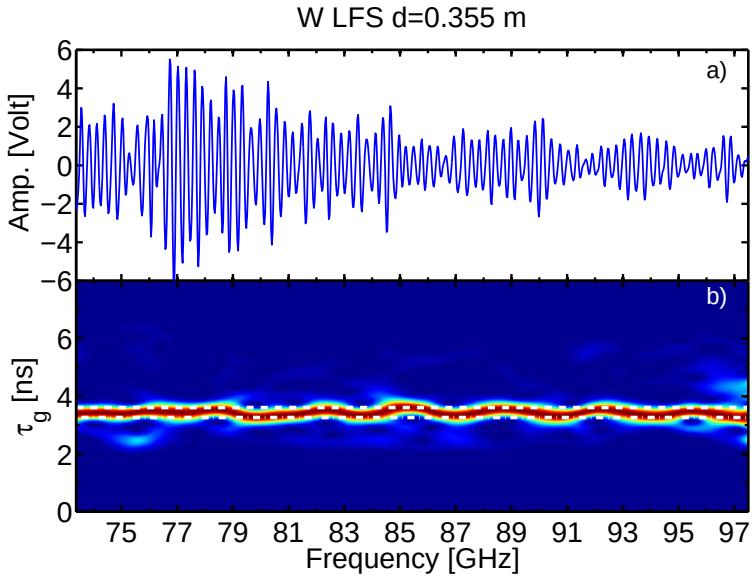

Figure 3.24: a) W band LFS signal obtained from a reflection at a metallic mirror placed at a distance $d = 0.355\,m$. b) Spectrogram of the signal in a); the white lines shows the maximum oscillation of the group delay.

After deducting the microwave path contribution from the group delay as it will be explained in next section the absolute mirror distance can be derived directly from the remanent group delay (see equation (3.15)). The results are presented in figures 3.25 and 3.26 for the LFS Ka and W channels, respectively. The distances are recovered with an

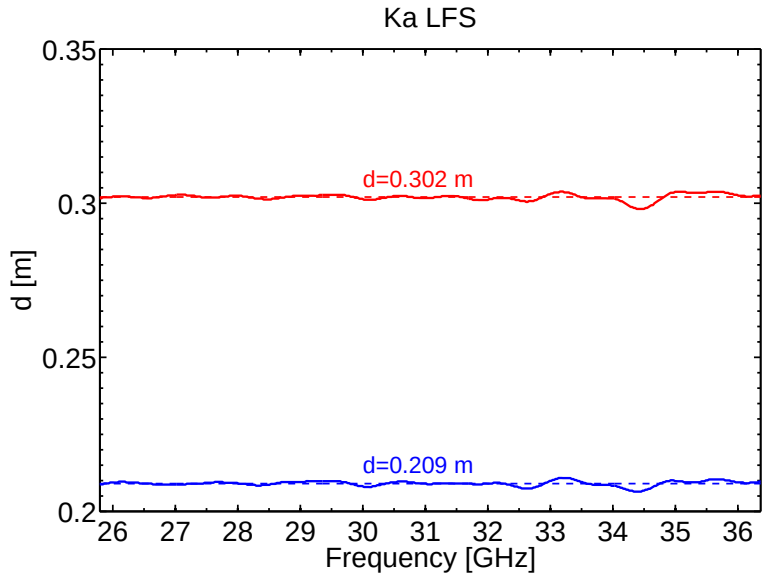

Figure 3.25: a)Evolution of the recovered mirror distance for the two reflectometry signals shown in figures 3.21(blue) and 3.22(red). Dashed lines mark the position of the mirror. b) Evolution of the mirror position shift for the two distances plotted in (a).

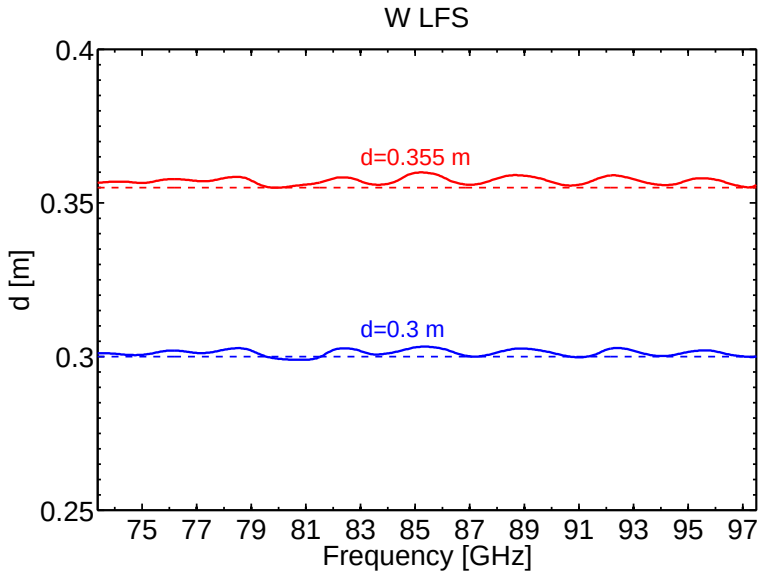

Figure 3.26: a)Evolution of the recovered mirror distance for the two reflectometry signals shown in figures 3.23(blue) and 3.24(red). Dashed lines mark the position of the mirror. b) Evolution of the mirror position shift for the two distances plotted in (a).

accuracy between 1 mm and 5 mm depending on the probing frequency and probing band. In fact this can even be better if we take into account that the position of the metallic mirror is evaluated with a ruler having an error of ±1 mm. It should be underlined that the accuracy of the distance measurement has to be evaluate at each probing frequency because the localization of each plasma layer requires the group delay values between zero and the frequency reflecting at the layer to be localized. The results of the tests reveal the superior performance of the system as well as the precision provided by the novel calibration procedure which is a basic requirement for successful density profile measurements (section 3.2.4).

3.3.2 Phase calibration

In the measurements with the plasma, the group delay includes three components respectively due to the propagation: (i) in the plasma, τ_p; (ii) in the vacuum path between the antenna mouth and the plasma, τ_v; (iii) in the microwave circuit τ_m between the antenna mouth and the reference pin. In order to perform profile inversion, the group delay due to the plasma must be extracted which requires to deduct the τ_v and τ_m contributions from the total group delay. The value of τ_m is obtained from the tests with the in vessel metallic mirror but τ_v cannot be easily measured because the position of the first plasma density layer is not known as and it varies with the plasma configuration.

In the following it is explained how the microwave contribution is estimated. As

already referred the total group delay τ derived from the signals acquired with the metallic mirror positioned at a known distance d is the vacuum contribution plus the microwave circuit one. As the distance d is known we can easily derive the vacuum contribution τ_v as they are related by equation (3.15).

$$\tau_v = \frac{2d}{c} \tag{3.15}$$

Where c is the speed of light. In this way the microwave circuit group delay is given by equation (3.16).

$$\tau_m = \tau - \frac{2d}{c} \tag{3.16}$$

This procedure was applied to all frequency bands for different distances of the mirror resulting in the values and presented in table 3.8. The accuracy of these results has a great impact on the profile accuracy.

Frequency band	Microwave contribution τ_m [ns]		
	LFS	HFS	X-mode
K	0.95297	0.96977	-
Ka	2.70228	0.98863	-
Q	1.13427	1.06975	0.56000
V	1.05328	0.98679	0.65662
W	1.04022	-	-

Table 3.8: Group delay contribution due to the microwaves (τ_m) for each channel.

Each antenna shows a different distance of the mouth to the plasma as its size and fixing position varies (see table 3.4). We must correct the group delay for these differences in order to derive a single group delay from the measurements of the several independent channels. We take as reference the channel on each side of the plasma in which the antenna mouth position is closer to the plasma. Ka band on the LFS and the K band for the HFS [22].

Table 3.9 shows the partial vacuum contributions that results from applying this methodology.

In particular any error on these two contributions (τ_m, τ_{vp}) will immediately introduce a mismatch between adjacent millimetre-wave bands in the combined group delay (from 16 GHz to 100 GHz) which would cause significant errors on the inverted profile.

Frequency band	Vacuum contribution τ_{vp} [ns]		
	LFS	HFS	X-mode
K	0.313	0.000	-
Ka	0.000	0.080	-
Q	0.247	0.067	0.000
V	0.307	0.093	0.067
W	0.087	-	-

Table 3.9: Partial vacuum group delay contribution (τ_{vp}) for each channel, due to the antenna mouth relative position.

3.4 Concluding remarks

In this section we describe the main steps of the diagnostic design and the solutions adopted for its implementation in the machine. Dedicated hardware was developed for best system performance in particular the antennae that launch and receive the probing/reflected waves. Novel techniques had to be developed for dynamic calibration of the frequency versus voltage curve which is a critical issue for profile measurements. The performance of the system in vacuum was characterized with detailed tests made both in the laboratory and in the tokamak (without plasma) using an in-vessel metallic mirror. Those tests provide a realistic evaluation of the reflectometry system accuracy once they use the complete configuration of the diagnostic: microwave transmission lines and antennas, control and data acquisition systems. A specific data processing software was utilized for a continuous analysis of the group delay curve for all the probing frequencies. Results show that the distances from the antenna to the mirror (in vacuum) are recovered with an accuracy between 1 mm and 5 mm. In the assessment the effect of plasma turbulence was not included and therefore the above results give an upper limit for the system performance. With plasma it is expected lower accuracy values due to the decrease of signal to noise ratio associated with scattering, diffraction and refraction effects suffered by the probing microwaves as well as phase noise caused mainly by scattering. However, the experimental results, as will be described in the next chapter, reveal that the system still retains its high spatial resolution in the presence of significant plasma turbulence and in particular in ITER relevant regimes like the H-mode.

References

[1] M. E. Manso, F. Serra, J. Mata, J. Barroso, J. Comprido, C. Teixeira, P. Caetano, P Luz, A. Monteiro, A. Silva, J. Mendonça, J. Neves, J. Pereira, S. Ramos, A. Almeida, L. Cupido, and P. Marques. A microwave reflectometric system for the ASDEX tokamak. In *Proceedings on* 15^{th} *European Conference on Controlled Fusion and Plasma Physics*, volume 12B, pages 1127–1130. European Physical Society, 1988.

[2] F. Simonet. TS 66.86.01. Technical report, Association EURATOM-CEA, 1987.

[3] Amanda E. Hubard. *Measurement of Electron Density on JET by Microwave Reflectometry*. PhD thesis, Imperial College of Science and Technology, 1987.

[4] S. O. Piper. Homodyne FMCW radar range resolution effects with sinusoidal nonlinearities in the frequency sweep. In *International radar conference*, pages 563–567. IEEE, Record of the IEEE 1995 International, May 1995.

[5] M. Brambilla. Ray tracing of lower hybrid and ion cyclotron waves. *Computer Physics Reports*, 4(3–4):71–93, August 1986.

[6] EURATOM/IST Association. Study of transport properties in ASDEX Upgrade using microwave. CCFP preferencial support technical report, November 1991.

[7] T. Grossmann, I. Nunes, F. Serra, M. E. Manso, and A. Silva. Sencitivity of fast swept frequency modulation reflectometry to changes in magnetic configuration in ASDEX Upgrade. *Fusion Enginnering and Design*, (34-35):425–428, 1997.

[8] M. Moresco, A. Vendramin, and E. Zilli. A focussing hog-horn antenna for microwave diagnostics in plasma machines. *Review of Scientific Instruments*, 51(8):1071–1074, August 1980.

[9] Constantine A. Balanis. *Antenna Theory: Analysis and Design*. John Wiley & Sons, 1982.

[10] I. Nunes and T. Grossmann. Design of hog-horn antennas for the ASDEX Upgrade reflectometer. Final report BSc in Engineering Sciences - Electronics Engineering, 1993.

[11] L. Cupido. Simulations on a fundamental waveguide with a pin reference inserted. Technical report, Association EURATOM/IST Centro de Fusão Nuclear, July 2005.

[12] Avantek, Inc., 481 Cottonwood Drive, Milpitas, California 95035, US. *Modular and oscillator components*, second edition, 1990.

[13] L. Cupido, A. Silva, M. E. Manso, and F. Serra. High performance drivers for fast sweep microwave reflectometry. In *Proceedings of the* 19^{th} *Symposium on Fusion Technology*, pages 865–868, Lisboa, July 1997. North-Holland.

[14] A. B. Carlson. *Communication Systems–An Introduction to Signals and Noise in Electrical Communication*. McGraw–Hill, New York, third edition, 1986.

[15] Jack Smith. *Modern Comunication Circuits*. McGraw-Hill Book Company, 1986.

[16] H.J. Hartfuss, T. Geist, and M. Hirsch. Heterodyne methods in millimetre wave plasma diagnostics with applications to ECE, interferometry and reflectometry. *Plasma Phys. Control. Fusion*, 39(11):1693–1769, November 1997.

[17] A. Silva, L. Cupido, M. Manso, F. Serra, F. X. Soeldner, P. Varela, C. Correia, C. Fernandes, C. Loureiro, A. Moreira, J. Neves, R. Pereira, J. Santos, and the ASDEX Upgrade Team. Fast sweep multiple broadband reflectometer for ASDEX Upgrade. In *Proceedings of the* 17^{th} *Symposium on Fusion Technology*, pages 747–750, Rome, 1993. North-Holland.

[18] V. Grossmann, J. Santos, P. Varela, M. Tavares, and M. Manso. New developments for the control and data acquisition system of the reflectometry on ASDEX Upgrade. *Fusion Enginnering and Design*, (48):25–30, 2000.

[19] S. da Graça. Operação e controlo remoto do sistema de reflectometria do tokamak ASDEX Upgrade. Master's thesis, Universidade Técnica de Lisboa - Instituto Superior Técnico, 2004.

[20] C. Loureiro, J. Santos, J. Simões, C. Correio, and M. Zilker. A high-speed transputer-based data acquisition system. *Measurement Science and Technology*, 7(1):21–25, January 1996.

[21] C. Loureiro, C. Correia, and C Varandas. High-speed multi-input VME bus data acquisition system. *Measurement Science and Technology*, 11(8):1224–1232, August 2000.

[22] P. Varela. *Automatic time-frequency analysis for plasma density profile evaluation from microwave reflectometry*. PhD thesis, Universidade Técnica de Lisboa - Instituto Superior Técnico, 2002.

4 Experimental results

After evaluating the diagnostic performance at the laboratory and in the vessel using a metallic mirror (as described in chapter 3), we assess the system performance in typical ASDEX Upgrade plasma discharges. Measurements obtained in several plasma regimens were analysed to determine the measuring capabilities of the diagnostic as well as its limitations.

4.1 Tolerance of the diagnostic to plasma vertical displacements

The different channels of the diagnostic are optimised for the machine equatorial plane. However as vertical displacements of the ASDEX Upgrade plasma often occur it is important to assess the decrease of the reflected signals resulting from refractive effects, which are associated with the curvature of the refractive index surfaces illuminated by the probing microwave beam, as indicated by the ray-tracing simulation studies (see section 3.2.1).

In the following we present results obtained in a circular limiter discharge #4809, where the plasma magnetic plane was shifted vertically in steps, with a total variation of $\approx 28\,cm$, leading to large vertical deviations of the plasma. This discharge is therefore, adequate to test the sensitivity of the diagnostic to vertical plasma displacements in a controlled way.

In figure 4.1 it is shown: (a) the line average density from interferometry; (b) and (c) the outer (FPG Raus) and the inner (FPG Raus) plasma positions derived from the magnetic data; (d) the vertical position of the plasma magnetic centre. The vertical traces in the figure indicate the time instants of reflectometry measurements.

In figure 4.2 it is plotted the reconstructed magnetic configuration cross sections of the plasma for the time instants $t_1 = 2.0\,s$, $t_2 = 2.81\,s$ and $t_3 = 2.905\,s$, giving insight about the movements that the plasma column undergoes from t_1 to t_3. At $t_1 = 2.0\,s$, the reflectometry antenna views the plasma below the magnetic mid-plane, $\Delta z \approx 5\,cm$ for the low filed side (LFS) and $\Delta z \approx 14\,cm$ for the high field side (HFS); at $t \approx 2.8\,s$, the midplane was shifted downwards by $\Delta z \approx 21\,cm$ below the LFS antenna and $\approx 12\,cm$

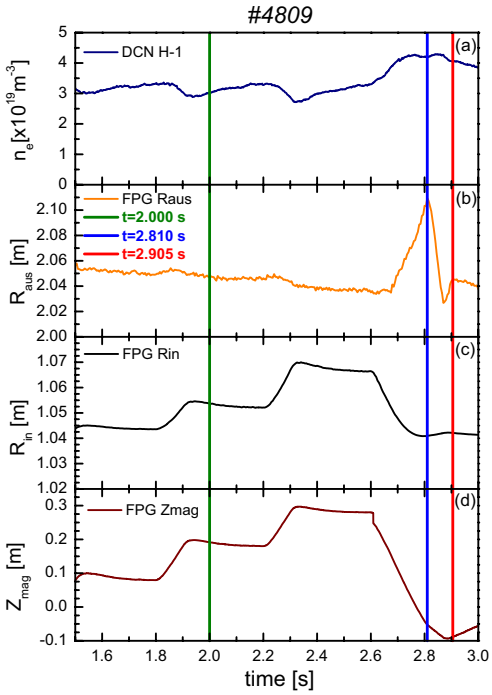

Figure 4.1: ASDEX Upgrade discharge #4809: (a) line average density from DCN interferometer; (b) R_{aus}, outer position of the last closed flux surface; (c)R_{in}, inner position of the last closed flux surface; (d) Z_{mag}, position of the plasma vertical magnetic centre. The vertical traces mark the acquisition times of reflectometry displayed in figures 4.3, 4.4 and 4.5.

below the HFS antenna. The largest shifts occurred at $t \approx 2.9\,s$, with $\Delta z \approx 23\,cm$ at the LFS and $\Delta z \approx 14\,cm$ for the HFS.

In figures 4.3 and 4.4 are represented the signals obtained obtained from $20\mu s$ sweeps with the K and Ka band reflectometers, respectively at the low and high field sides.

As the wave propagation is oblique to the density gradient due to the plasma deviations, a significant part of the microwave beam should be refracted. In fact it is observed that the amplitude of the reflected signal decreases for vertically displaced plasmas, as can be observed in figure 4.3 (f) and in figure 4.4 (f), specially at the LFS where the changes of the refractive index surfaces are more pronounced. The decrease should not be due to turbulence effects, as turbulence is not expected to vary significantly in ohmic discharges. In spite of the signal reduction, the sensitivity of the diagnostic is still enough to detect clearly the signal fringes up to the frequency $f \approx 37$ GHz ($n_e \approx 1.7 \times 10^{19}\ m^{-3}$). Signals reflected at higher densities (inner plasma layers) have lower amplitude and the measurement becomes difficult or impossible as the frequency further increases, due to the fact that longer oblique propagation paths lead to higher beam diffraction. This behaviour is in agreement with the ray tracing calculations presented chapter 3 (see figure 3.4) and in [1].

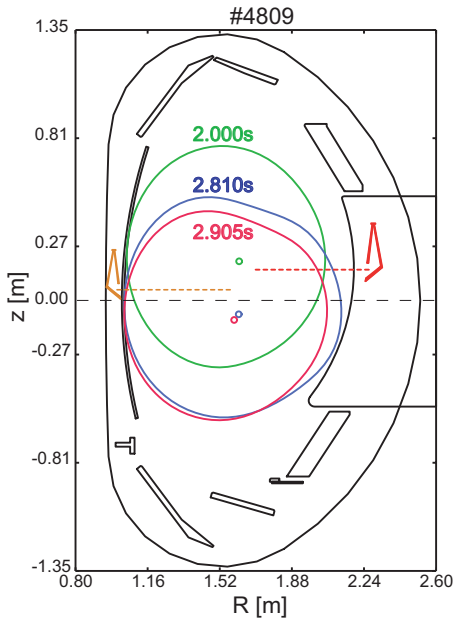

Figure 4.2: Reconstruction of the magnetic configuration cross sections of the plasma for the time instants where reflectometry measurements presented on this section have been performed, showing the configurations, at $t_1 = 2.0\,s$ (plasma center: $z \approx +0.19\,m, R_{mag} \approx 1.60\,m$, and for the vertical displacements at $t_2 = 2.8\,s$ ($z \approx -0.07\,m, R_{mag} \approx 1.62\,m$) and $t_3 = 2.905\,s$ ($z \approx -0.09\,m, R_{mag} \approx 1.60\,m$).

The electron density profiles inverted at $t_1 = 2.0\,s$, $t_2 = 2.81\,s$ and $t_3 = 2.905\,s$ are depicted in figure 4.5. It is seen that while at the HFS the profiles remain practically at the same radial position, (before and after the plasma vertical displacement), at the LFS the plasma move radially. The asymmetric evolution of the density profiles detected by reflectometry is consistent with the evolution of the magnetic configuration cross sections, shown in figure 4.2: at the HFS the separatrix is always located near $R \approx$105 cm and at the LFS the separatrix moves outwards from $R \approx$205 cm (at t=2.0 and 2.9 s) to $R \approx 211cm$ (t=2.8 s). The radial separation between profiles (t=2.8 s and t=2.9 s) reaches $\approx 10cm$ at the upper probed densities; this is in agreement with the evolution of the location of the last flux surfaces, as observed along the sight line (see Figure 4.2) of reflectometry at the LFS (the probed density layers are located deeper inside the vessel for t=2.9 s). It can be concluded that the reflectometry channels cope with rather large vertical plasma movements which is a result of the single antenna design (mono-static) where the reception is always optimised with moderated directivity.

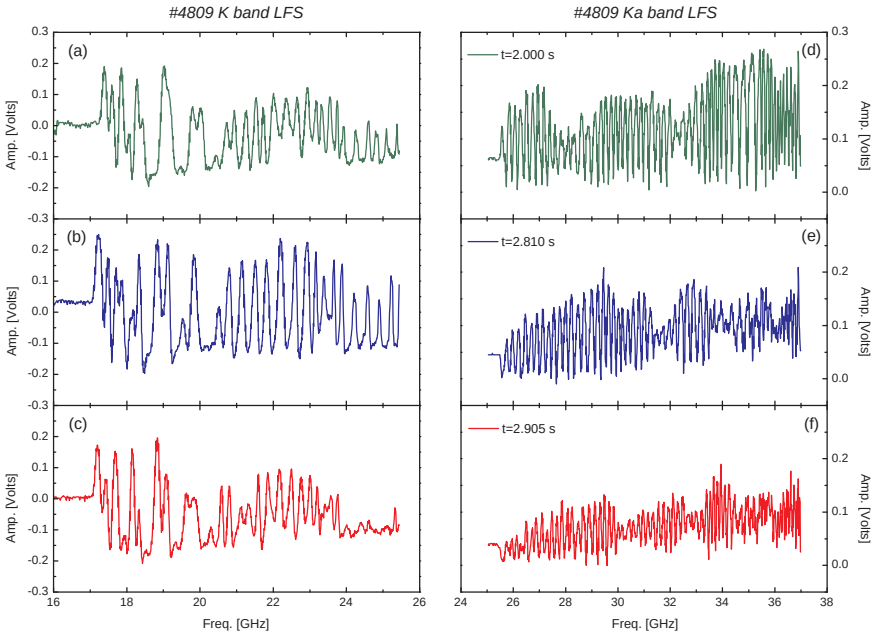

Figure 4.3: LFS raw signals for shot #4809 at $t_1 = 2.0\,s$, $t_2 = 2.81\,s$ and $t_3 = 2.905\,s$, obtained with sweeping time $\Delta t = 20\,\mu s$ (in the range 16-38 GHz).

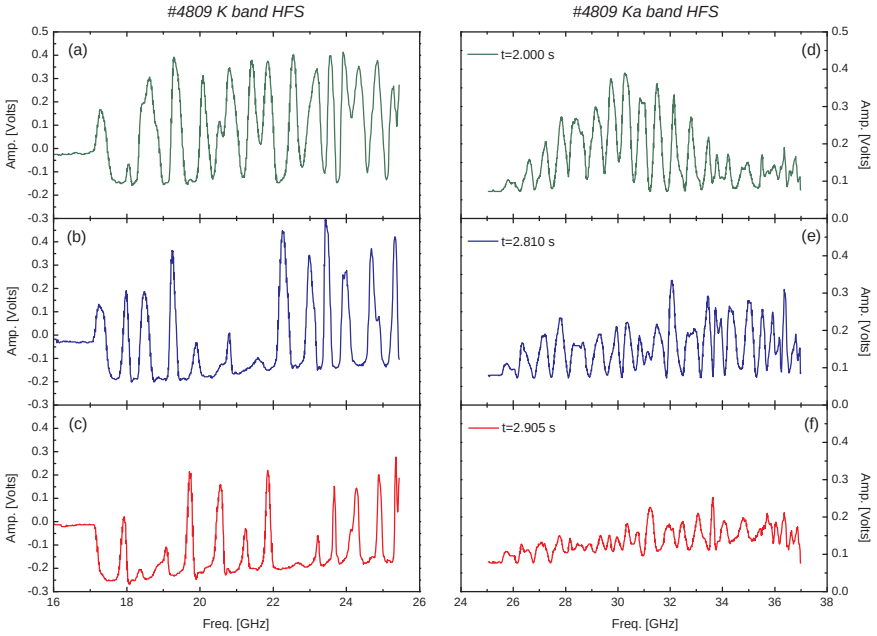

Figure 4.4: HFS raw signals for shot #4809 at $t_1 = 2.0\,s$, $t_2 = 2.81\,s$ and $t_2 = 2.905\,s$, obtained with sweeping time $\Delta t = 20\,\mu s$ (in the range 16-38 GHz).

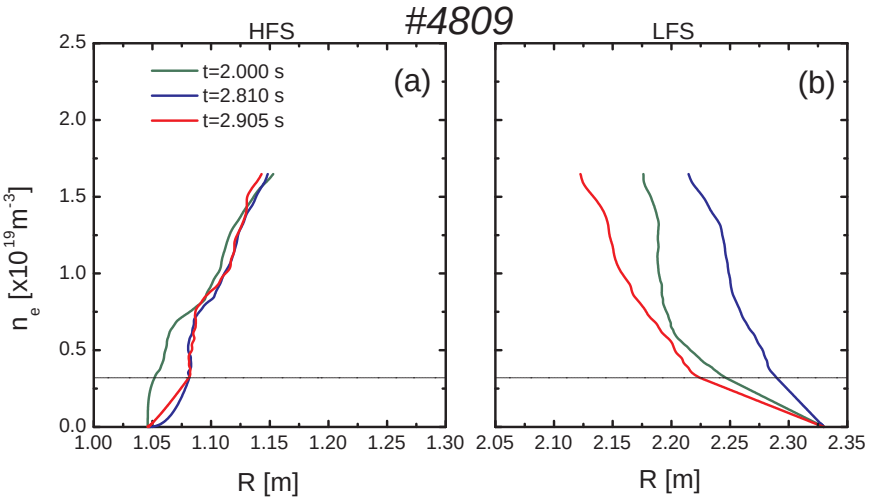

Figure 4.5: Density profiles obtained directly from reflectometry data, at HFS and LFS, for #4809 at $t_1 = 2.0\,s$, $t_2 = 2.81\,s$ and $t_3 = 2.905\,s$, with sweeping time $\Delta t = 20\,\mu s$ (in the range 16-40 GHz).

4.2 Sensitivity of the diagnostic to radial displacements

The reflectometry system measures the radial distances from the antennas to the reflecting layers and therefore it is important to evaluate the radial resolution of the measurements. In ASDEX Upgrade discharge #13171 the plasma achieves an H-mode regime at high density ($\overline{n}_e \approx 10 \times 10^{19} m^{-3}$), and the plasma radial position is scanned outward and inward by some 4 cm during the time interval 2.2 to 3.8 s, as shown in figure 4.6 (d) and (g), where Raus and Rin are the outer and inner most plasma positions, derived from the magnetics.

Figure 4.7 displays the reconstructed magnetic configuration cross sections of the plasma column, for three time instants. It is clear from the figure that only radial shifts are involved with only minor changes of the plasma shape.

The raw signals of figure 4.8 exhibit a variation of its beat frequency which is in agreement with the plasma column movements: (i) the beat frequency decreases when the plasma is closer to the antenna, at t = 2.670 s (see figure 4.8 (b) and (e)); (ii) it increases when the plasma is further away, at t = 3.470 s (see figure 4.8 (c) and (f)).

From the evolution of the position of the density layer $n_e = 0.5 \times 10^{19} m^{-3}$ in figure 4.6 (f) and (h), at the high field side (REF HFS) and low fiels side (REF LFS) given by reflectometry, it is clear the good agreement with the plasma position inferred from the magnetics. It should be noted that due to the higher level of plasma turbulence at the LFS, the evolution is better seen at the HFS. A deviation between ΔRin and ΔREF is observed for $t < 2.25\,s$ (before the plasma radial position scan) because the effect of the

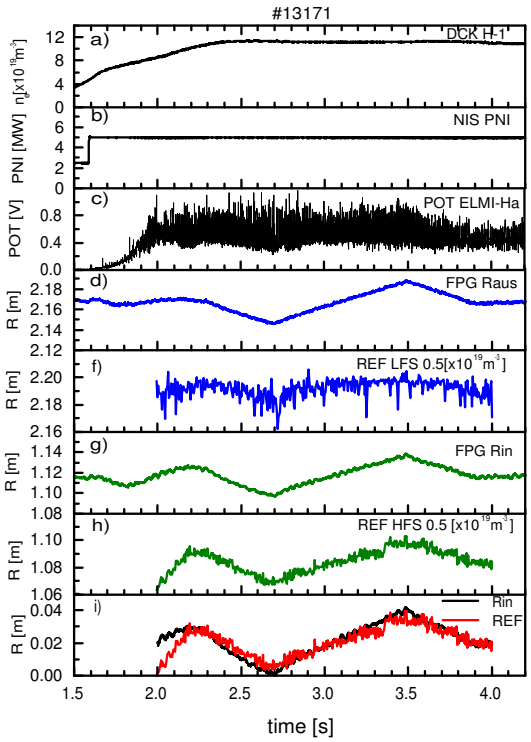

Figure 4.6: a) Mean density from DCN. b) Neutral beam power. c) Hα signal. d) Outer most plasma position from the magnetics. f) Position of the plasma layer $n_e = 0.5 \times 10^{19} m^{-3}$ from the LFS reflectometry profiles. g) Inner most plasma position from the magnetics. h) Position of the plasma layer $n_e = 0.5 \times 10^{19} m^{-3}$ from the HFS reflectometry profiles. i) Variation of the position from the magnetics and from reflectometry HFS.

radial plasma displacement is masked by the abrupt and great increase of the edge plasma density following the L-H mode transition. The above results shows that reflectometry is able to measure the location of specific density layers near the separatrix, which will be specially useful to control the position of the plasma boundary in next fusion devices during long pulse operation, when magnetic diagnostics may accumulate errors due to drifts. This new application is being further investigated in view of its importance for ITER [2][3][4].

4.3 Measuring range of distances and gradients

As referred in section 3.2.1 the system was designed for typical target plasmas with different density ranges, and different plasma positions (vertical and horizontal). From our previous experience on ASDEX and supported on ray-tracing simulation we have selected focused hog-horn antennas to launch and receive the probing microwaves. These proved to give good results and required rather small access to the vessel which is important in

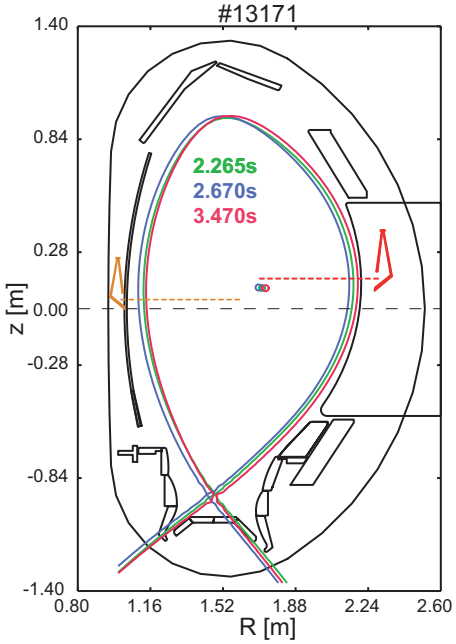

Figure 4.7: Recontruction of the magnetic configuration cross sections of the plasma for the shot #13171. Three instants are shown corresponding approximately to the plasma position maximum shifts.

view of the space constrains. The focusing range of the antennas take into account the regions of plasma to be probed by each antenna and should guarantee that the probed

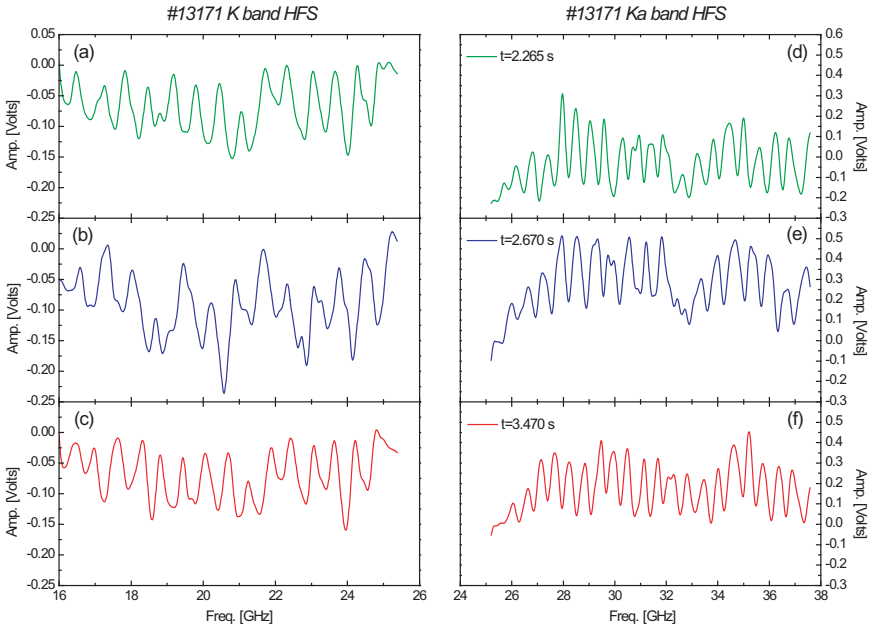

Figure 4.8: Raw data signals for the K and Ka HFS channels corresponding to the three time instants of figure 4.7.

layer should be between the focusing point and the antenna mouth. If not, the ray-tracing study indicates that partial or total loss of the reflected signal will likely occur. To access the capability of the system to measure in a wide range of distances and gradients we have analysed two discharges with a rather different plasma gradients. The first one was obtained in ASDEX Upgrade discharge #11711 with laser ablated impurities, where edge cooling pulses are produced by injection of Si by means of Laser-Blow-Off (LBO) between 3.75 s and 5.5 s. In such conditions a fast increase of the electron temperature in the

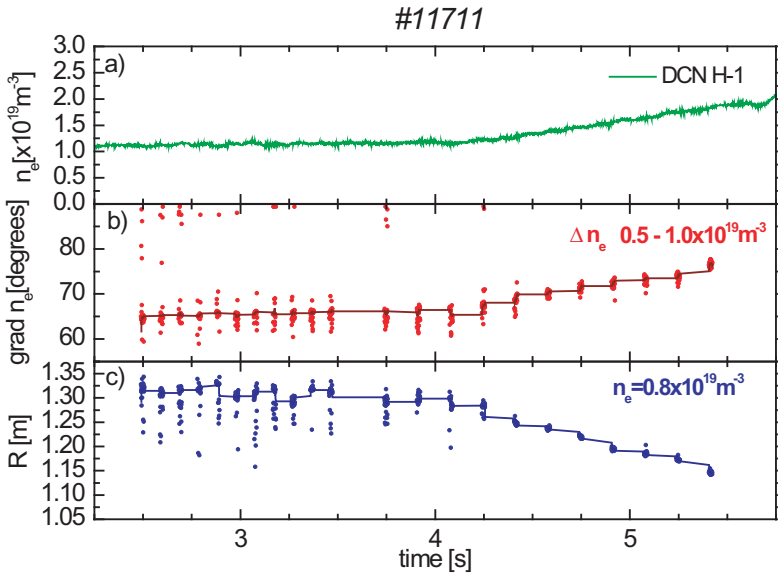

Figure 4.9: a) Evolution of the mean density from DCN for discharge #11711. b) Variation of the HFS reflectometry density profiles gradient. c) Evolution of the radial position of a plasma layer seen from HFS reflectometry.

centre is observed and the confinement is improved [5].

Figure 4.9(a) shows the evolution of the line integrated density obtained from the DCN interferometer ranging from $\approx 1.0 \times 10^{19} m^{-3}$ to $\approx 2.0 \times 10^{19} m^{-3}$. In this discharge the reflectometry system was operated in bursts of 32 consecutive sweeps (spaced by $50\,\mu s$) and the time interval between bursts was 100 ms. In figure 4.10 are plotted the electron density profiles from the ASDEX Upgrade microwave reflectometry system. At $t = 2.69764s$ and $t = 3.37308s$ the density stays constant and there is very little difference between the profiles. In fact there is a very slow ramp up of density as can be observed in the line average density (figure 4.9 (a)). After the Si Laser Blow-Off (starting at $t = 3.75s$) a steepening of the density profile is observed at both sides (measured after t $\approx$4.41 s) in agreement with the improvement of confinement. The density profiles that are represented in major radius exhibit lower density gradients at the HFS than at the LFS in agreement with the larger spacing of the magnetic field surfaces at the inner side

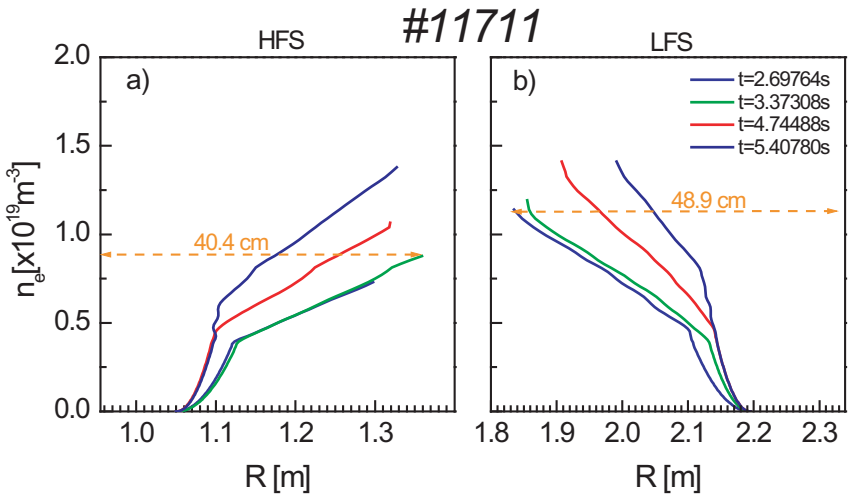

Figure 4.10: Electron density profiles measured from single $20\mu s$ microwave sweeps for shot #11711. a) High field side. b) Low field side.

of the tokamak.

In figure 4.9(b) it is represented the temporal evolution of the slope of the density profile defined as $grad = \arctan\left[\frac{n_e(x_2)-n_e(x_1)}{x_2-x_1}\right]$ in the density region $0.5 \times 10^{19} m^{-3}$ to $1 \times 10^{19} m^{-3}$ and in (c) the evolution of the radial location of the plasma layer $n_e = 0.8 \times 10^{19} m^{-3}$. It is observed that in spite of the great variations observed in each burst of density profiles, the line connecting the data from each burst follows the expected evolution, namely the profile peaking after the improved confinement starting for $t \approx 4\,s$. It should be noted that the profile variations within each burst of profiles decreases significantly after 4 s indicating that the level of fluctuations decreased, which is typical of improved confinement.

In figure 4.11 it is depicted a density profile from the HFS after being mapped into the LFS (dashed lines) by plotting the density along the corresponding magnetic field surfaces. Good agreement is obtained with the LFS profiles (solid lines), and the small shifts observed can be due to errors from the initialisation procedure and/or to small uncertainties related to the evaluation of the flux surfaces. The fact that density profiles measured with different reflectometer channels at the LHS and HFS shows the same temporal evolution and agree well when plotted in poloidal coordinates is a strong evidence of the good results given by the reflectometry system.

Distance range

The wide range of distances that can be measured with the system can be inferred from figure 4.10. At the HFS the system is able to measure up to 40.4 cm from the antenna

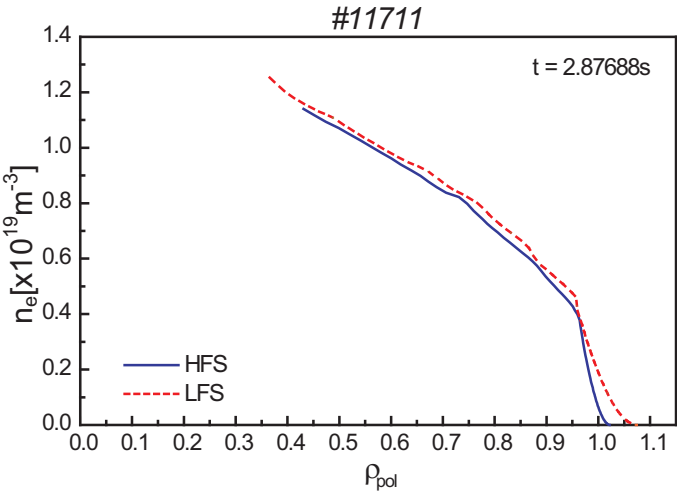

Figure 4.11: Mapping from the HFS profiles into the LFS, plotting the density along the corresponding magnetic field surfaces.

mouth and at the LFS up to 48.9 cm. It should be noted that the focusing range of the antennas is 40 cm (as could be seen in table 3.2).

Gradient range

The system can measure density profiles with wide range of density gradients; very low gradients, as in discharge #11711 (figure 4.9(b)); with very steep plasmas like in discharge #13171 (figure 4.12). In this figure it can be observed the evolution of the gradient for two plasma regions. The increase of the gradient for the highest density region at $t \approx 1.55\,s$ as the electron density builds up following the L-H mode transition, is clearly detected by the diagnostic (figure 4.12).

4.4 Combined X and O-mode profiles

Ordinary mode propagation (O-mode) is most adequate to measure the plasma density profile as its cut-off frequency depends solely on the plasma density. However, below densities $0.45 \times 10^{19} m^{-3}$, it is difficult to use O-mode because its wavelength becomes too large, which means that significant reflections occur before the waves reach the cut-off layer and the WKB approximation that allows the use of the Abel inversion is no longer valid.

In order to probe the density profile for $0 < n_e < 0.45 \times 10^{19} m^{-3}$, the extraordinary mode (X-mode) can be utilized. For the same reflecting density the wavelength is smaller than O-mode and therefore the WKB approximation is still valid; as its cutoff frequency

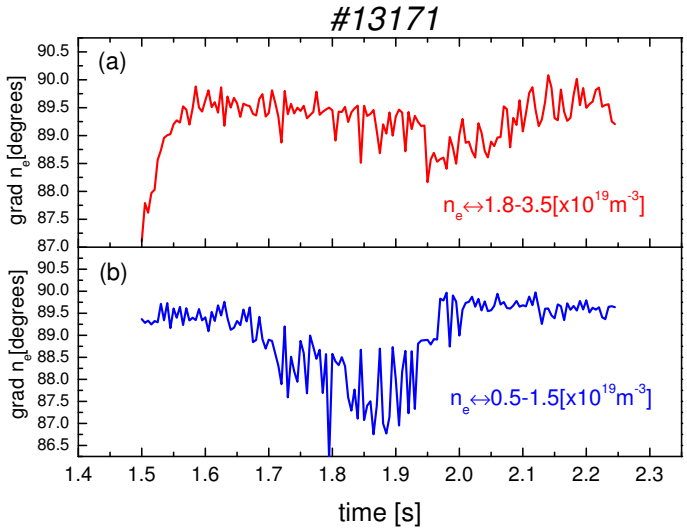

Figure 4.12: Evolution of the gradient of the HFS reflectometry profiles for two plasma regions.

depends both on the magnetic field and plasma density, X-mode waves can be reflected from almost zero density. However, X-mode has some important limitations, namely it operates only for an assumed magnetic field range and if B_t changes it becomes out of operation. Also, it depends critically on the correct identification of the first detected fringe $f_B(F)$, which in some cases is difficult. It was shown in [6] that an error of 1 GHz leads to a typical deviation of 4 cm in the position of the first plasma layer. Nevertheless, it is important to measure the outer part of the profile and to use it to initialise profile inversion from O-mode.

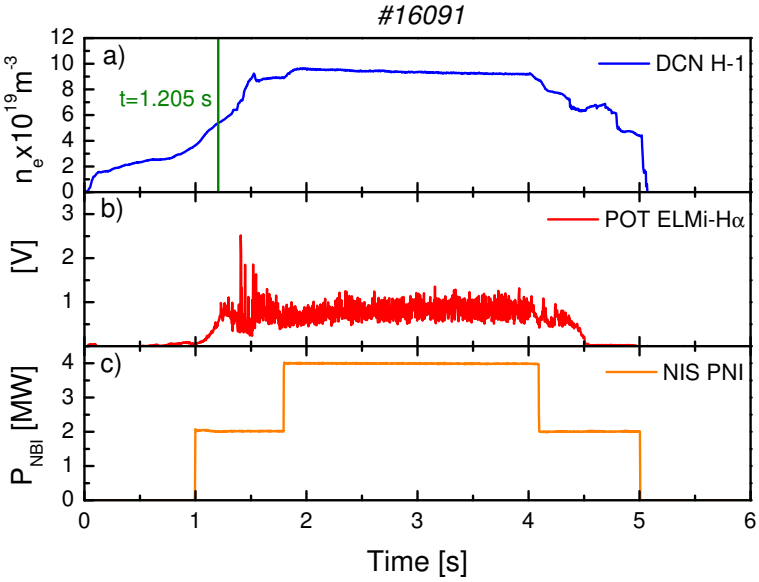

Figure 4.13: a) Evolution of the average density from DCN interferometer. b) H_α radiation at the main plasma. c) The neutral beam injected power.

To illustrate that method we present results obtained in ASDEX Upgrade standard H mode discharge #16091. In figure 4.13 it is shown the time traces of: (a) average density from interferometer diagnostic; (b) H_α radiation at the main plasma; (c) neutral beam injected power. The L to H transition occurs at $t \approx 1.3\,s$. In this discharge the reflectometer was operated in bursts of eight 20 μs sweeps with 15 ms interval between bursts. Figure 4.14 shows the X-mode signal from the Q band channel obtained at t = 1.205 s during the L phase prior to the L to H transition.

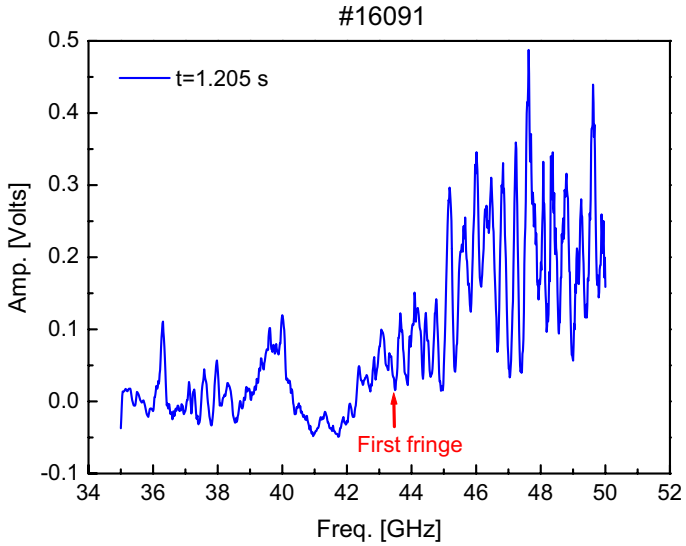

Figure 4.14: X-mode raw signal from the Q band channel at t = 1.205 s during L phase prior to the L to H transition.

The position of the first fringe F1(GHz) was determined by the method described in [6] which uses the jump in the signal power associated with the first reflected power to identify F1. The group delay derived from the X-mode detected signal is depicted in figure 4.15 resulting in the density profile shown in figure 4.16. The inversion was obtained with the numerical method described in 2.3.5. Using this profile we simulate O-mode probing leading to the O-mode group delay curve between $0 \leq F \leq 17.5\,GHz$ depicted in red in figure 4.17.

From the complete group delay curve (derived from X-mode reflectometry bellow F1 = 17.5 GHz and from O-mode above F1) a density profile was obtained as shown in figure 4.18. In this figure it is also shown for comparison the density data from Thomson scattering diagnostic, showing a good agreement with the results from combined O and X-mode reflectometry.

X-mode, although very useful to improve the accuracy of the measured profiles presents in some cases difficulties associated with the correct identification of the first

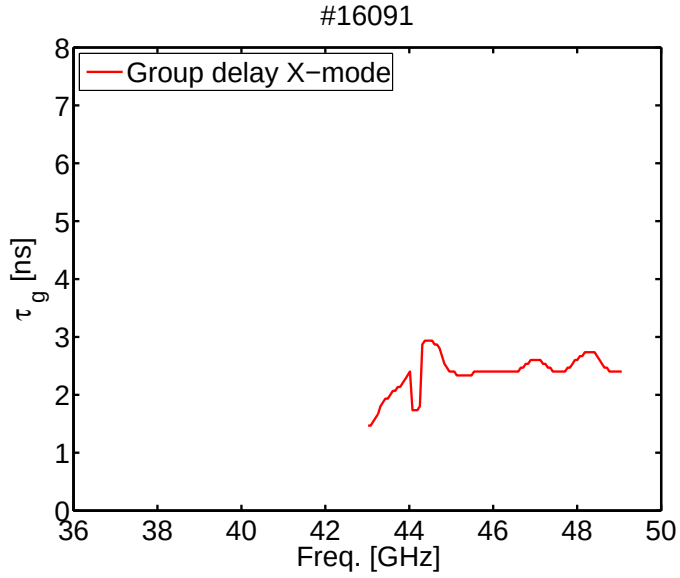

Figure 4.15: X-mode group delay from the Q band obtained from the signal in figure 4.14.

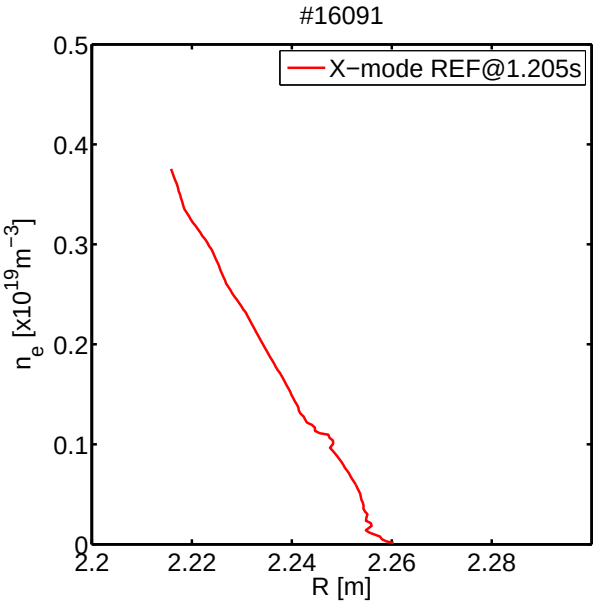

Figure 4.16: X-mode electron density profile from the Q band obtained from the group delay in figure 4.15.

fringe and also it implies a more time consuming data analysis. Fortunately, the combined O and X-mode results suggested that a linear extrapolation of the group delay curve down to zero frequency might be a good approximation for the profile initialisation[7]. In particular, the method proof to be quite accurate in relevant ASDEX Upgrade plasma scenarios where a steep edge gradient exists, because the importance of the initial group delay decrease with density and the density increase occurs in a very short radial distance

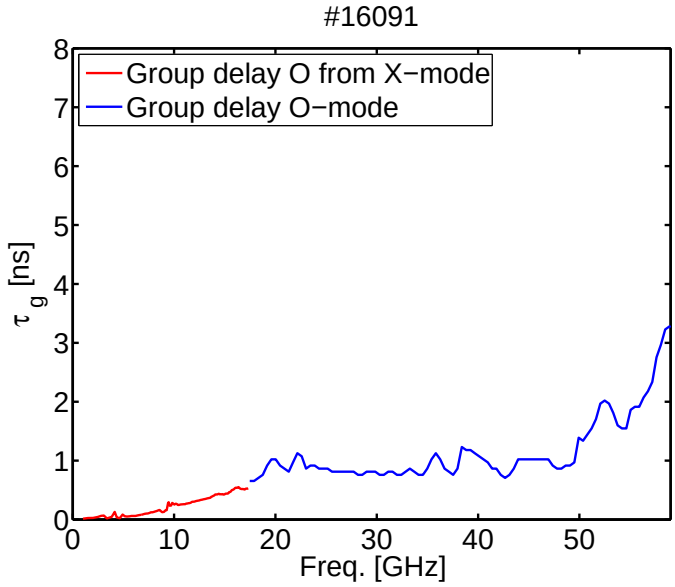

Figure 4.17: In red O-mode group delay obtained from the X-mode profile. In blue the group delay calculated from the LFS O-mode channels.

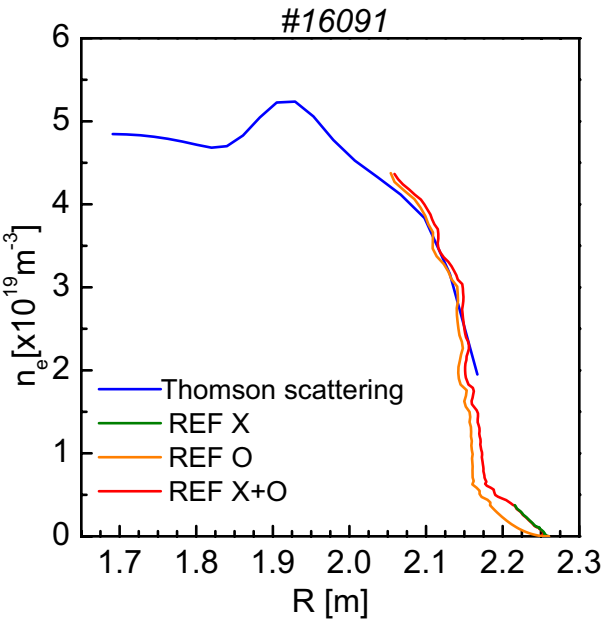

Figure 4.18: Reflectometry O plus X-mode electron density profiles. Comparison with Thomson Scattering profile and with the O-mode profiles linear initialized.

(typically a few mm). The method solely based on O-mode data has been extensively used to evaluate the density profiles on ASDEX Upgrade and a comprehensive analysis of the two types of measurements (O-mode plus linear extrapolation and O plus X-mode) is foreseen for the near future to further clarify this issue.

4.5 Comparison with other electron density profile diagnostics

It is important to compare the density profiles with other electron density diagnostics to validate and discard the existence of possible errors, although sometimes this could be difficult due to quite different time resolutions or physical positions around the torus. Here we have compared reflectometry density profiles with the ones from lithium beam in the scrape-off-layer (SOL) region of shot #19707. In figure 4.19 it is shown the relevant information for this shot; the mean density and the Hα signal. The vertical traces mark

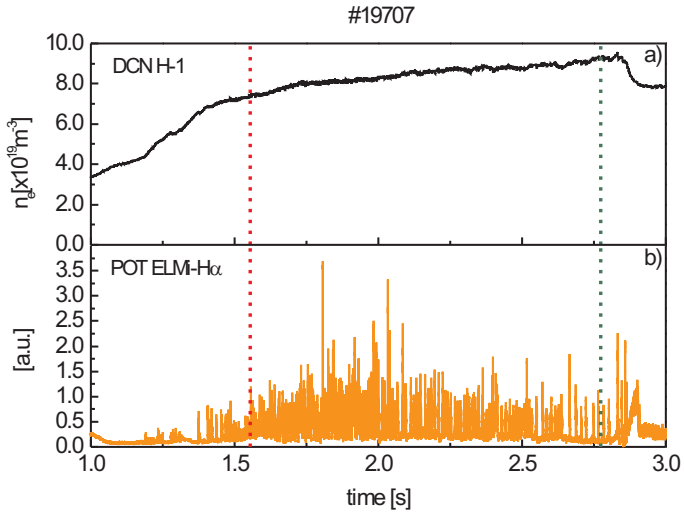

Figure 4.19: a) Evolution of the average density from DCN interferometer. b) The H_α radiation at the main plasma.

the time instants for the electron density profiles in figure 4.20. There is good agreement between the two diagnostics in terms of gradient and radial position (figure 4.20).

Reflectometry can measure in a reasonable range of different electron densities. To prove this ability we have analyzed the high density discharge #20580. figure 4.21 shows the relevant information for this shot. In figure 4.22 we have plotted the electron density profiles for the the Low Field Side (LFS) and High Fiels Side (HFS). We start with a low mean density of $\overline{n}_e \approx 4\times10^{19}\mathrm{m}^{-3}$ at $t = 0.950105\,\mathrm{s}$ and with time density increase, making that new channels start getting a reflected signal. The importance of the W band channel is exposed at $t = 3.080105\,\mathrm{s}$ where the density pedestal is located at $n_e \approx 7.5 \times 10^{19}\ \mathrm{m}^{-3}$ and can no longer be seen at the HFS because the maximum available probing frequency is exceeded.

We should also emphasise the good agreement with the Thompson Scattering data.

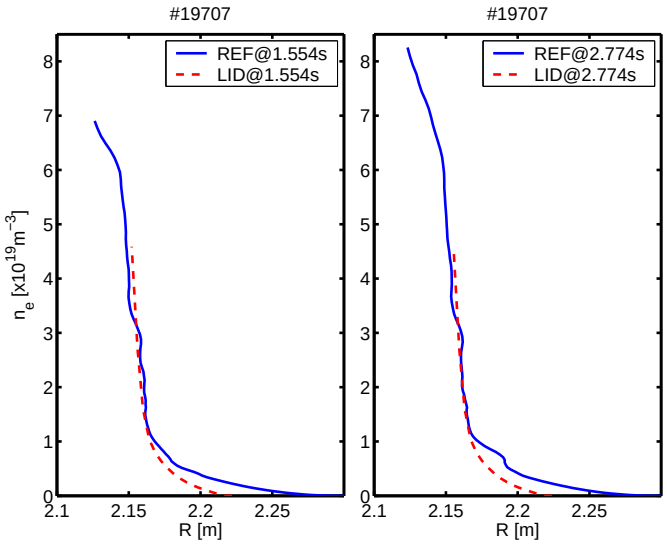

Figure 4.20: Comparison of reflectometry (REF) with lithium beam (LID) electron density profiles for the two time instants marked in figure 4.19.

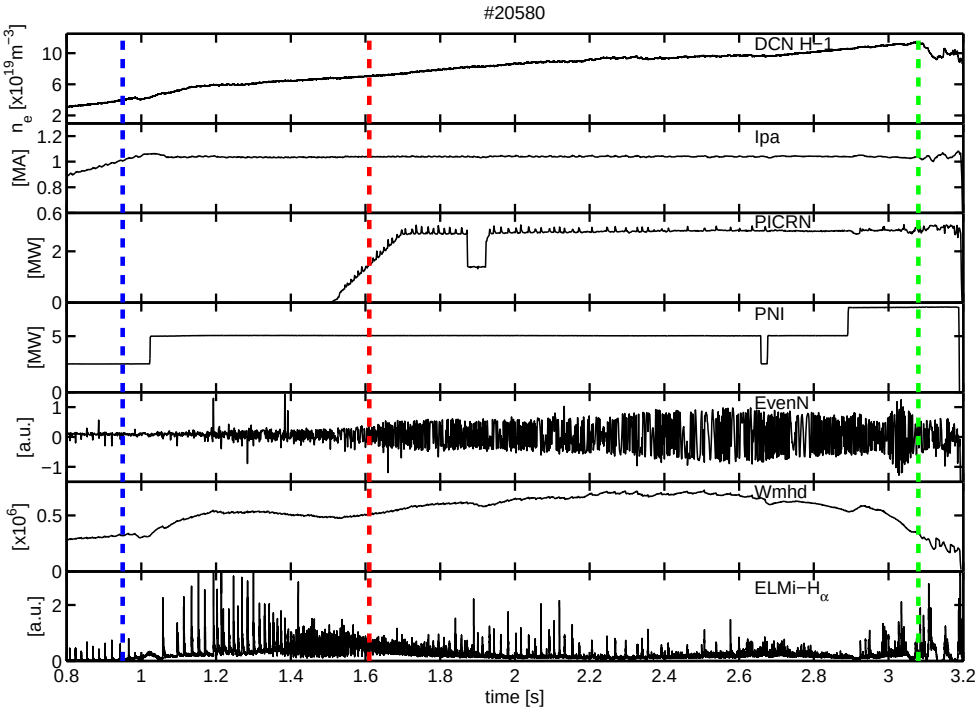

Figure 4.21: Relevant information for shot #20580. It is also marked the time position for the profiles in figure 4.22.

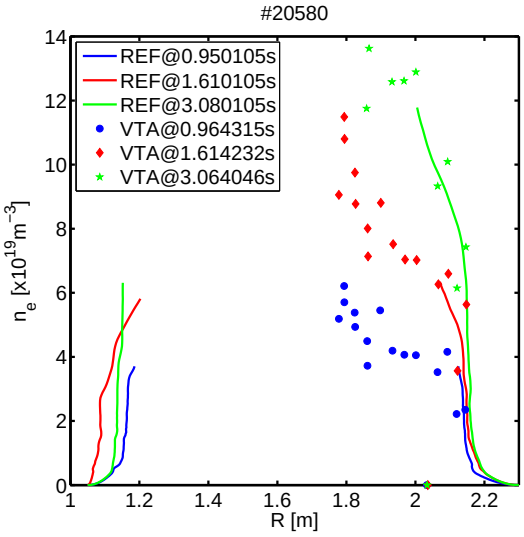

Figure 4.22: The HFS and LFS reflectometry electron density profiles (REF) for shot #20580 in different electron density ranges and comparison with the vertical Thomson Scattering data (VTA).

4.6 Fast density profile changes

Another important characteristic of the reflectometry diagnostic is the capability to respond to fast electron density profile variations. To test its performance we analyse two situations:(i) L to H transition; (ii) the ELMy phase of an H-mode plasma.

4.6.1 L to H transition

The H-mode is a regime of enhanced confinement occurring in a toroidal confinement systems [8][9]. The occurrence of a steep edge gradients of temperature and density during the H-mode leads to a specific MHD instability, the so-called edge localized modes (ELMs) which expel energy and particles from the plasma edge [10]. The H-mode with edge localized modes (ELMs) is considered the most promising regime of enhanced confinement for steady state operation in a future reactor-size magnetic fusion experiment. Although significant progress has been made in characterizing various H-mode phenomena [11] there is still a lack of predictive theories for the H-mode operating regime (e.g. power threshold and ELM type). This is especially important as ITER will have to work at comparatively high density, whereas most of experimental knowledge about H-mode has been acquired at low to medium density. Therefore, dedicated experiments to study the H-mode at high density have been carried out in ASDEX Upgrade. With the development of new diagnostics and the improvement of temporal and spatial resolution of relevant measurements in ASDEX Upgrade, namely from microwave reflectometry, it is possible to

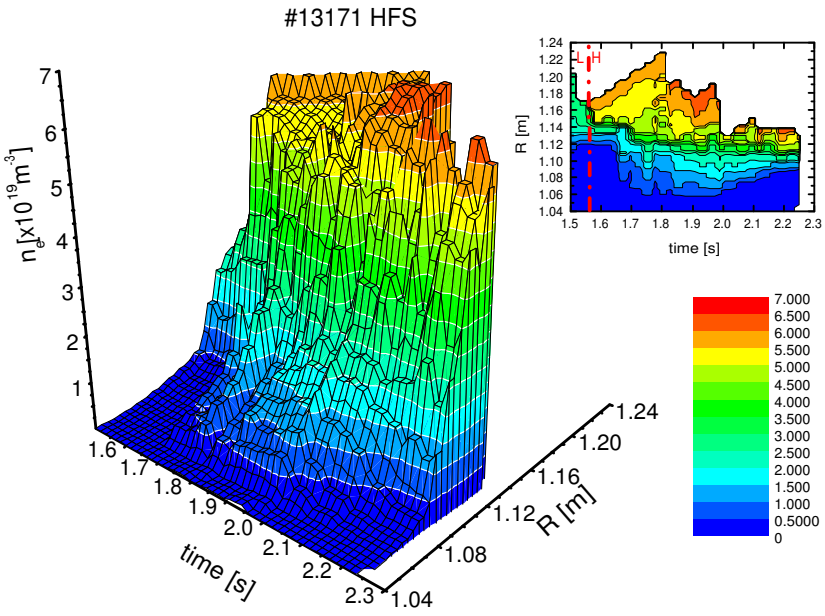

Figure 4.23: Three-dimensional plot of the evolution of the reflectometry density profiles for shot #13171, covering the L to H transition.

gain new insight into the physical phenomena governing the behaviour of H-mode plasmas and to analyze the physical mechanisms responsible for ELMs and to describe the loss of particles and energy from the plasma.

Figure 4.23 shows the evolution of the density profile between 1.5 and 2.24 s. The initial movement of the density layers corresponds to significant changes of the density profile which are expected in view of the increase of the average density, as given by the interferometer (figure 4.6(a)).

4.6.2 ELMs

Density profiles were measured during type I Edge Localized Modes (ELMs) [12] in an H-mode discharge #5903. Figure 4.24 shows the abrupt changes of the density profile at the high-field side due to the ELMs, occurring with a periodicity coinciding with the Hα radiation bursts at the divertor; at the low field side a similar behaviour is observed.

The density profiles presented in figure 4.25, show a profile flattening at the edge during the ELM, corresponding to an increase of the density outside the magnetic separatrix and a decrease inside. Between ELMs the profile recovers the steep gradient ($\nabla n_e \geq 1.0 \times 10^{21}\ m^{-4}$), typical of the H-mode transport barrier region [13]. Li-beam measurements at LFS (for a similar H-mode discharge) give the same two typical profile shapes (during and between ELMs) that cross close to the separatrix, at a value

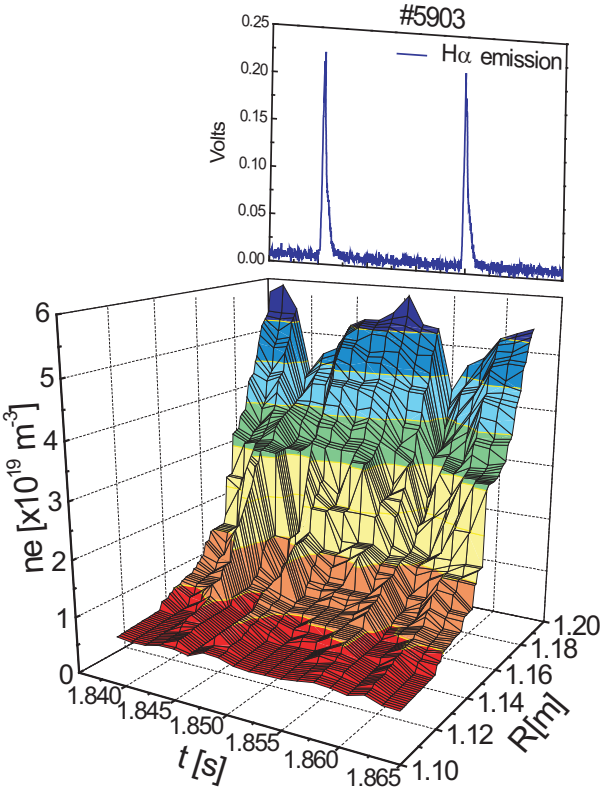

Figure 4.24: Three-dimensional plot of the evolution of the reflectometry density profiles for shot #5903(at the high field side), during the time window (1.835-1.865 s). H_α emission shows the occurrence of ELMs

$n_e \approx 3.5 \times 10^{19}\ m^{-3}$ given by reflectometry (figure 4.25). The edge profile flattening due to the ELMs measured by reflectometry can also be inferred from DCN interferometry data.

4.7 Simultaneous high field/low field side density profile measurements from reflectometry during inboard pellet launch experiments

We have shown that profile measurements can be performed in the presence of plasma turbulence. However, there are extreme plasma situations when reflectometry signals can be greatly affected by the plasma turbulence that should be tested to assess the limits of profile measurements. One such situation is during pellet injection experiments because the pellets induce strong plasma movements together with broadband turbulence associated with ELMs. We analyzed experiments with a advanced fuelling method,

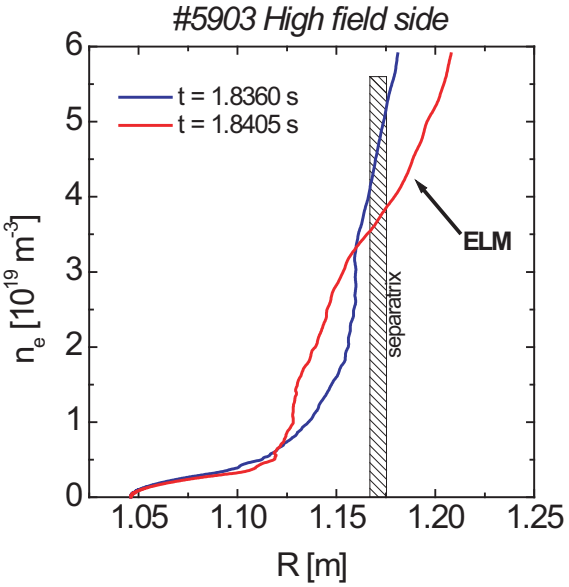

Figure 4.25: Electron density profiles from reflectometry otained for shot #5903 at the high field side, by sweeping the complete range of frequencies (16-72 GHz) in $\Delta t = 20\mu s$ during an ELM (t=1.8405 s) and in between ELMs (t=1.836 s).

consisting of pellet injection from the high magnetic field side (HFS), allowing particle deposition deep inside the core plasma. The experiments have been performed in target H mode plasma shot #14024 where 25 pellets were injected (1.8 s - 2.8 s) at 560 ms^{-1}, with 30 Hz repetition rate. The profiles were measured each 1 ms. Figure 4.26 a) and b) depicts the temporal evolution of the reflectometry group delay for two probing densities, $n_e = 4.54 \times 10^{19} m^{-3}$ and $n_e = 2.67 \times 10^{19} m^{-3}$ at the LFS, in shot #14024 (vertical lines correspond to the times of the injection of the pellets). No significant effect on the group delay is observed for lower density, which is located near the separatrix ($n_{e(sep)} \approx 3.0 \times 10^{19} m^{-3}$). This confirms previous results showing that the pellet injections do not affect the density profile at the plasma edge (figure 4.27) and do not degrade the plasma confinement.

For the higher densities (figure 4.26 a)) the group delay is strongly reduced following the pellet injection associated to the edge density gradient steepen (figure 4.27). After pellet injection, the group delay remains unchanged during a time of typically [6 - 15] ms and after it increases revealing a flattening of the profile, which corresponds to energy and particle losses. After the pellet injection the density profile steepens, both at HFS and LFS, close and inside the plasma separatrix (figure 4.27). When a pellet is injected, the density layer moves outward and the decay length decrease indicating the peaking of the profile (figure 4.28). During some millisecond after the pellets, the profile stiffness is maintained and after the plasma starts to flatten. This phenomena could be explained by

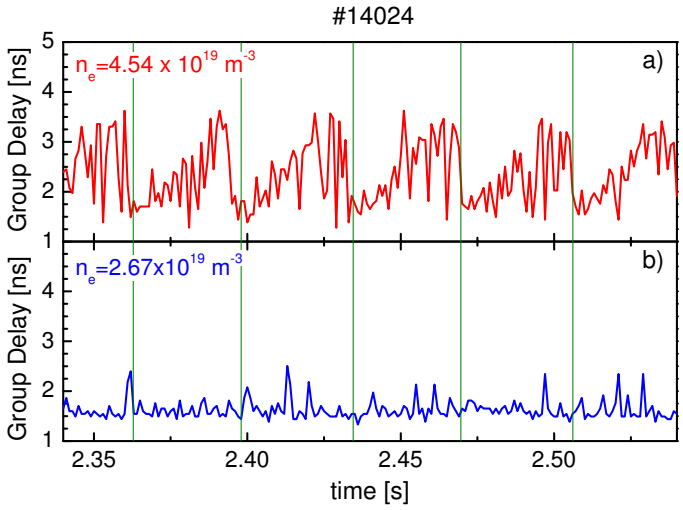

Figure 4.26: Temporal evolution of τ_g in discharge #14024 at LFS for: a) a probing layer inside the separatrix ($n_e = 4.54 \times 10^{19} m^{-3}$) ; b) a probing layer near the separatrix ($n_e = 2.67 \times 10^{19} m^{-3}$).

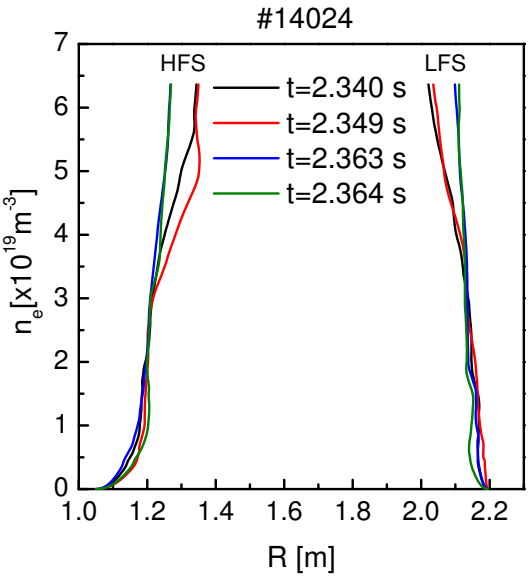

Figure 4.27: Density profiles evolution at HFS and LFS for discharge #14024.

the effects associated with strong ELMs induced by the pellets. After this confinement degradation the profile starts to recover a few millisecond before the next pellet, peaking further when the pellet occurs.

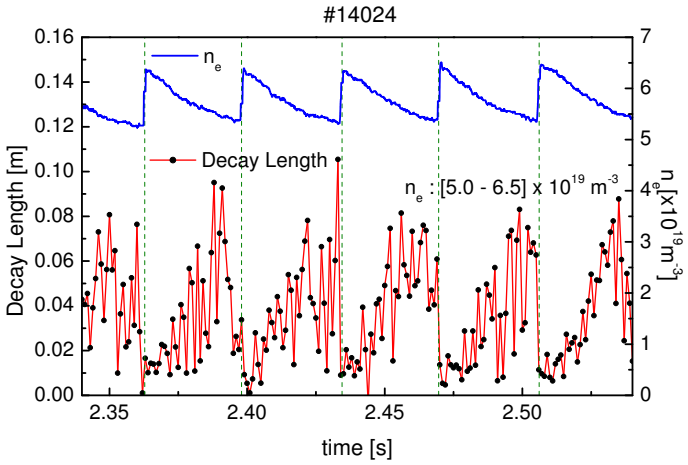

Figure 4.28: Evolution of the decay length at the density range $n_e = [5.0 \leftrightarrow 6.5] \times 10^{19} m^{-3}$ and the evolution of the average density from DCN interferometer.

4.7.1 Detailed behaviour of the edge profile in ELMy H-mode regimes

A detailed picture of edge profile dynamics under ELMs was studied before in [14]. It can be obtained with improved accuracy and extended to higher frequencies as presented in Fig. 4.29. The density time traces show clearly two distinct regions separated by $\approx 1\,cm$ around $2.17\,m$. This should be the position of the last closed flux surface, separating the pedestal ($< 2.17\,m$) and the SOL ($> 2.17\,m$) and corresponding to a turning point in the density profile [14]. The SOL density increases (within $100\,\mu s$) during the ELM (period of enhanced H_α light emission $\approx 2 - 3\,ms$) in agreement with the enhanced transport. The high SOL density is maintained during the ELM, but is back to pre-ELMs values immediately after the end of the period of enhanced H_α light emission. The density in the pedestal (inside the turning point) also collapses very quickly, within $100\,\mu s$ time scale, but recovers more slowly to the pre-ELM values ($\approx 10 - 20\,ms$). This means that the confinement in the pedestal is good between ELMs, allowing the profiles to recover, but poor during the ELMs. This is consistent with the expected picture of the density evolution in the pedestal and SOL regions during the ELM cycle. At the HFS, however, the picture looks more complex: like in the LFS, the density collapse in the pedestal at the ELM onset is rapid as expected and the recovery of the pedestal density in between ELMs is also similar to the LFS. The difference is in the SOL density in the HFS. At the HFS, the raised density level lasts for a longer period of time around 4 ms after the ELM onset and 1- 2 ms after the H_α signal has gone back to the pre-ELM levels. Then, there is a sudden decrease correlated with a small H_α response. This is an unexpected finding that raises important questions: why does the SOL HFS density lasts longer than in the

LFS and what causes the small secondary spike in the H_α data? The results may suggest that the time scales in the SOL are different in the HFS and LFS but no definitive answer can be given without further investigation. It should also be noted that the reflection from the high density layers probed with W band from the LFS start at $t \approx 2.42\,s$ for the $n_e = 6.5 \times 10^{19}\,m^{-3}$ and $t \approx 2.428\,s$ for the $n_e = 7 \times 10^{19}\,m^{-3}$ following the sudden increase of plasma density due to the injection of a pellet at $t \approx 2.42\,s$.

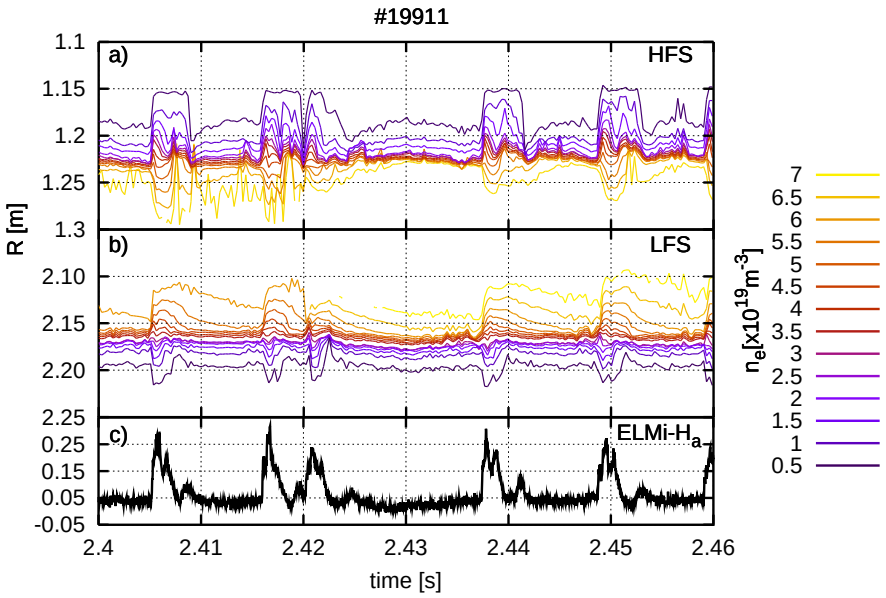

Figure 4.29: Time evolution of different electron density layers for shot # 19911: a) For the HFS; b) For the LFS. c) The D_α signal for the same time interval.

4.8 Fixed frequency measurements

Reflectometry can provide localized information about density fluctuations due its increased sensitivity near the cutoff layer. In order to measure density fluctuations the reflectometers are usually operated in fixed frequency and either the phase is measured (with heterodyne I/Q detection) or a quantity $\delta(E\sin(\phi))$ is obtained (with homodyne or single ended heterodyne detection). The reflectometry system in ASDEX Upgrade can measure density fluctuation with all the broadband channels operating at fixed frequencies and it is also equipped with two dedicated channels (in Q and V, O-mode bands) operating only in fixed frequency. They can be also used to monitor routinely the transition from L-mode to H-mode regime from the drop of the fluctuations power in the detected signal at a selected frequency range. Although the information about the plasma fluctuations provided by the measurements are limited due to the fact that the phase is not

obtained separately, it gives important characteristics of the plasma fluctuations namely its localization and frequencies. In this following we give some examples showing the great capabilities of the reflectometry to measure density fluctuations that derive from the possibility to use several channels and to localize the cutoff layers from the high resolution density profiles obtained with the broadband channels operating in sweep mode.

4.8.1 The L to H transition

In figure 4.30 it is shown the H_α signal and the intensity spectrum of the Q-band reflectometer using two different windows of analysis: (a) the power was computed in the range 100 - 200 KHz and (b) in the range 200 - 300 GHz.

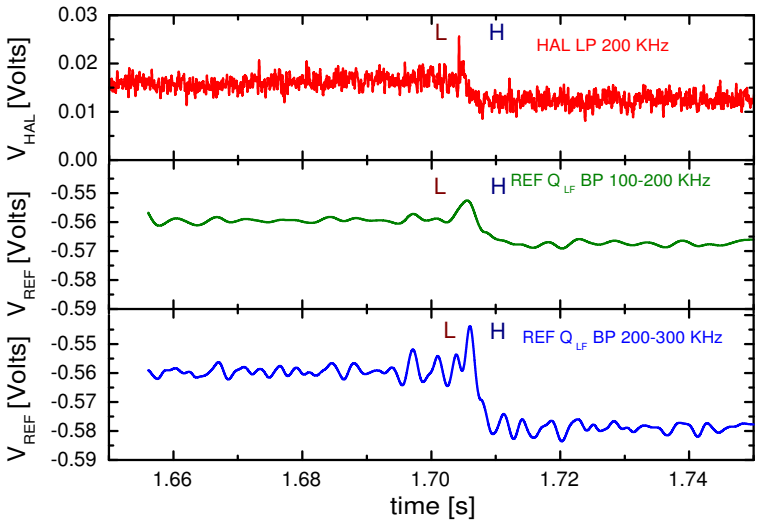

Figure 4.30: The L-H transition seen by the fluctuation monitor. a) The H_α signal showing the L-H transition. b) and c) The reflectometer fluctuation intensity signal for two different fluctuation bands for the same L-H transition.

Although the L-H transition can be clearly resolved from the abrupt decrease of the fluctuations level inferred from intensity spectrum of the reflectometer signal occurring at $t \approx 1.706\,s$, in agreement with the data from the H_α signal, it is more clearly resolved if the power spectrum is calculated in the range 200 - 300 GHz. This shows that the high frequency spectrum of turbulence is the more sensitive indicator to detect the L - H transition. This method will provide therefore a useful and direct tool to give in real time the L-H transition by implementing this method in hardware with a set of band pass filters followed by an integrator.

4.8.2 Measurement of MHD activity

In H-mode ASDEX-Upgrade #9904 Edge Localized Modes (ELMs) occurred as well as large magnetic islands, namely a neoclassical 2/1 mode that decreases its frequency due to the exchange of momentum with the wall. When the phase velocity is reduced to zero the mode is locked to the wall [12]. MHD activity is usually detected with external magnetic coils and here we compare the reflectometry measurements of MHD activity with the standard magnetic information. In figure 4.31a) it is displayed the H_α signal indicating

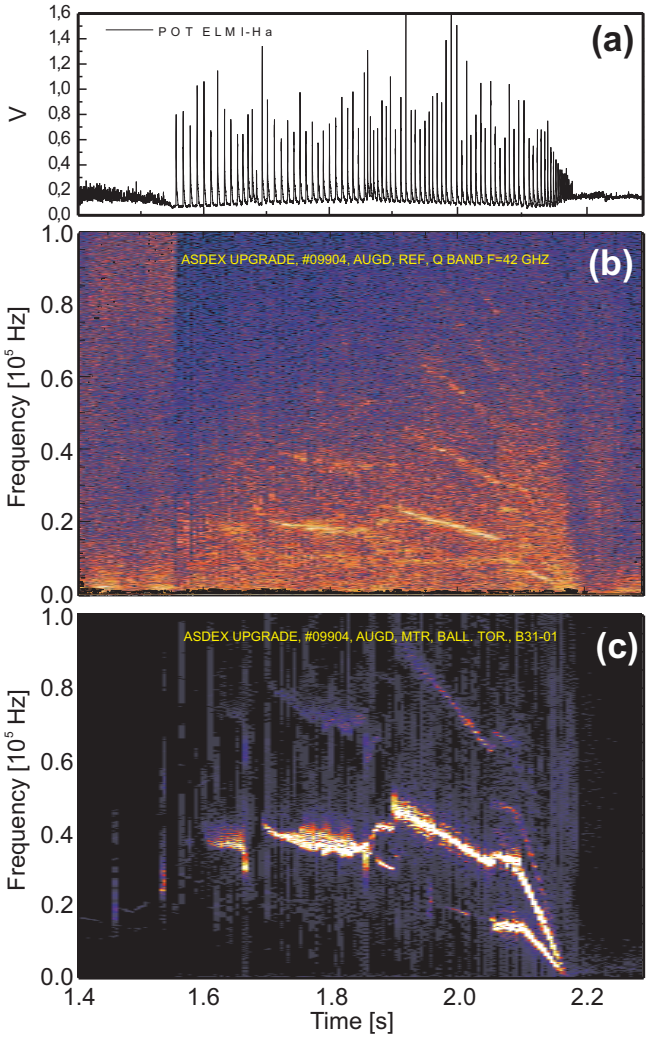

Figure 4.31: The L-H transition seen by the fluctuation monitor. a) The H_α signal showing the L-H transition. b) Time resolved power spectra of the fixed frequency reflected Q band signal at F = 42 GHz ($n_e = 2.2 \times 10^{19} m^{-3}$), obtained with a sliding Fast Fourier Transform (FFT). c) Time resolved power spectra of the magnetic signals, obtained with a sliding FFT.

the transition from L to H regime at $t \approx 1.55s$ followed by strong ELMs represented by the high amplitude frequent peaks of the H_α radiation. The time resolved power spectra of

the reflected microwave signals obtained with a sliding Fast Fourier Transform are shown in figure 4.31b) as contour plots, in the time interval 1.4 s to 2.3 s. The probing frequency was F = 42 GHz which corresponds to a reflecting layer with $n_e = 2.2 \times 10^{19} m^{-3}$. The L-H transition at $t \approx 1.55s$ is clearly seen from the abrupt drop in the level of the signal fluctuations in the frequency range 30 - 100 kHz.

After the transition, periodic broadband structures are seen in good agreement with the spikes of the H_α signal due to the ELMS. The coherent structures observed and interpreted by the magnetic diagnostics (figure 4.31(c)) are also detected by reflectometry. At $t \approx 1.65s$ a first coherent structure is revealed (at f $\approx$ 20 KHz) decreasing in frequency, which is correlated with a m=1, n=1 mode. At $t \approx 1.85s$ another coherent structure is triggered, corresponding to a neoclassical (3/2) mode. Those fluctuations subsequently decrease in frequency until at $t \approx 2.06s$ another neoclassical (2/1) mode is observed which locks to the wall (zero frequency) at $t \approx 2.19s$. Its harmonics (3,1) and (3/2) shows the same locking process.

Using density profiles obtained with the broadband channels operating in swept mode we can localize the fixed frequency cutoff layer where the measurements are being performed. As can be seen from figure 4.32, where it is displayed a density profile obtained

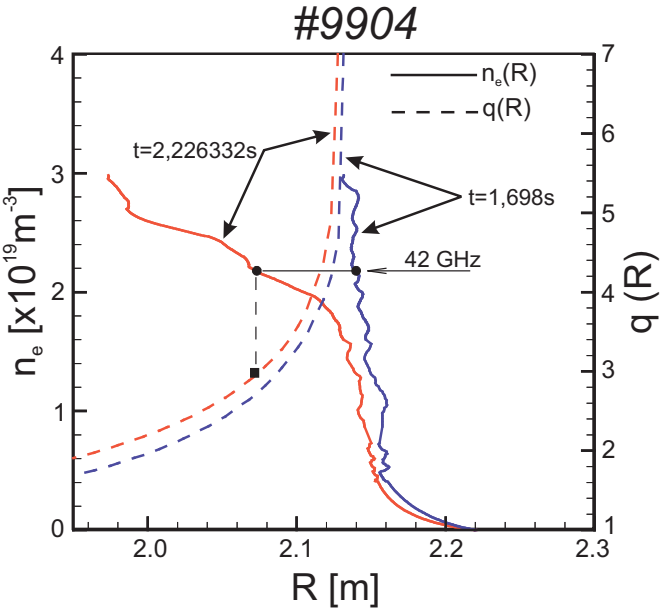

Figure 4.32: Density profiles obtained from broadband reflectometry, at t=1.698 s and 2.226 s. The location of the probed density layer by the fluctuations monitor($F = 42GHz \Leftrightarrow 2.19 \times 10^{19} m^{-3}$), is indicated both in n_e and q(r).

during the H-phase (at t = 1.698 s) and after mode locking (at t = 2.226 s), the cutoff layer moves along time. In the figure it is also shown the corresponding q-profiles esti-

mated from MHD equilibrium reconstruction. During the H phase the probed layer inside and close to the magnetic separatrix with density, $n_{sep} = 2.08 \times 10^{19} m^{-3}$, whereas in the case of mode locking the cutoff layer is close to the rational surface q = 3. These results show that some modes (measured with the magnetic diagnostics, such as the 1/1 mode) located well inside the plasma impact also at outer flux surfaces. Localization is therefore very important to study MHD perturbations.

4.9 Concluding remarks

The tests performed both in the laboratory and in the tokamak with a metallic mirror confirmed the high performance of the reflectometry system. However, with the plasma the propagation and reflection of the probing microwaves is much more complex due to the effect of the plasma turbulence and therefore a detailed assessment was made in typical plasma ASDEX Upgrade configurations.

It was demonstrated that the system is quite tolerant to plasma vertical displacements ($\mp$14 cm) which confirms the optimised design of the antennas. It is shown that the diagnostic can also resolve radial plasma displacements of some 5 mm under the presence of turbulence. When necessary the distance information can be reinforced (increase of signal to noise ratio) using burst mode measurements (sequences of individual measurements group together to give an average value) at the cost of decreased time resolution (typically 280 μs).

The measuring ranges of the diagnostic were found to be 40 cm to the HFS and 49 cm to the LFS, while density gradients between 65 and 89.5 degrees could be measured.

The analysis of the density profile initialisation show that while combined O and X wave probing should improve the profile accuracy, mainly at the plasma, the method based on O mode waves plus a linear extrapolation down to zero frequency is much simpler and provides a reasonable estimate of the edge profile.

Comparison with density data from Li-beam beam and Thomson scattering show reasonable agreement but it should be noted that reflectometry diagnostic is located at a different position in the tokamak and has a higher temporal resolution. It is also more sensitive to localized profile deformations due to the propagation close to the cutoff, such as for example due to magnetic activity.

Several studies are presented that illustrate the great capabilities of the diagnostic, namely to resolve abrupt profile changes as those due to ELMs and the L to H transition.

It is demonstrated the use of fixed frequency operation to study magnetic activity and its localization from broadband swept operation.

References

[1] T. Grossmann, I. Nunes, F. Serra, M. E. Manso, and A. Silva. Sencitivity of fast swept frequency modulation reflectometry to changes in magnetic configuration in ASDEX Upgrade. *Fusion Enginnering and Design*, (34-35):425–428, 1997.

[2] J. Santos, M. Manso, and the ASDEX Upgrade Team. Plasma position using reflectometry edge density profile measurements on ASDEX Upgrade. In *Proceedings on* 28^{th} *European Conference on Controlled Fusion and Plasma Physics*, volume 25A, pages 1241–1244. European Physical Society, 2001.

[3] J. Santos, M. Manso, P. Varela, J. Neuhauser, and the ASDEX Upgrade Team. Plasma position measurements from ordinary FM-CW reflectometry on ASDEX Upgrade. *Review of Scientific Instruments*, 74(3):1489–1492, March 2003.

[4] J. Santos, S. Hacquin, M. Manso, and the ASDEX Upgrade Team. Frequency modulation continuous wave reflectometry measurements of plasma position in ASDEX Upgrade ELMy H-mode regimes. *Review of Scientific Instruments*, 75(10):3855–3858, October 2004.

[5] R. C. Wolf, O. Gruber, R. Dux, S. Günter, A. Kallenbach, K. Lackner, M. Maraschek, H. Meister, and the ASDEX Upgrade Team. Advanced tokamak operation on ASDEX Upgrade. In *Proc. 17th Int. Conf. On Plasma Physics and Controlled Fusion Research*, 1998.

[6] I. Nunes, P. Varela, G. D. Conway, F. Silva, F. Serra, M. Manso, and ASDEX Upgrade Team. Absolute calibration of density profiles from both O and X mode reflectometry on ASDEX upgrade. In *Proceedings on* 28^{th} *European Conference on Controlled Fusion and Plasma Physics*, volume 25A, pages 1249–1252. European Physical Society, 2001.

[7] P. Varela, M. E. Manso, A. Silva, J. Fernandes, and F. Silva. Initialization of plasma density profiles from reflectometry. *Review of Scientific Instruments*, 66(10):4937–4942, October 1995.

[8] F. Wagner, G. Becker, K. Behringer, D. Campbell, A. Eberhagen, W. Engelhardt, G. Fussmann, and The ASDEX team. Regime of improved confinement and high beta in neutral-beam-heated divertor discharges of the ASDEX tokamak. *Physical Review Letters*, 49(19):1408–1412, 1982.

[9] The ASDEX team. The H-mode of ASDEX. *Nuclear Fusion*, 29(11):1959–2040, November 1989.

[10] H. Zohm. The physics of edge localized modes (ELMs) and their role in particle and power exhaust. *Plasma Phys. Control. Fusion*, 38:1213–1223, 1992.

[11] W. J. Connor and H. R. Wilson. A review of theories of the L–H transition. *Plasma Phys. Control. Fusion*, 42(1):R1–R74, January 2000.

[12] John Wesson. *Tokamaks*. Clarendon Press · Oxford, 1987.

[13] W. Suttrop, O. Gruber, B. Kurzan, H.B. Murmann, J. Neuhauser, J. Schweinzer, J. Stober, W. Treutterer, and ASDEX Upgrade Team. Effect of plasma shape variation on elms and h-mode pedestal properties in ASDEX upgrade. *Plasma Phys. Control. Fusion*, 42:A97–A102, 2000.

[14] I. Nunes, G.D. Conway, A. Loarte, M Manso, F. Serra, W. Suttrop, the CFN, and ASDEX Upgrade Team. Characterization of the density profile collapse of type I ELMs in ASDEX Upgrade with high temporal and spatial resolution reflectometry. *Nuclear Fusion*, 44:883, 2004.

5 Conclusions and future work

5.1 Conclusions

A complex multichannel broadband FM-CW reflectometry system (with 11 channels) has been developed for ASDEX Upgrade with the main goals of measuring the plasma profile and density fluctuations simultaneously at the high and low field sides (LFS/HFS), aiming to contribute to the understanding of confinement and transport in the ASDEX Upgrade plasma, in particular in ITER relevant scenarios such as improved H-mode regimes.

The diagnostic should also be used to develop and fully demonstrated new measuring techniques required for ITER, such as the control of plasma position and shape using reflectometry measurements.

The system is now routinely providing electron density profiles with a minimum temporal spacing of 30 μs. The plasma is probed from zero density to $n_e = 12.3 \times 10^{19} m^{-3}$ at the LFS with combined O and X-modes, and from $n_e = 0.32 \times 10^{19} m^{-3}$ to $n_e = 6.64 \times 10^{19} m^{-3}$ at the HFS using O-mode.

In this work we address the design of the FM-CW reflectometry diagnostic and the implementation of solutions to achieve the goals required mainly by the density profile measurements.

The system was planned to measure either density profiles (distance versus density measurements obtained with broadband swept operation) or fluctuations (fixed frequency operation) with the same reflectometer channels.

The most demanding requirements in terms of system performance are, by far, the swept measurements to obtain the density profile also essential to localize the plasma layers where the fluctuations are studied with fixed frequency operation. Therefore the diagnostic has been primary designed for highest performance in broadband swept operation.

The broadband FM-CW system previously developed for ASDEX revealed the great capabilities of reflectometry to perform density measurements enormous but it also revealed the difficulties to make such measurements in the presence of strong plasma turbulence. As the level of turbulence in ASDEX Upgrade was expected to be higher than

in ASDEX (due in particular to higher heating power) and in addition the plasma shape could vary significantly (single null and double null configurations), the design utilized before for the reflectometry diagnostic on ASDEX had to be significantly modified. The system incorporate both hardware and software novelties to improve performance, namely microwave technologies; frequency calibration and testing; data analysis methods adapted to the characteristics of the wave propagation in the fusion plasma.

A big challenge to be faced for the first time was the installation of reflectometer channels (with in-vessel antennas) at the high field side of the machine.

Regarding hardware the system was equipped with (i) unity generators using solid state sources compatible with ultra fast broadband operation; (ii) emitting-receiving antenna specially designed to account for the antenna-plasma interaction in most relevant ASDEX Upgrade plasma scenarios; (iii) frequency markers plus a delay line to accurately obtain the dynamic frequency calibration of the oscillators in ultra fast swept operation, which proofed to be of crucial importance to obtain accurate distance measurements.

We build a robust system with high performance (low level of spurious reflections), optimized for reception, which is achieved with a mono-static configuration of in-vessel antennas and operation close to the tokamak. This imposed full remote control of the diagnostic. In order to exploit the full capabilities of the diagnostic a control system was designed including dedicated electronics that gives the possibility to operate the reflectometry diagnostic both in swept and fixed frequency operation in a most flexible way. A dedicated data acquisition system handles the large amounts of data generated by the diagnostic.

Here we present a comprehensive analysis of the performance of the diagnostic taking into account its design options documented with experimental results obtained in a wide range of plasma regimes. A detailed assessment of the system performance in vacuum (both in the laboratory and with in vessel measurements with a metallic mirror placed inside the tokamak) is presented that demonstrated the accuracy of the absolute distance measurements to be within some millimetres. We address several questions, in particular the measuring range of the antennas and the range of density gradients. It is shown that it is possible to obtain a detailed evolution of the density profile and density gradient even in the presence of turbulence, providing that sufficient data can be extracted from the plasma. The radial movements of the plasma can be measured with great accuracy, which is especially important for the use of reflectometry for plasma position control, as is proposed for the ITER.

The understanding of the signals reflected from the turbulent plasma imposed the application of advanced digital signal processing techniques which lead to an extensive in-

vestigation that lasted more than one decade. After the combined efforts of both hardware and software developments it is possible now in ASDEX Upgrade to obtain density profiles with high spatial and temporal (30 μs) resolutions under strong turbulent regimes. The experimental results presented in this work show the great sensitivity of the diagnostic to plasma radial movements and its tolerance to vertical movements of the plasma. Density profiles measured during fast plasma events such as Edge Localized Modes (ELMs), which are accompanied by abrupt and dramatic changes of the plasma density profile as well as broadband turbulence, illustrate the capabilities of the diagnostic to measure under extreme difficult conditions, even when the probing waves should suffer significant refraction, diffraction and scattering effects.

5.2 Future work

The FM-CW system in ASDEX Upgrade although designed for plasma edge and core measurements has some severe limitations to access the plasma core either due to the high densities reached at the edge in some regimes (improved H mode and density limits) or to the flatness of density profiles beyond the edge pedestal. It will be possible to reach the core region with X mode propagation although the measurement requires external magnetic data and is very sensitive to errors in the detection of the first reflected signal when the upper cutoff is used, which may decrease the accuracy of the profile measurements. The lower cutoff can also be utilized by launching the waves from the high field side. It should be noted that this technique is proposed for ITER density profile measurements and was never tested in present machines which makes its application very important for the design of the ITER microwave diagnostics.

A present problem of the FM-CW reflectometry diagnostic is its sensitivity to the ECRH radiation which will constitute a serious danger for the diagnostic after the ongoing upgrade of the ECRH system with capability for beam steering. The critical components are the directional couplers placed inside the machine with matched loads not able to stand high RF power. A possible solution is to develop a new transmission line with a bistatic antenna configuration although it is a good option for optimized emission-reception (as described in this work) but avoids the use of the in vessel directional couplers. Taking into account the severe space constrains the new transmission line will have to be able to transmit and receive several fundamental frequency bands.

Finally, it would be challenging to extend the diagnostic to the probing of the ASDEX Upgrade plasma divertor, in spite of the severe access restrictions at the divertor and the difficulty to perform the measurements, as this technique is foreseen for ITER to

characterize plasma transport and operation as well as to optimize machine operation and was never tested in present devices.

A Microwave circuits

Schematic glossary

A	Pyramidal Horn
AMP	Amplifier
CWG	Coaxial to Waveguide Transition
D	Detector
DB	DC Break
DC	Directional Coupler
DR	Driver
FDB	Frequency Doubler
FTR	Frequency Tripler
HA	Hog Horn
IF	Intermediate Frequency Module
MX	Mixer
OSC	Oscillator
PS	Power Splitter
VW	Vacuum Window

Table A.1: Glossary for the microwave circuit schematics .

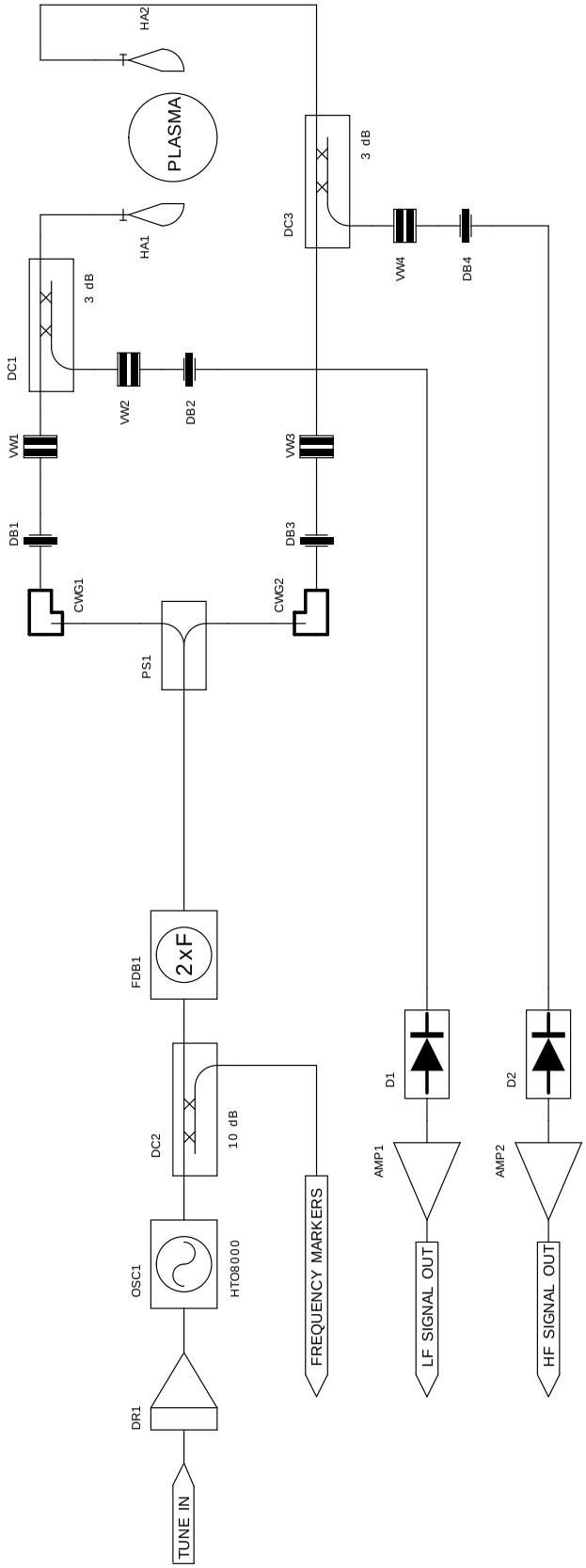

Figure A.1: Schematic of the K band microwave circuit.

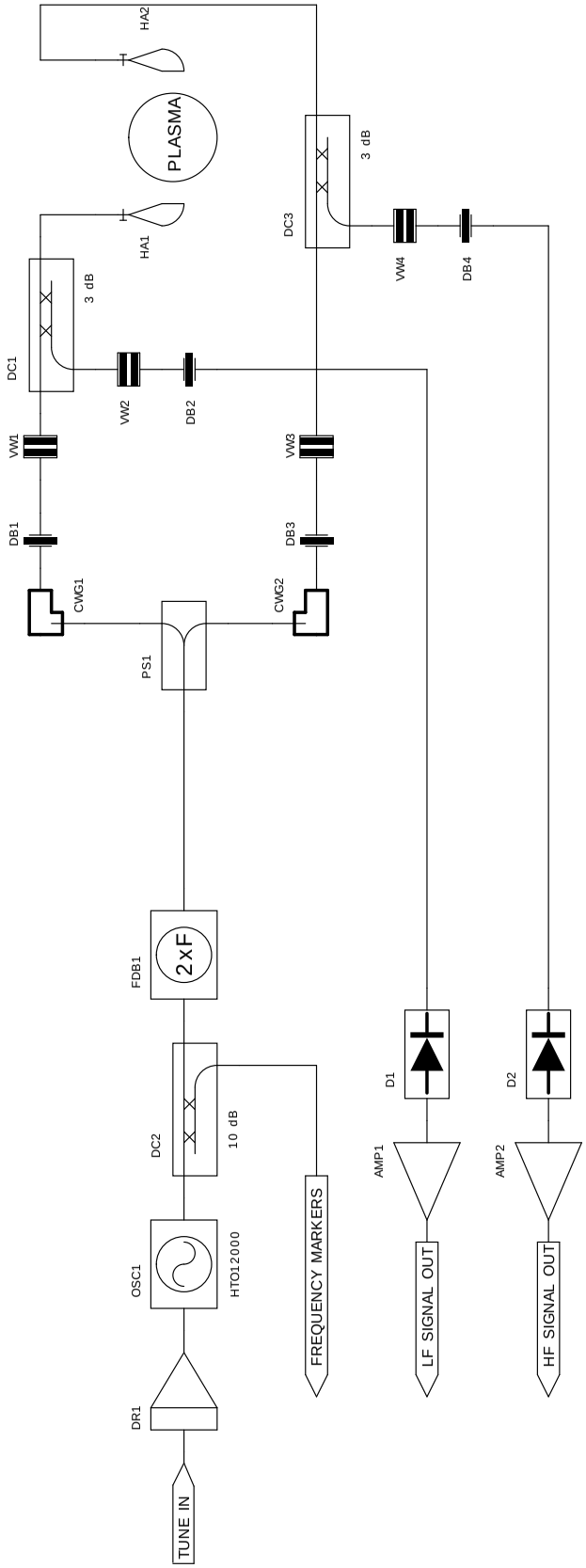

Figure A.2: Schematic of the Ka band microwave circuit.

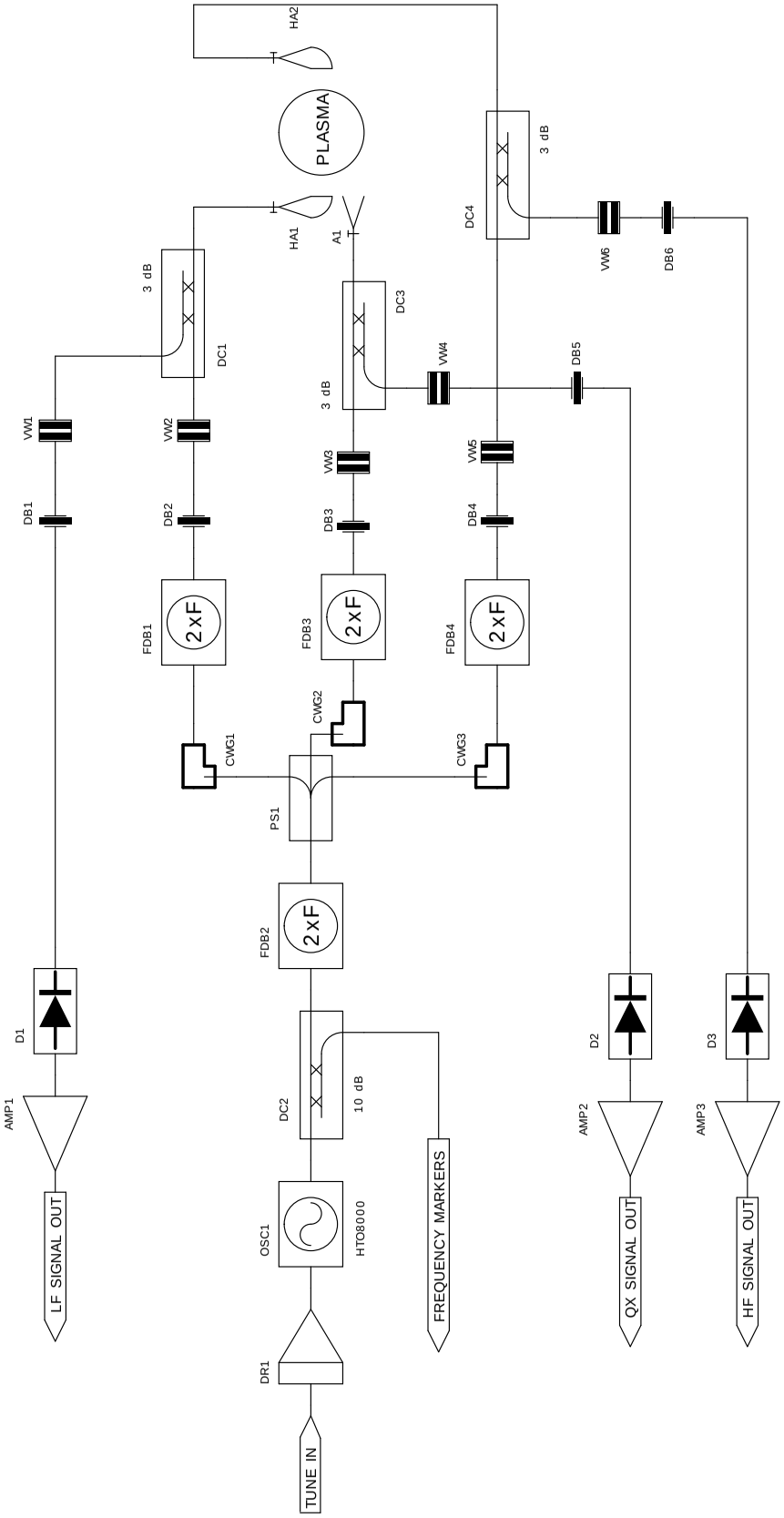

Figure A.3: Schematic of the Q band microwave circuit.

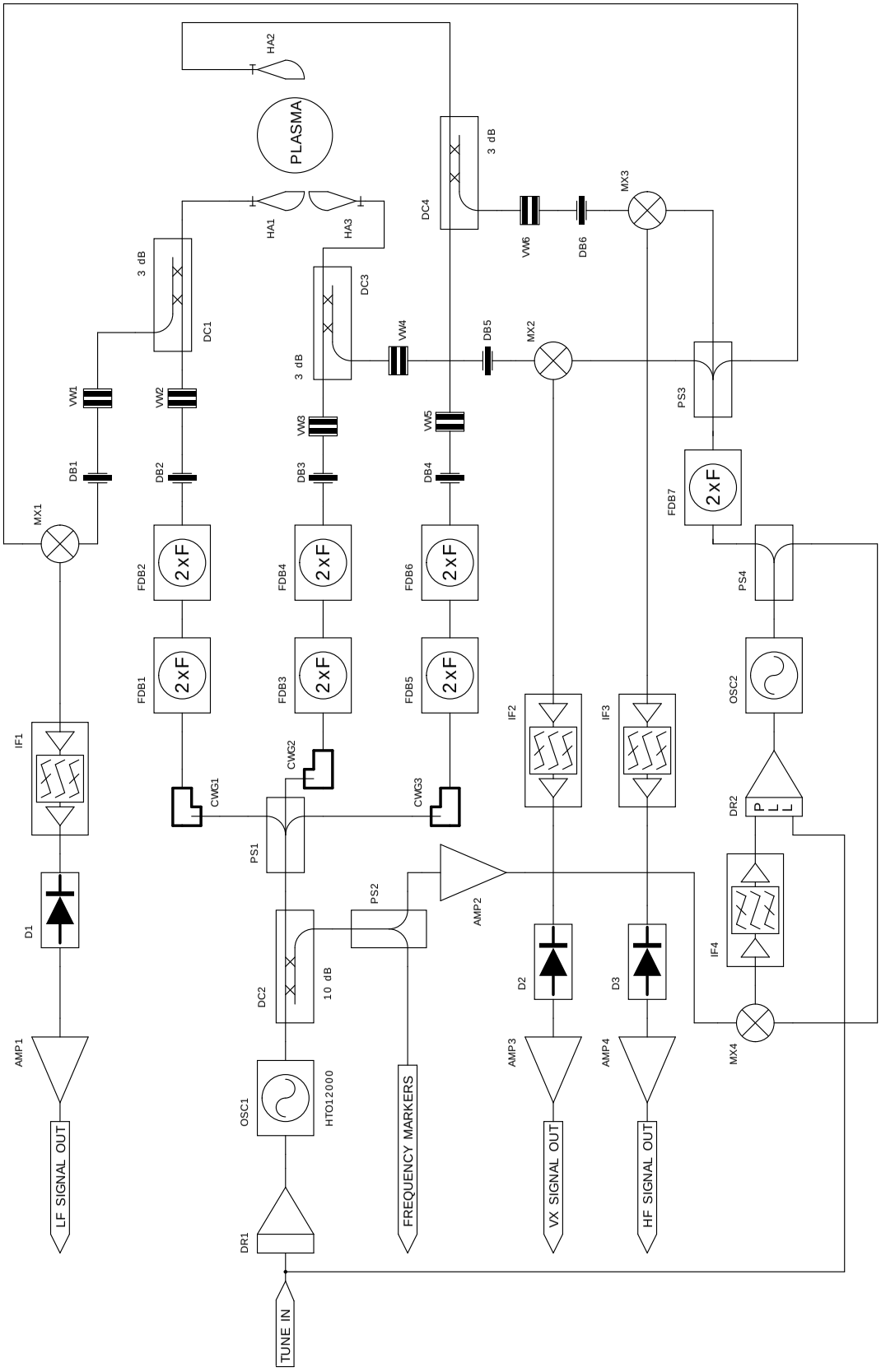

Figure A.4: Schematic of the V band microwave circuit.

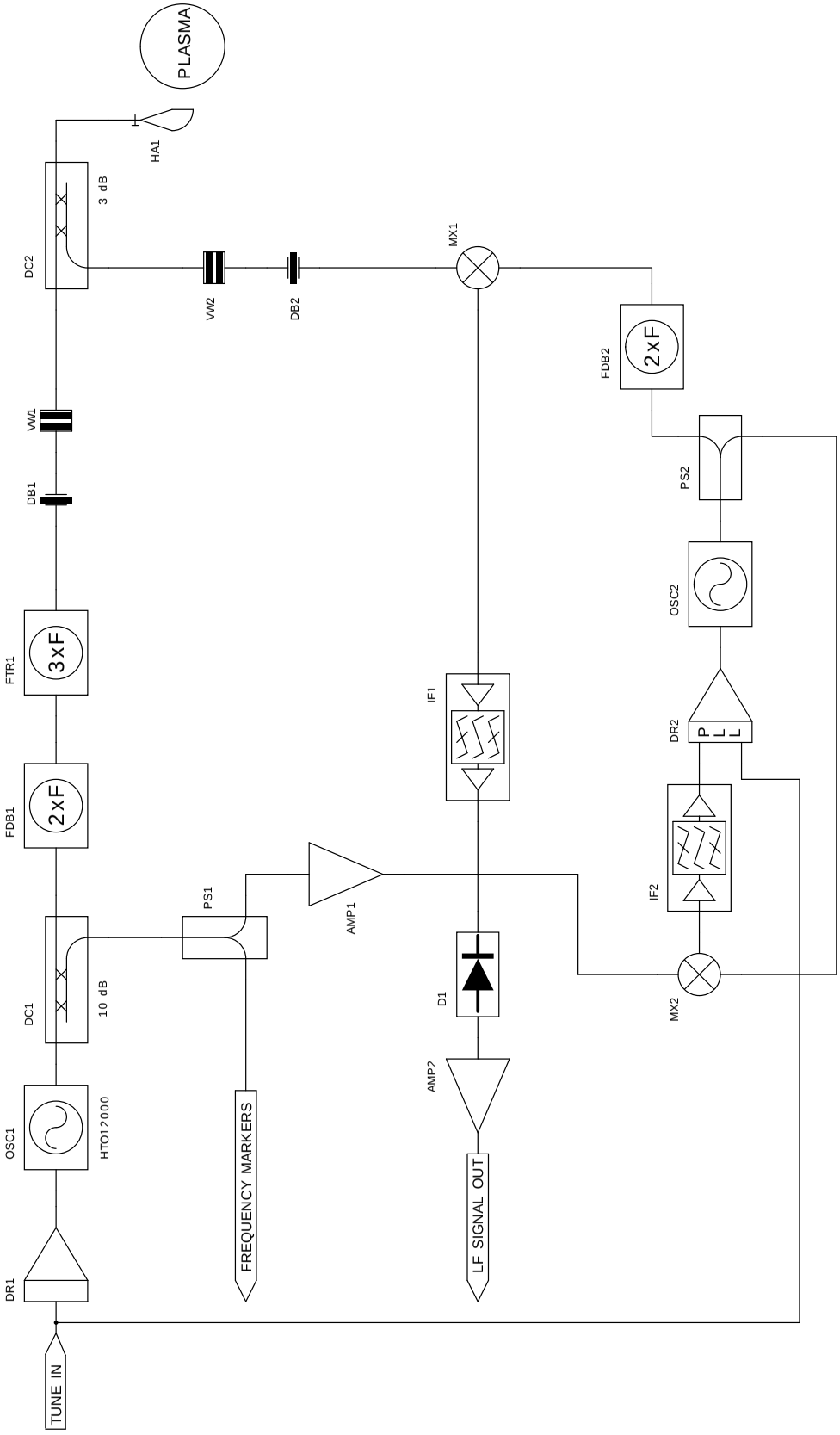

Figure A.5: Schematic of the W band microwave circuit.

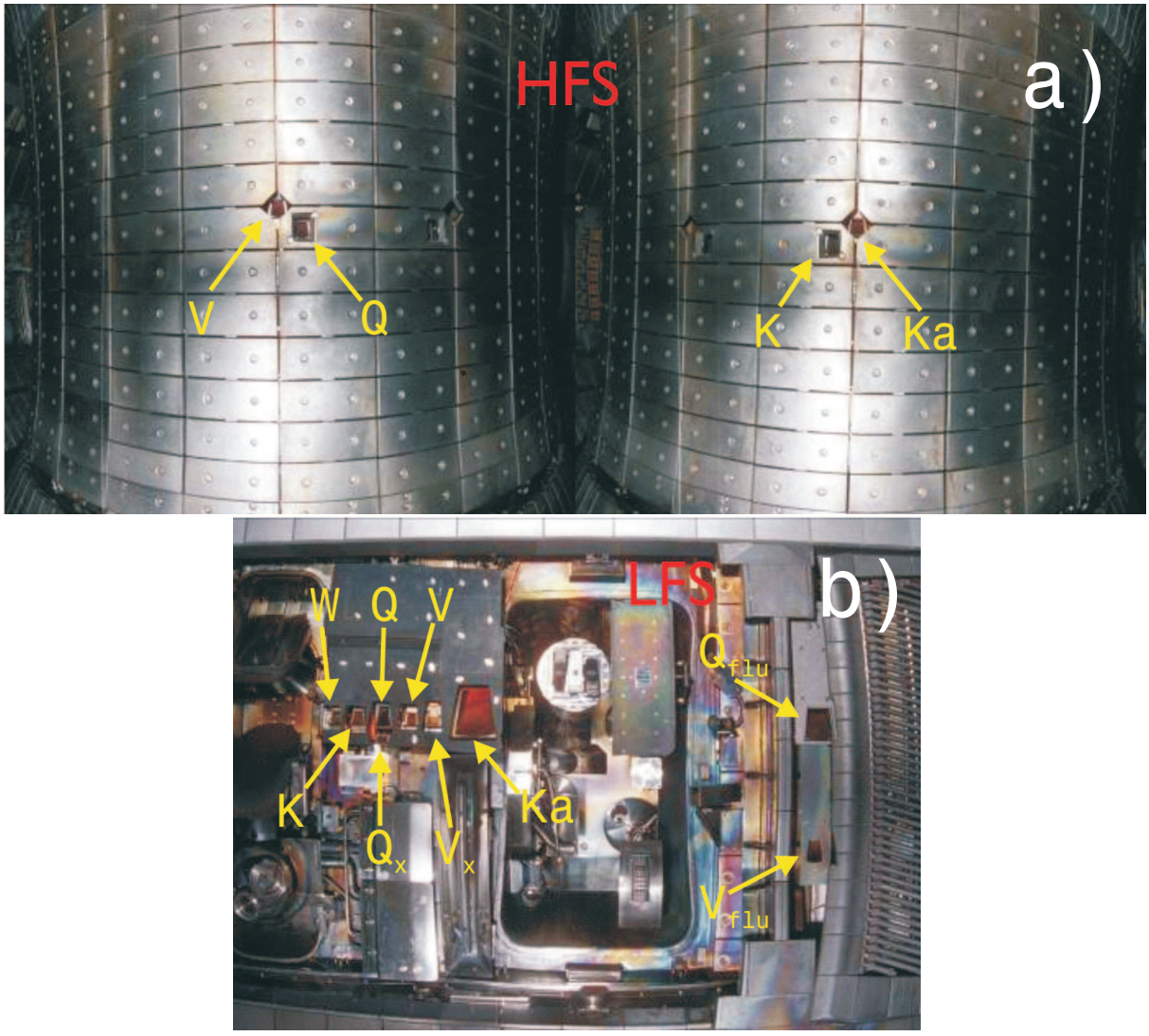

Figure A.6: Picture showing the relative position of the different antennas inside the vessel. a) On the HFS. b) On the LFS.

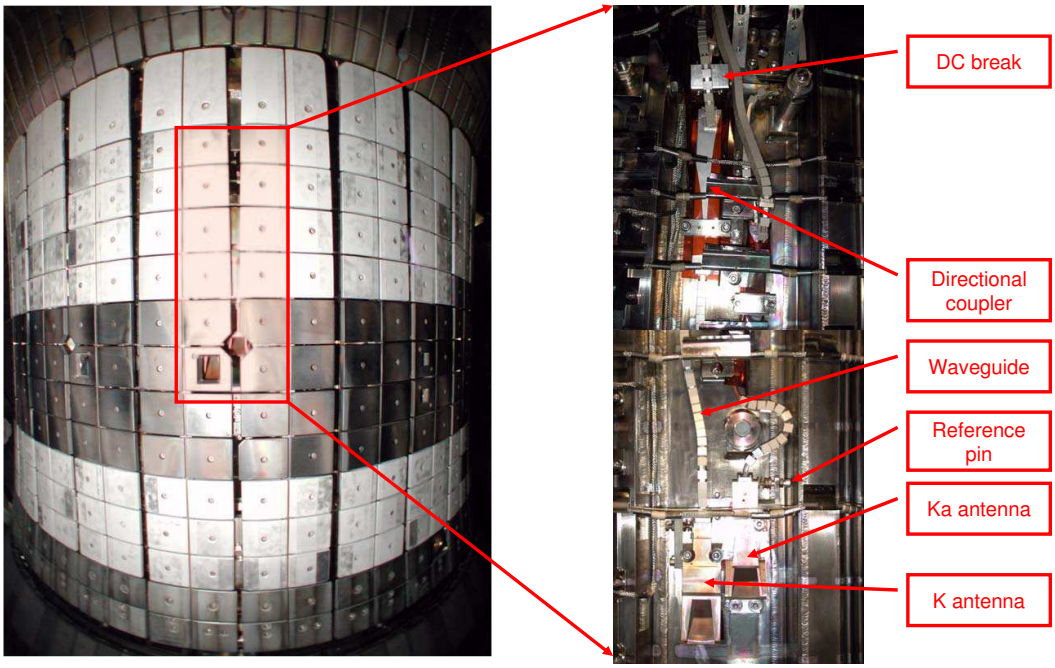

Figure A.7: Picture showing in detail the K and Ka HFS channels in-vessel setup. On the left side with the heat shield in place. On the right side with the heat shield removed, showing the antennas, the reference pins, the directional couplers and the difficult waveguide routing.

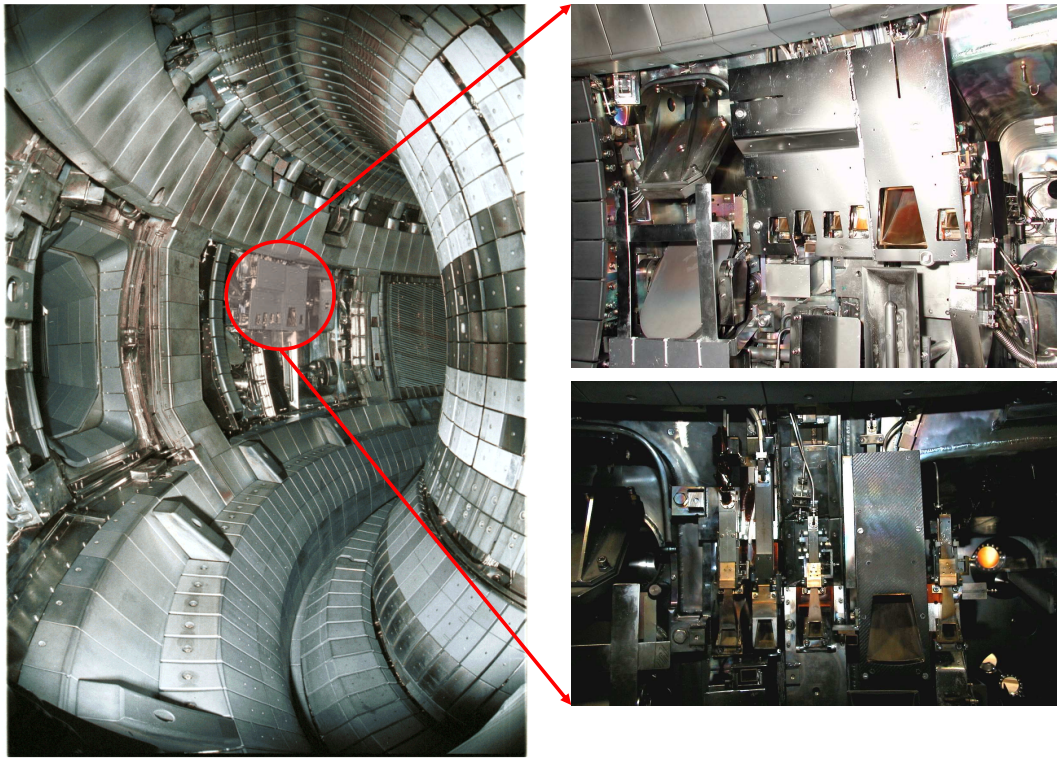

Figure A.8: Picture showing in detail LFS channels in-vessel setup. On the left side with the heat shield in place. The right side with the heat shield removed, showing the antennas, the reference pins and the directional couplers.

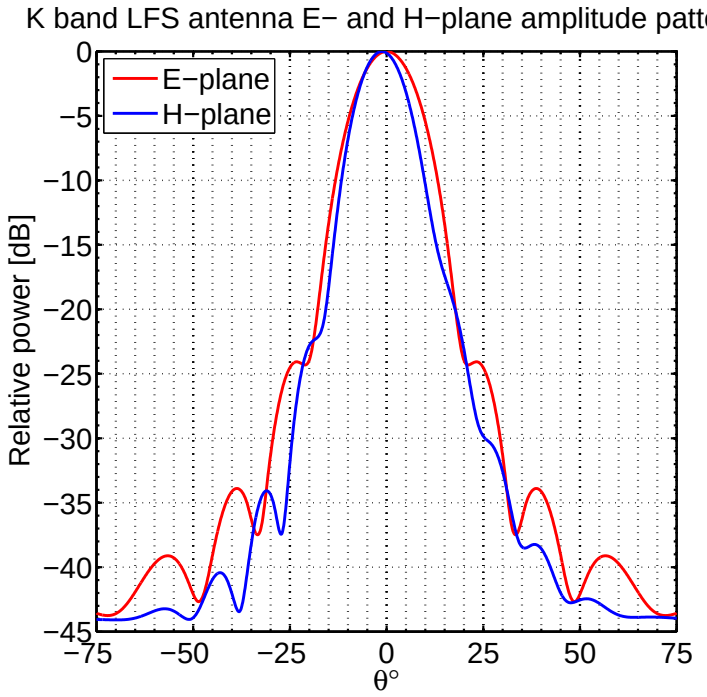

Figure A.9: Simulated radiation pattern of the K band LFS antenna.

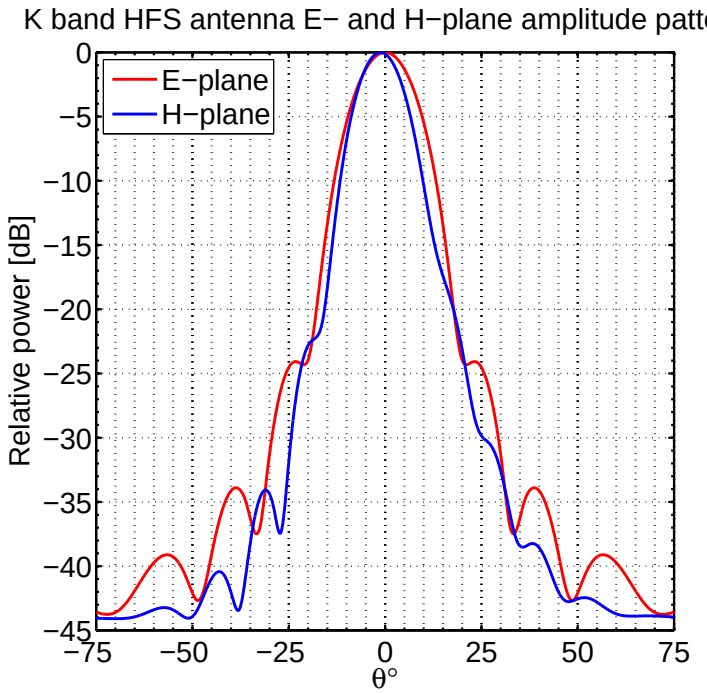

Figure A.10: Simulated radiation pattern of the K band HFS antenna.

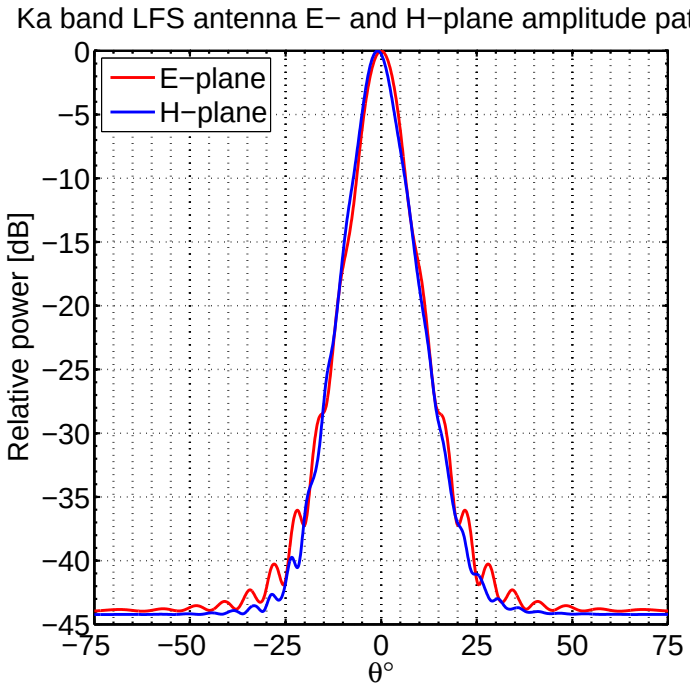

Figure A.11: Simulated radiation pattern of the Ka band LFS antenna.

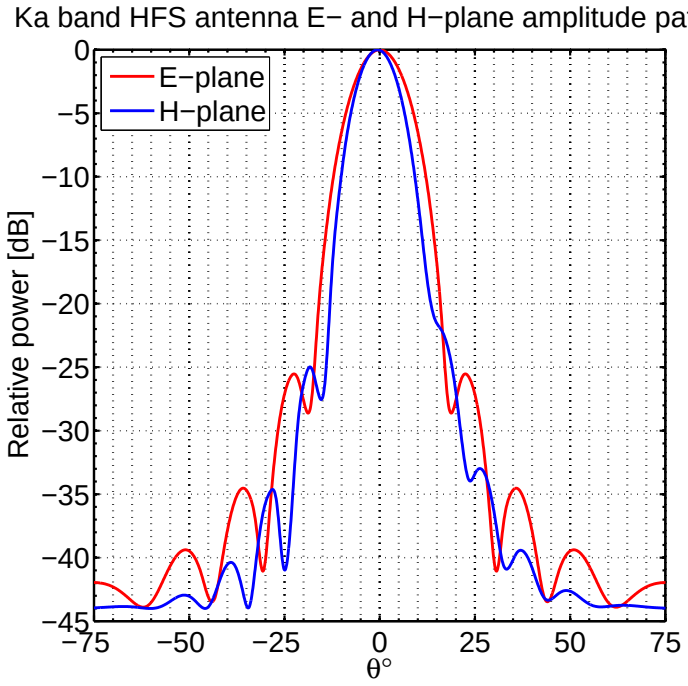

Figure A.12: Simulated radiation pattern of the Ka band HFS antenna.

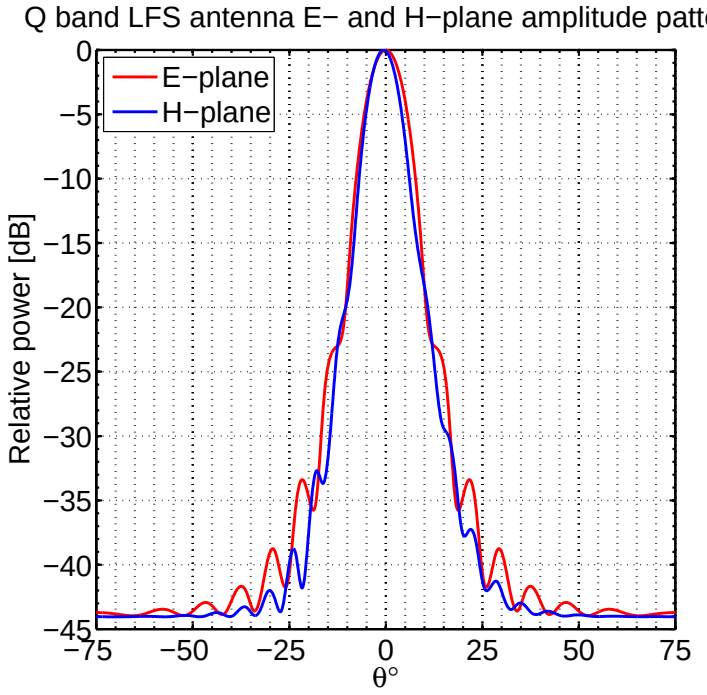

Figure A.13: Simulated radiation pattern of the Q band LFS antenna.

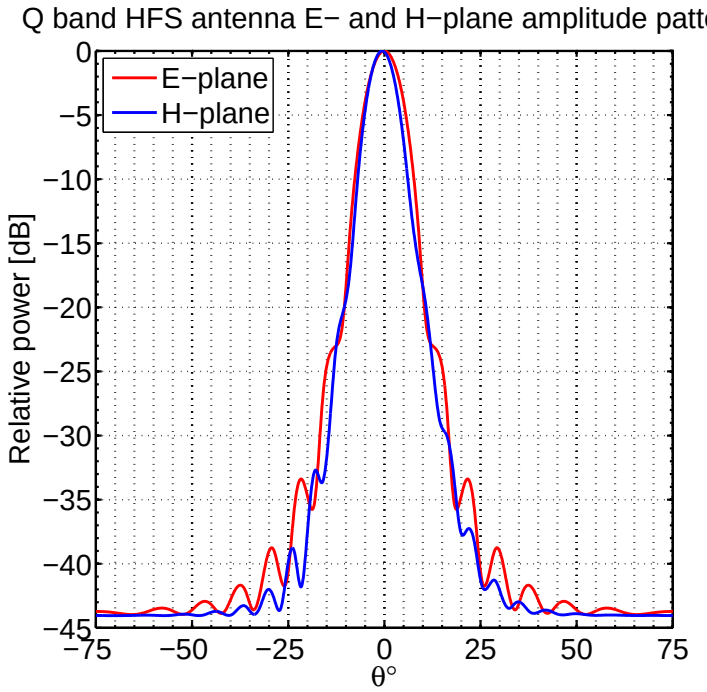

Figure A.14: Simulated radiation pattern of the Q band HFS antenna.

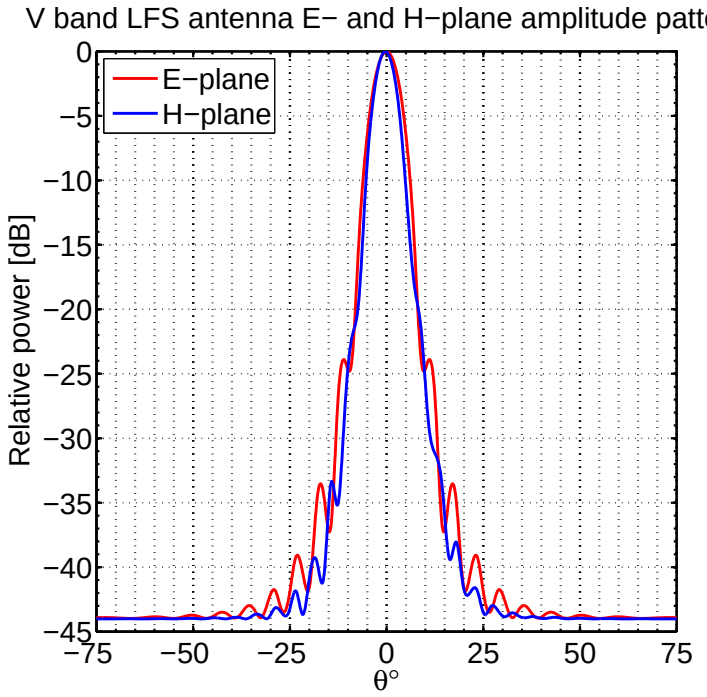

Figure A.15: Simulated radiation pattern of the V band LFS antenna.

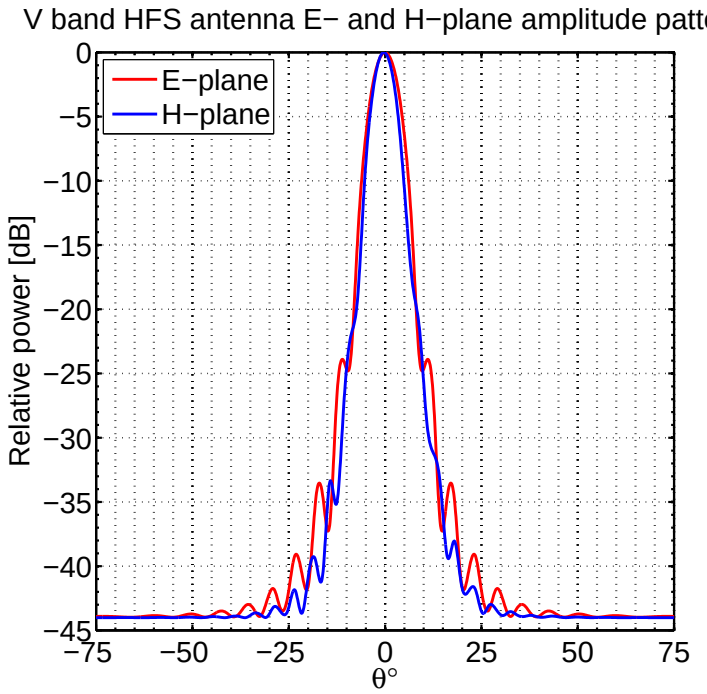

Figure A.16: Simulated radiation pattern of the V band HFS antenna.

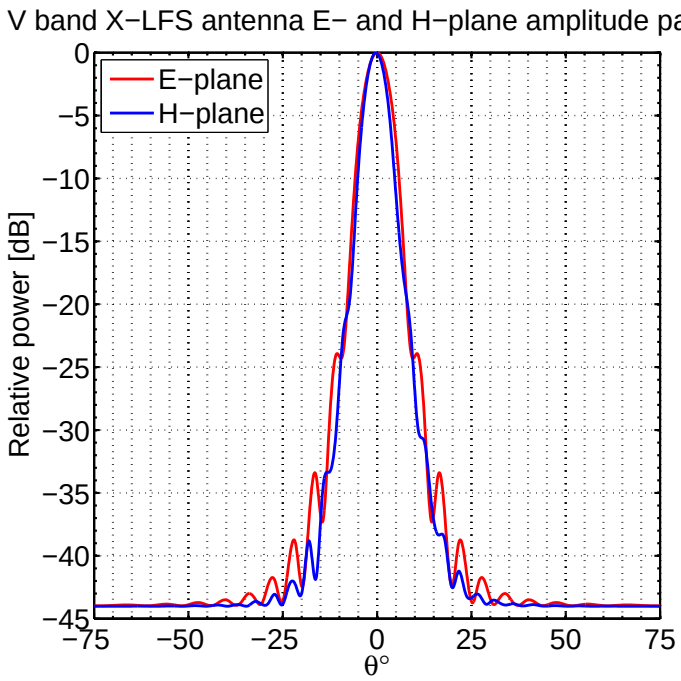

Figure A.17: Simulated radiation pattern of the V band X-mode antenna.

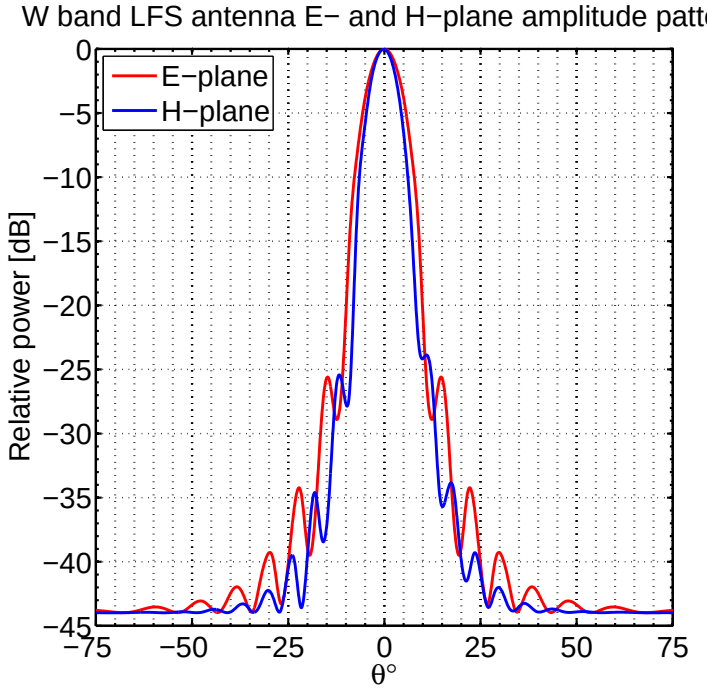

Figure A.18: Simulated radiation pattern of the W band LFS antenna.

B Fast ramp generator

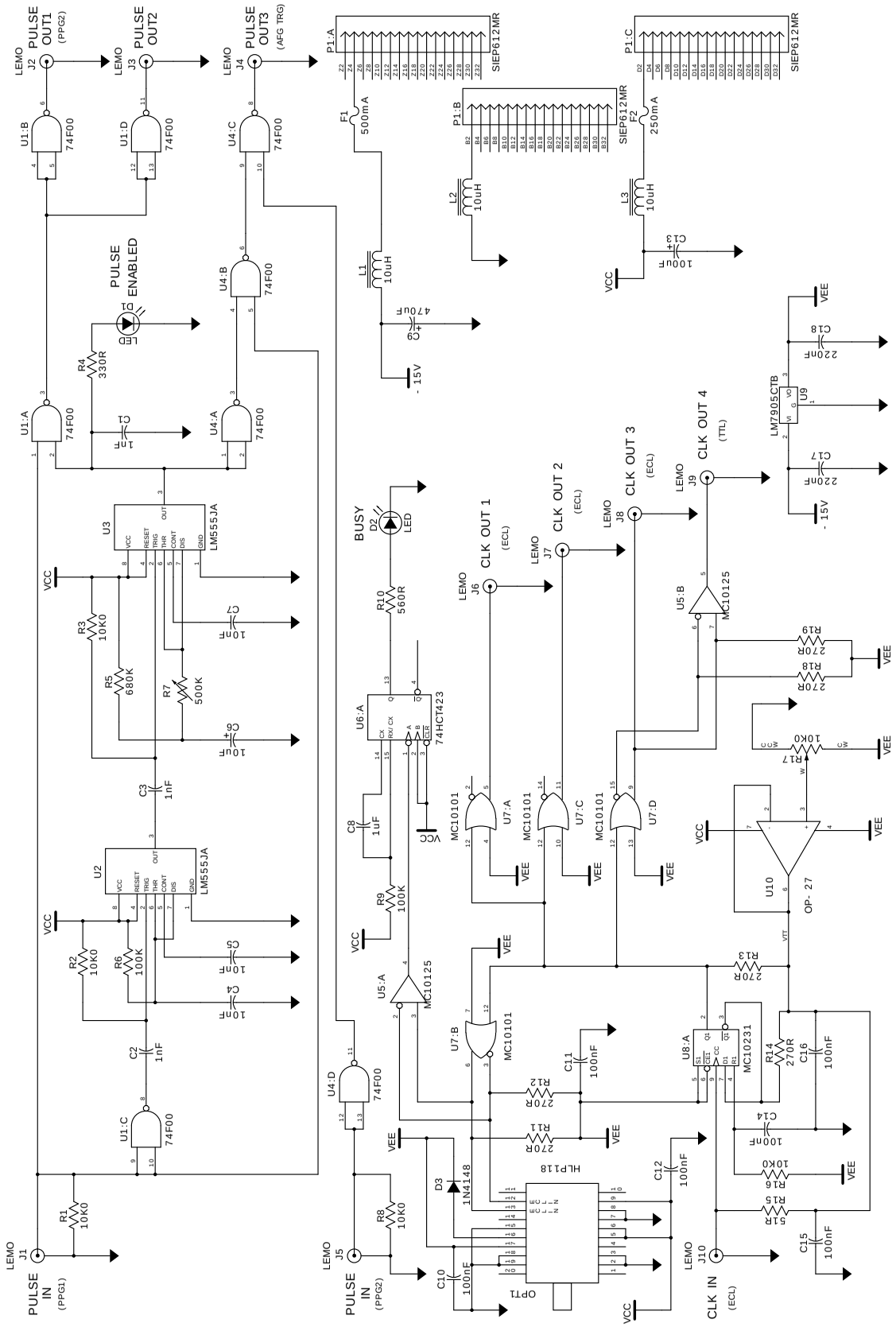

Figure B.1: Schematic of the optical clock transmitter.

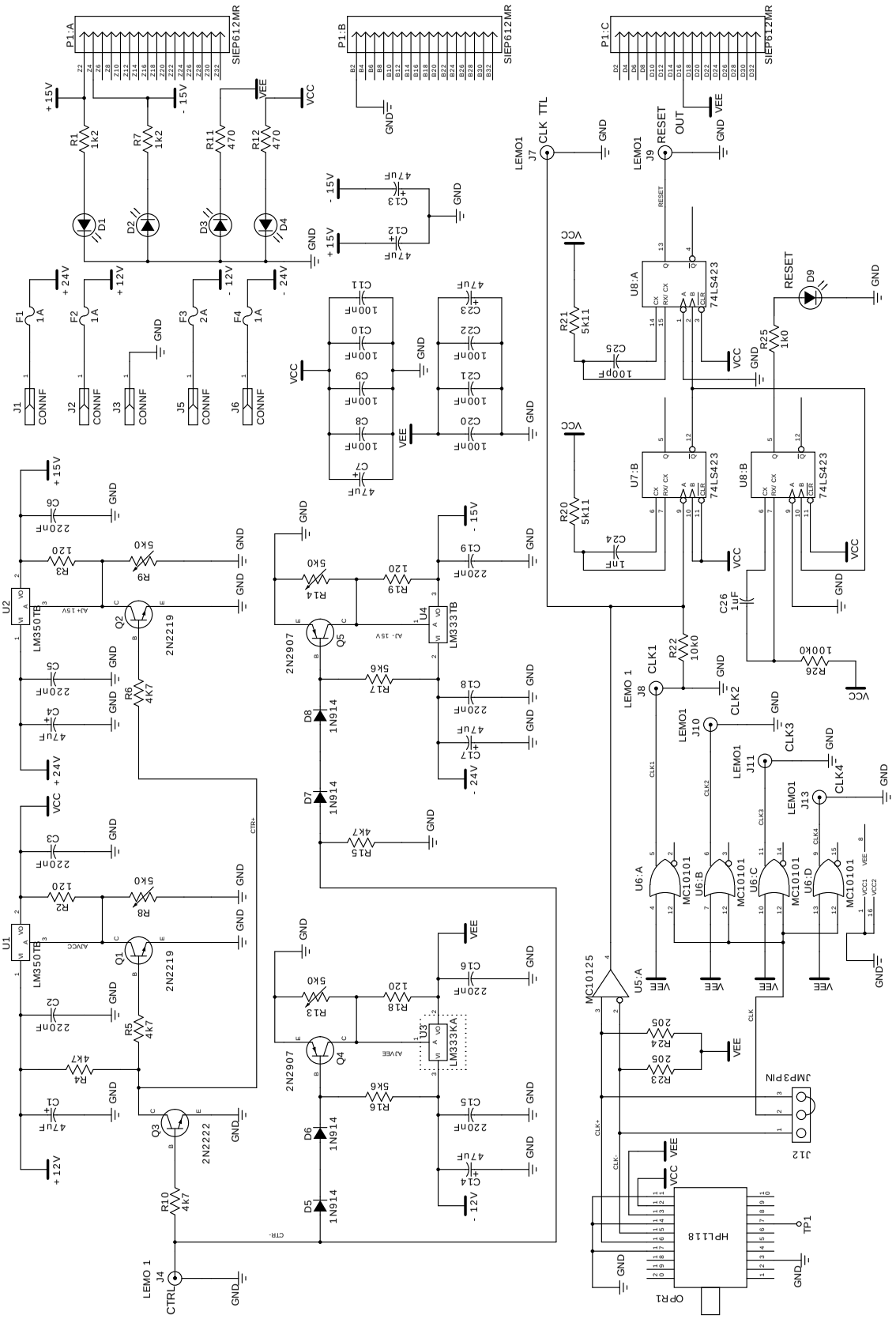

Figure B.2: Schematic of optical clock receiver.

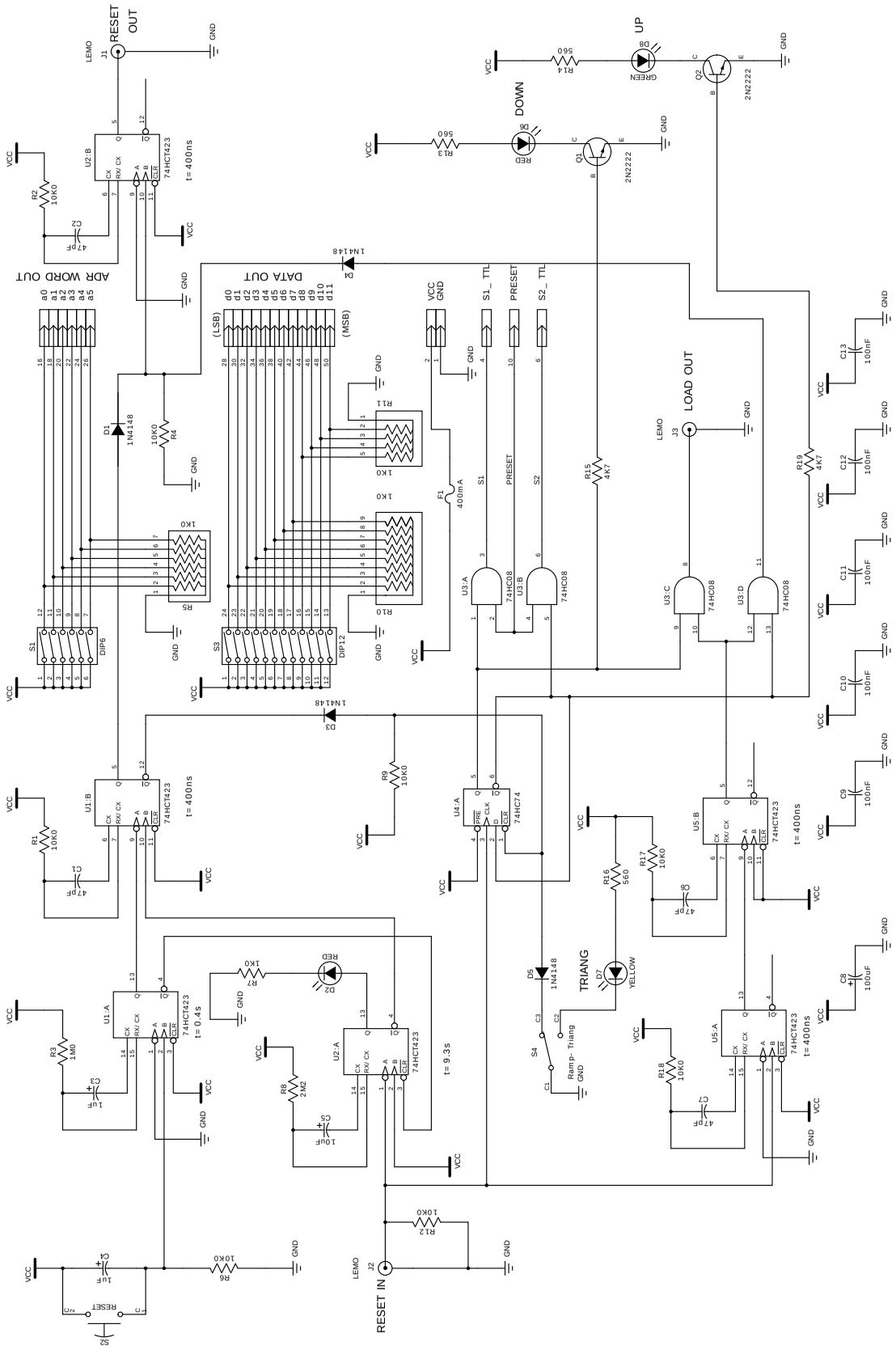

Figure B.3: Schematic of the fast ramp generator triangular↔ramp control module.

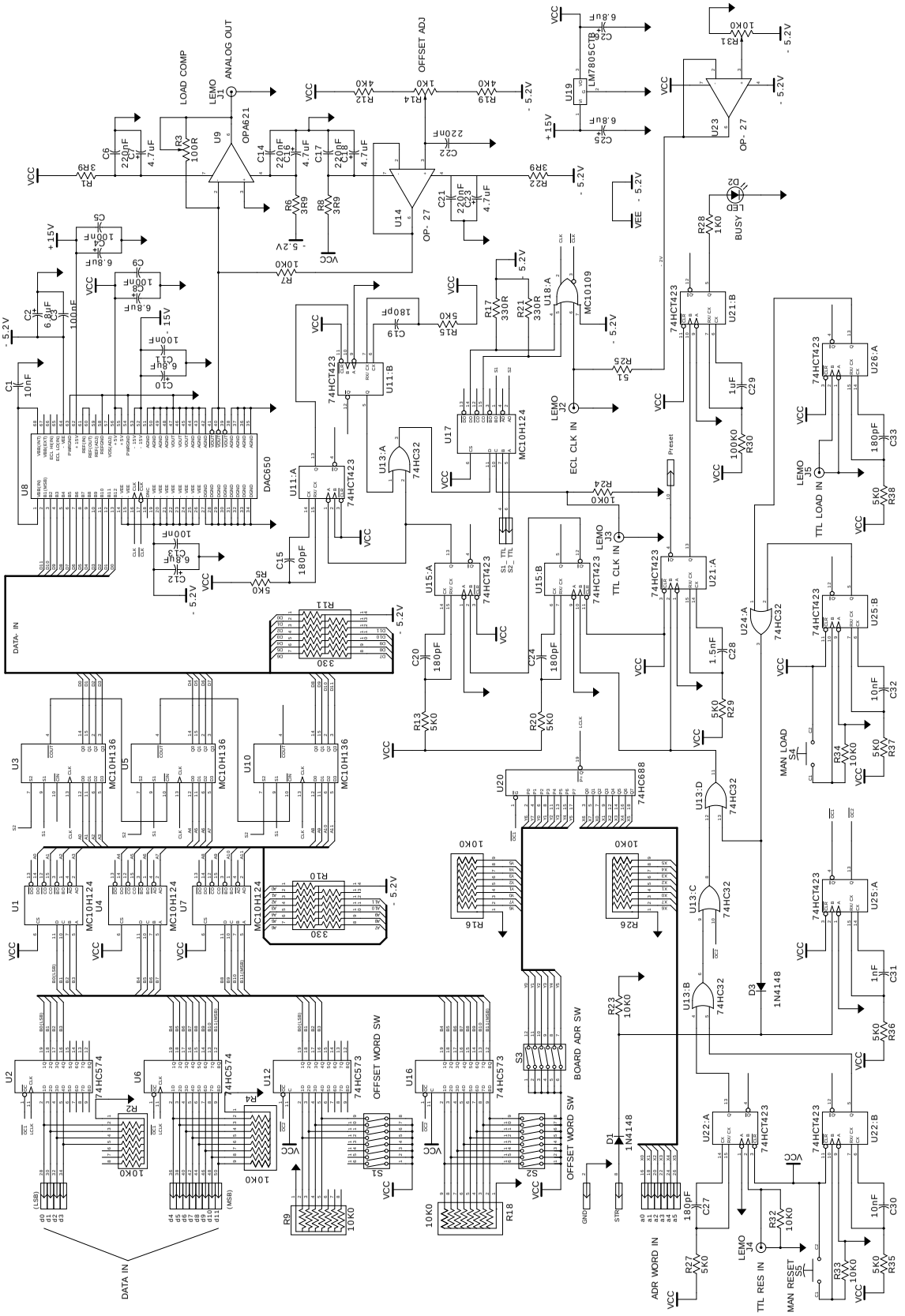

Figure B.4: Schematic of the fast ramp generator.

C Control and signal conditioning electronics

HTO 8-12	K (GHz)	Q (GHz)	**HTO 12-18**	Ka (GHz)	V (GHz)	W (GHz)
8.125	**16.250**	32.500	12.125	24.250	48.500	**72.750**
8.375	16.750	33.500	12.375	24.750	**49.500**	74.250
8.625	17.250	34.500	12.625	**25.250**	50.500	75.750
8.875	17.750	**35.500**	12.875	25.750	51.500	77.250
9.125	18.250	36.500	13.125	26.250	52.500	78.750
9.375	18.750	37.500	13.375	26.750	53.500	80.250
9.625	19.250	38.500	13.625	27.250	54.500	81.750
9.875	19.750	39.500	13.875	27.750	55.500	83.250
10.125	20.250	40.500	14.125	28.250	56.500	84.750
10.375	20.750	41.500	14.375	28.750	57.500	86.250
10.625	21.250	42.500	14.625	29.250	58.500	87.750
10.875	21.750	43.500	14.875	29.750	59.500	89.250
11.125	22.250	44.500	15.125	30.250	60.500	90.750
11.375	22.750	45.500	15.375	30.750	61.500	92.250
11.625	23.250	46.500	15.625	31.250	62.500	93.750
11.875	23.750	47.500	15.875	31.750	63.500	95.250
12.125	24.250	48.500	16.125	32.250	64.500	96.750
12.375	24.750	**49.500**	16.375	32.750	65.500	98.250
12.625	**25.250**	50.500	16.625	33.250	66.500	**99.750**
12.875	25.750	51.500	16.875	33.750	67.500	101.250
-	-	-	17.125	34.250	68.500	102.750
-	-	-	17.375	34.750	69.500	104.250
-	-	-	17.625	35.250	70.500	105.750
-	-	-	17.875	35.750	71.500	107.250
-	-	-	18.125	36.250	**72.500**	108.750
-	-	-	18.375	36.750	73.500	110.250
-	-	-	18.625	**37.250**	74.500	111.750
-	-	-	18.875	37.750	75.500	113.250

Table C.1: Frequency markers for each band.

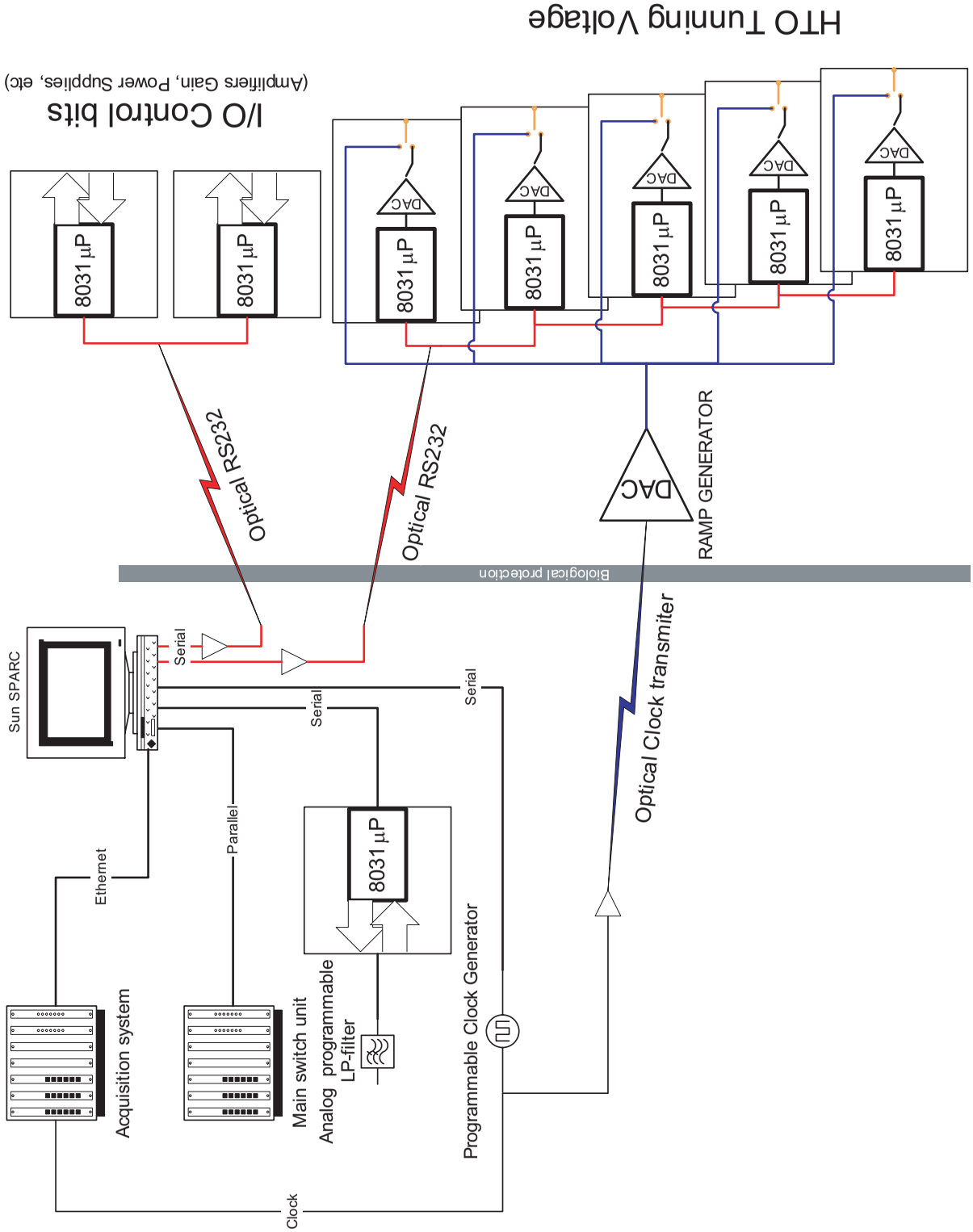

Figure C.1: Block diagram of the control and data acquisition system.

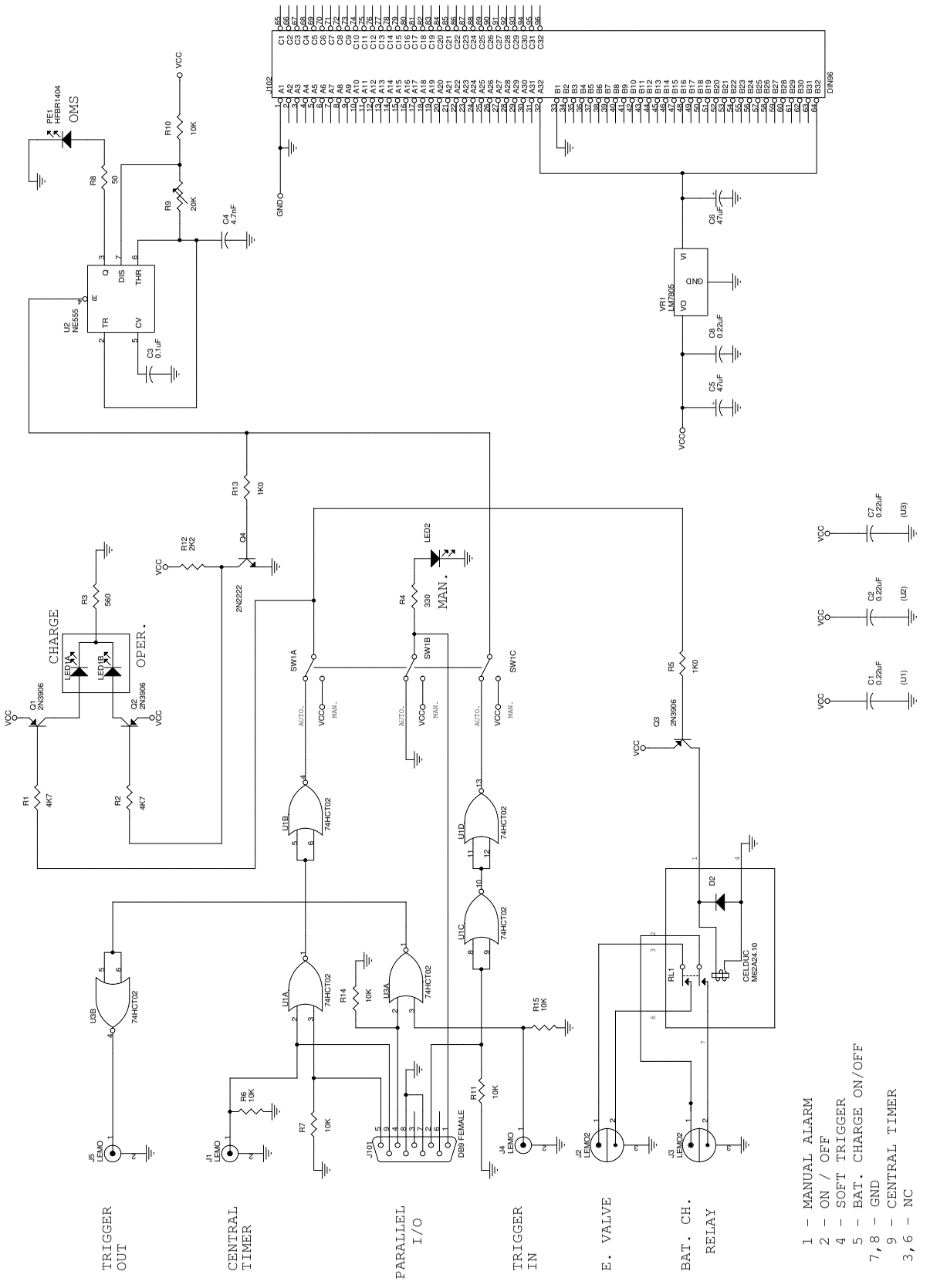

Figure C.2: Schematic of the main control unit.

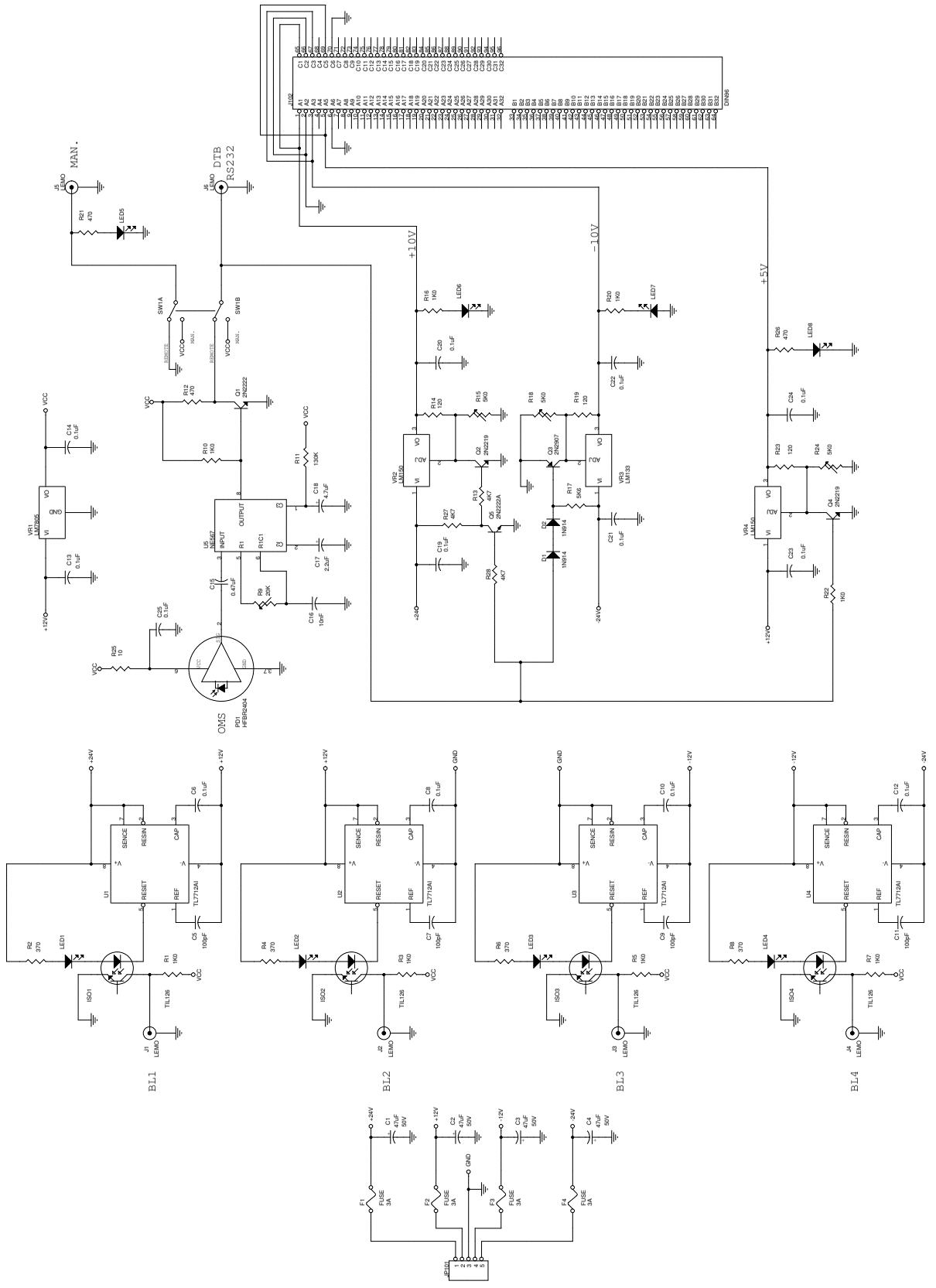

Figure C.3: Schematic of the main switch unit.

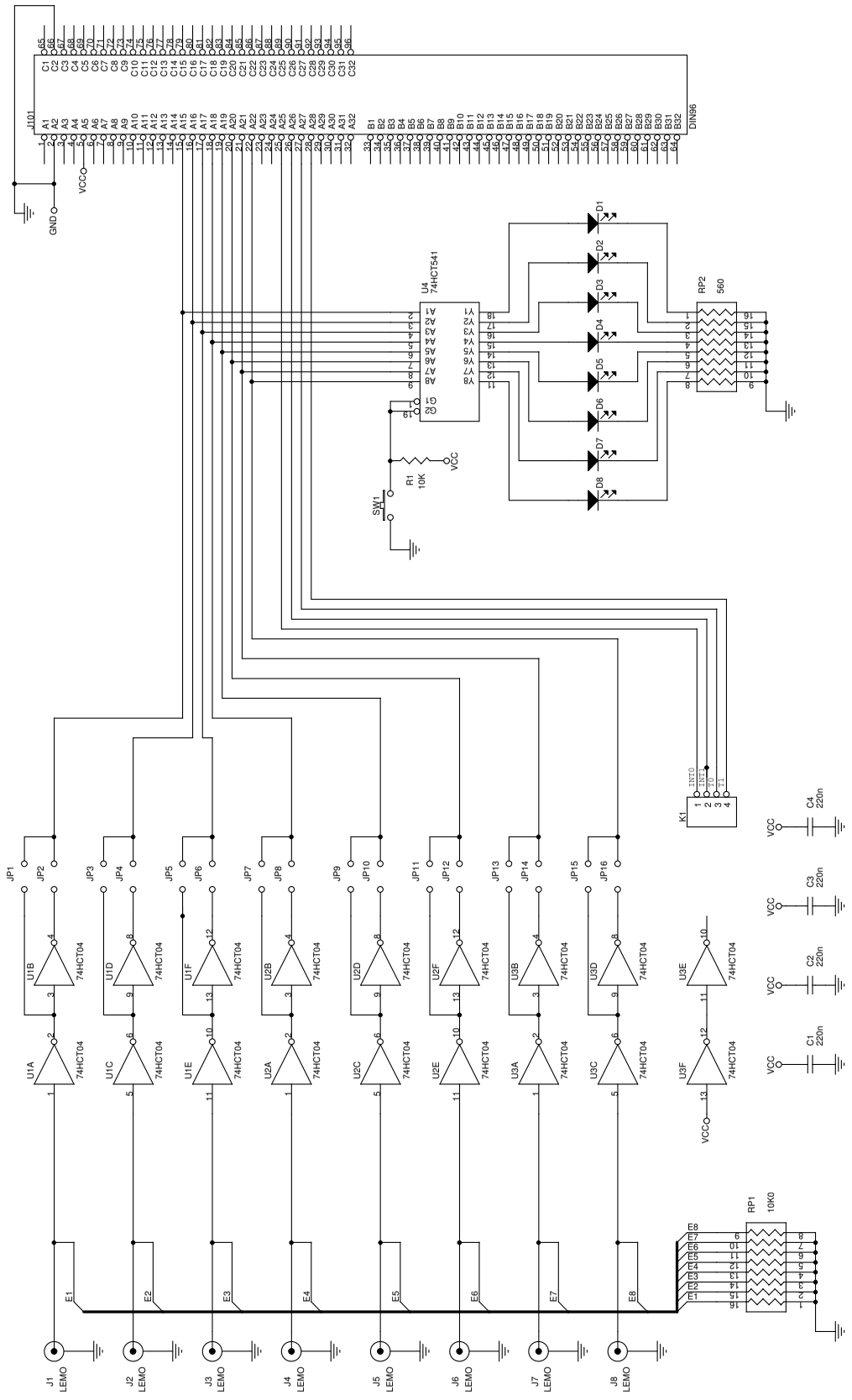

Figure C.4: Schematic of the control input board.

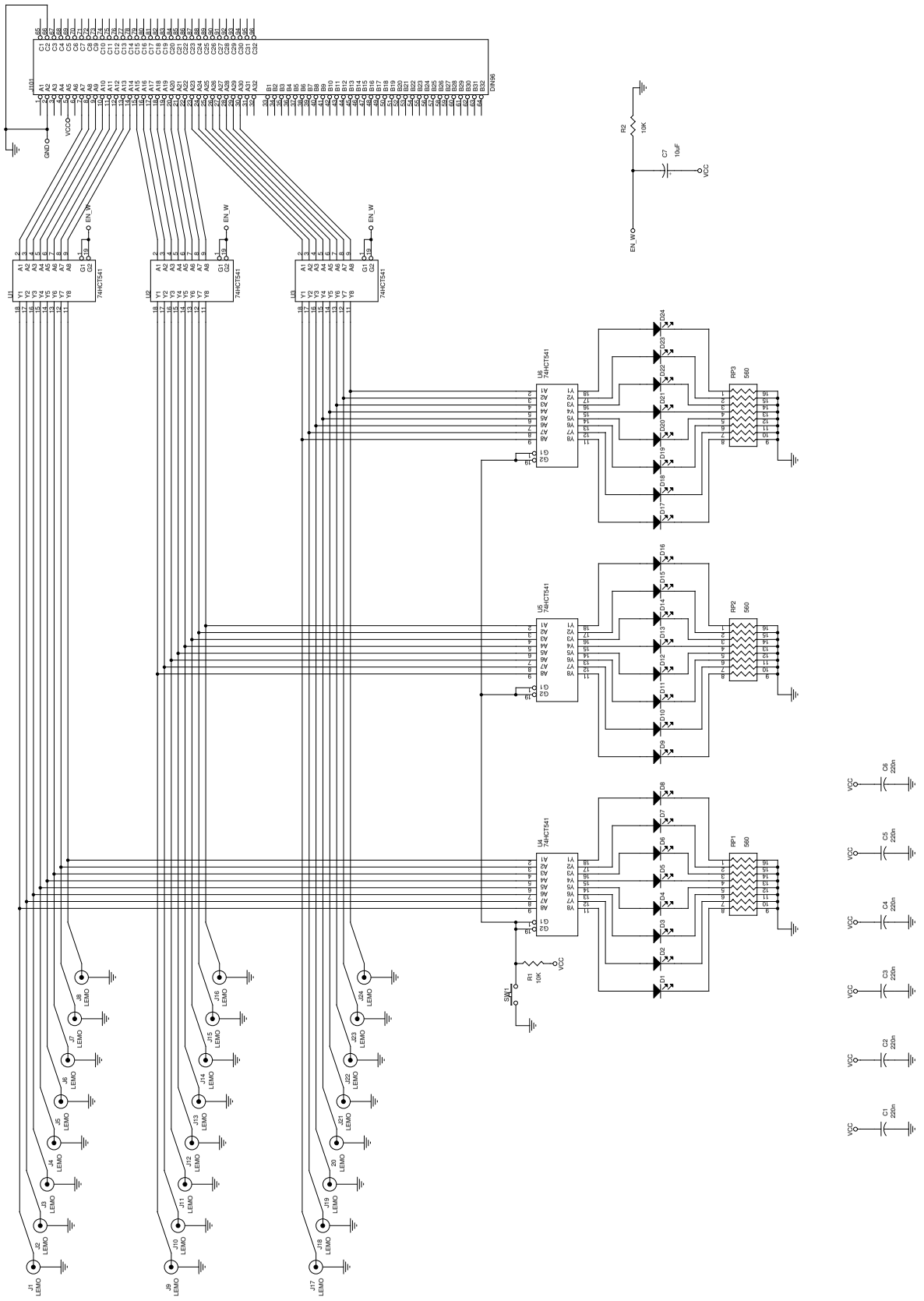

Figure C.5: Schematic of the control output board.

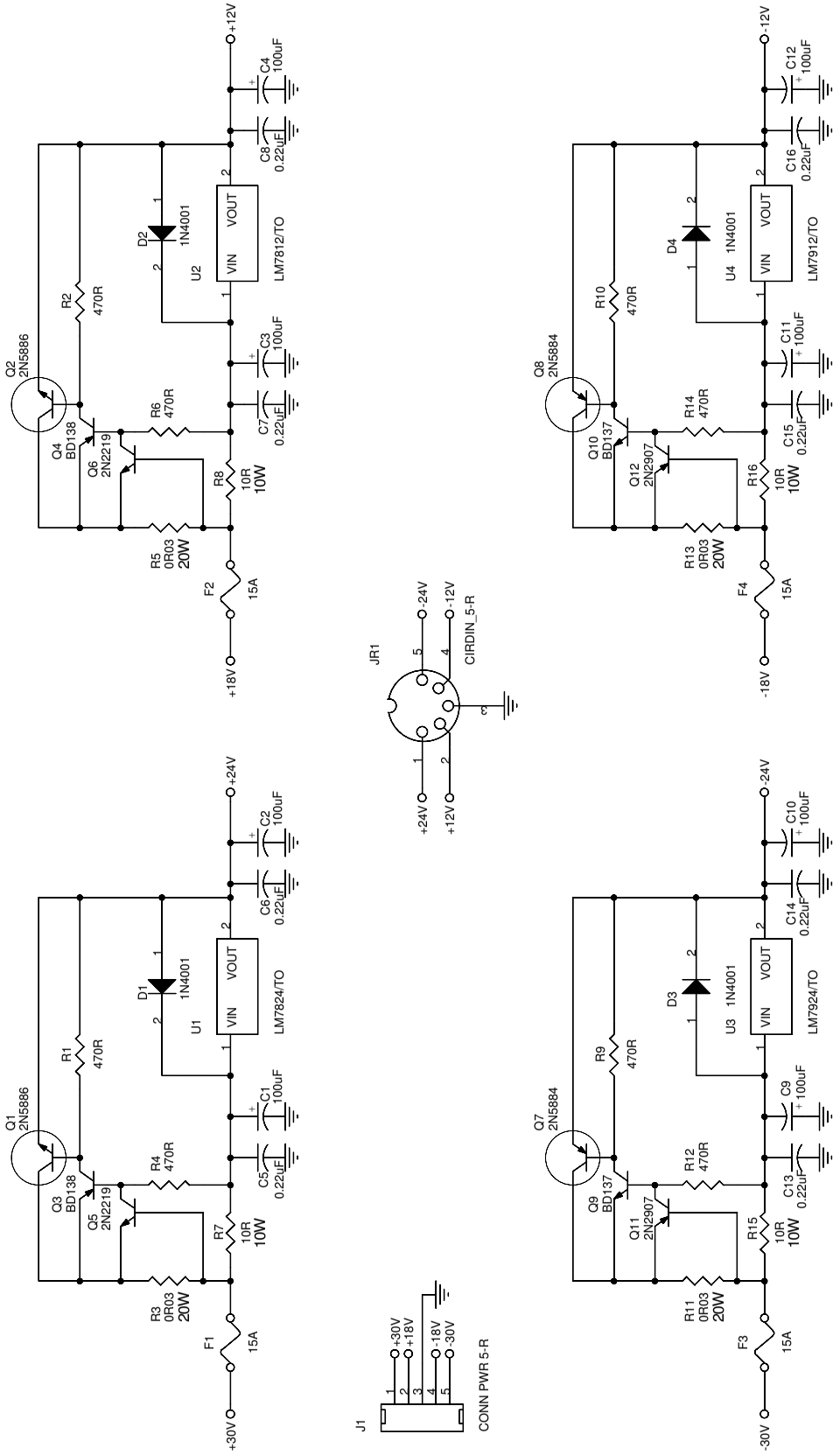

Figure C.6: Schematic of the main voltage regulator.

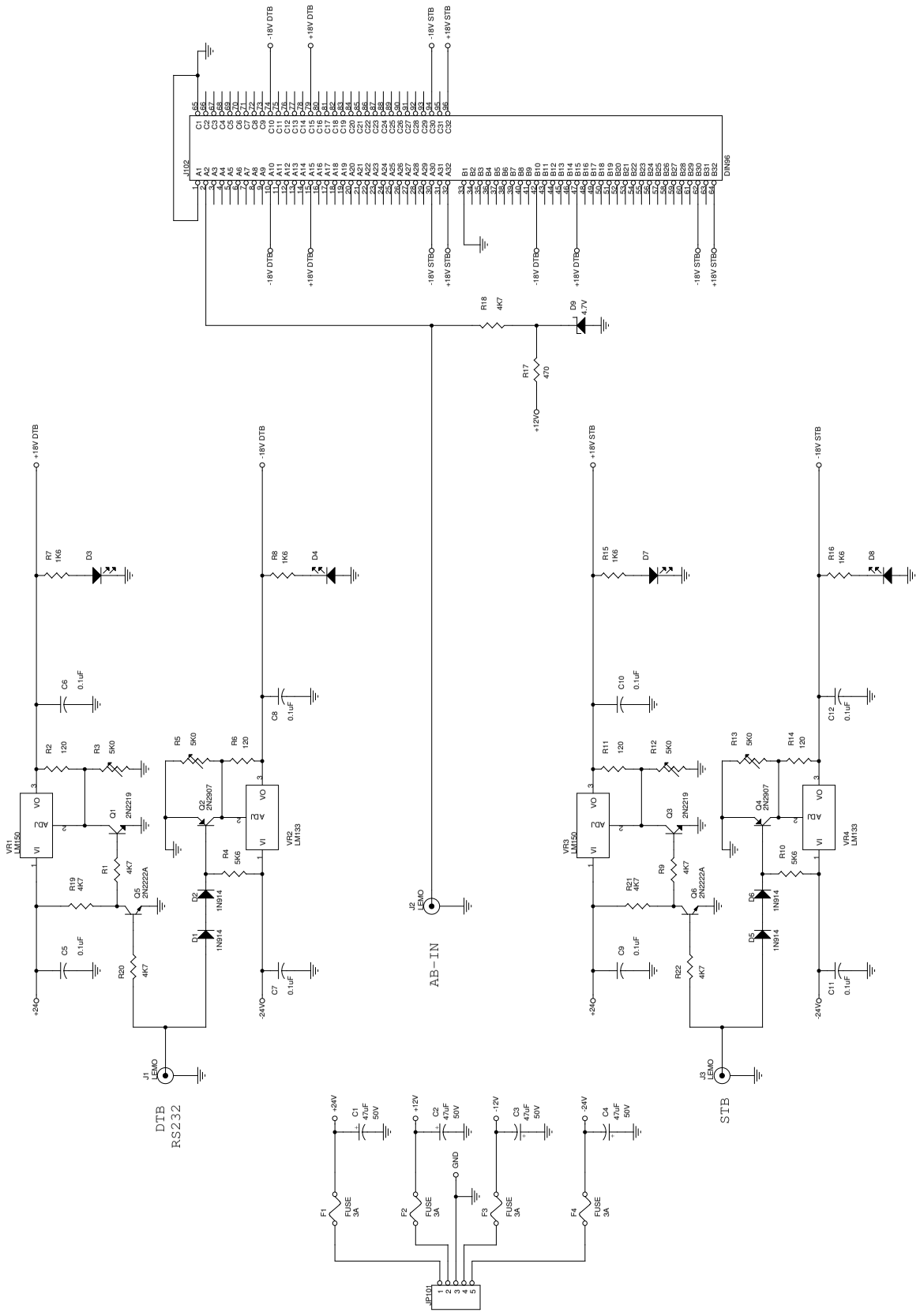

Figure C.7: Schematic of the optical boards power supply.

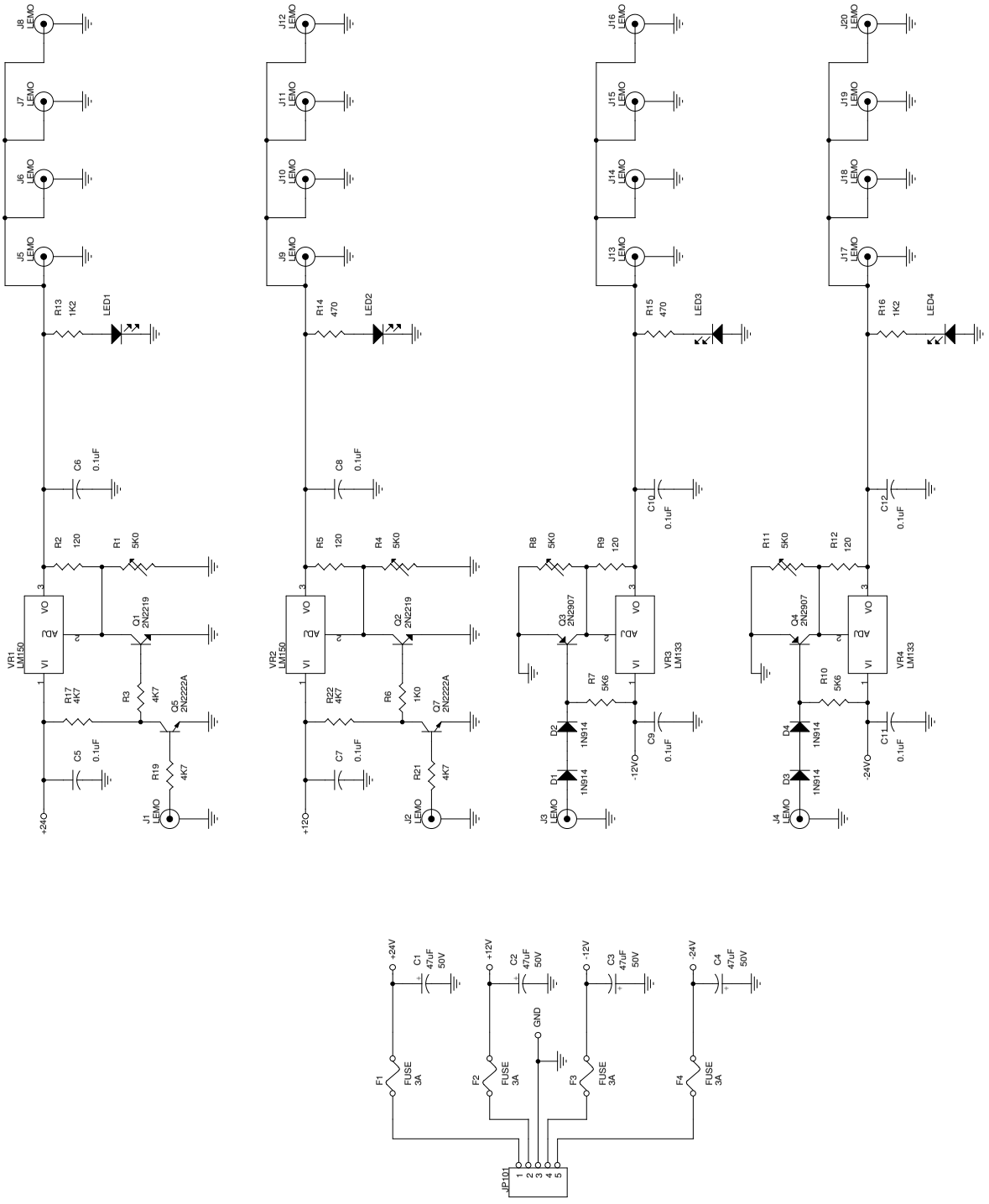

Figure C.8: Schematic of the oscillator and detection power supply.

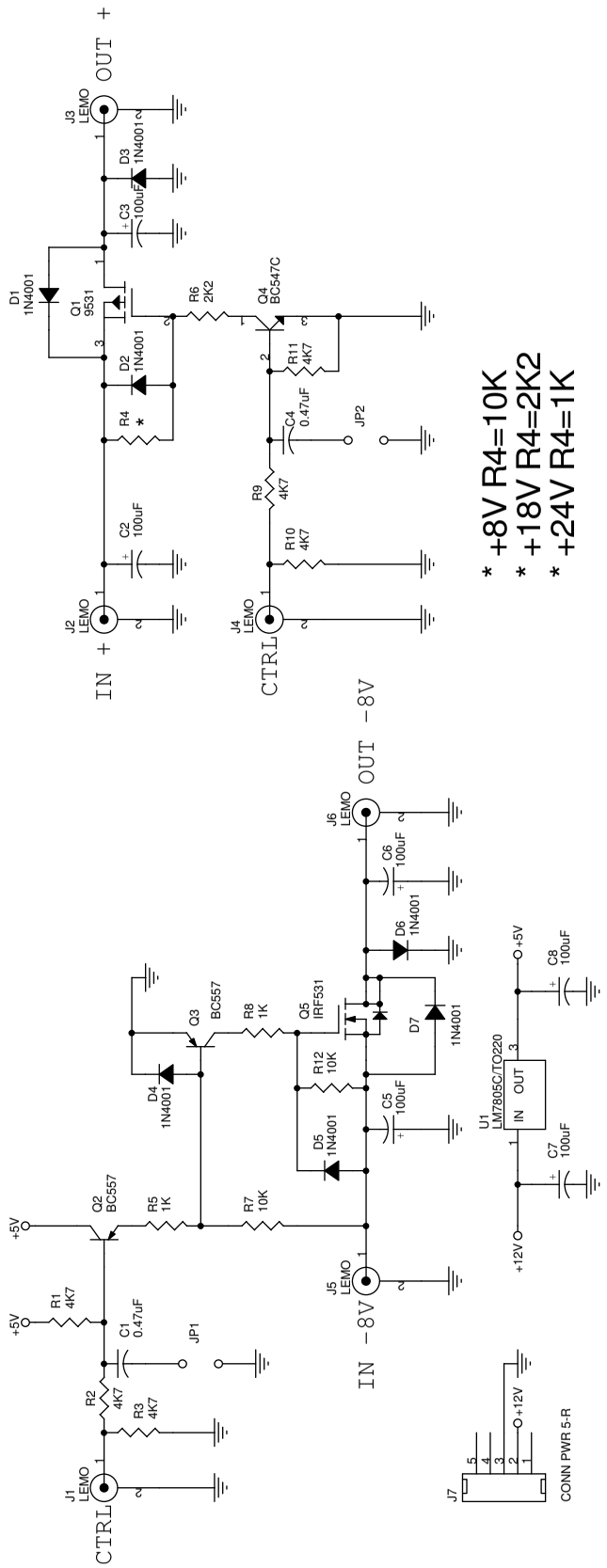

Figure C.9: Schematic of the heterodyne power supply switch.

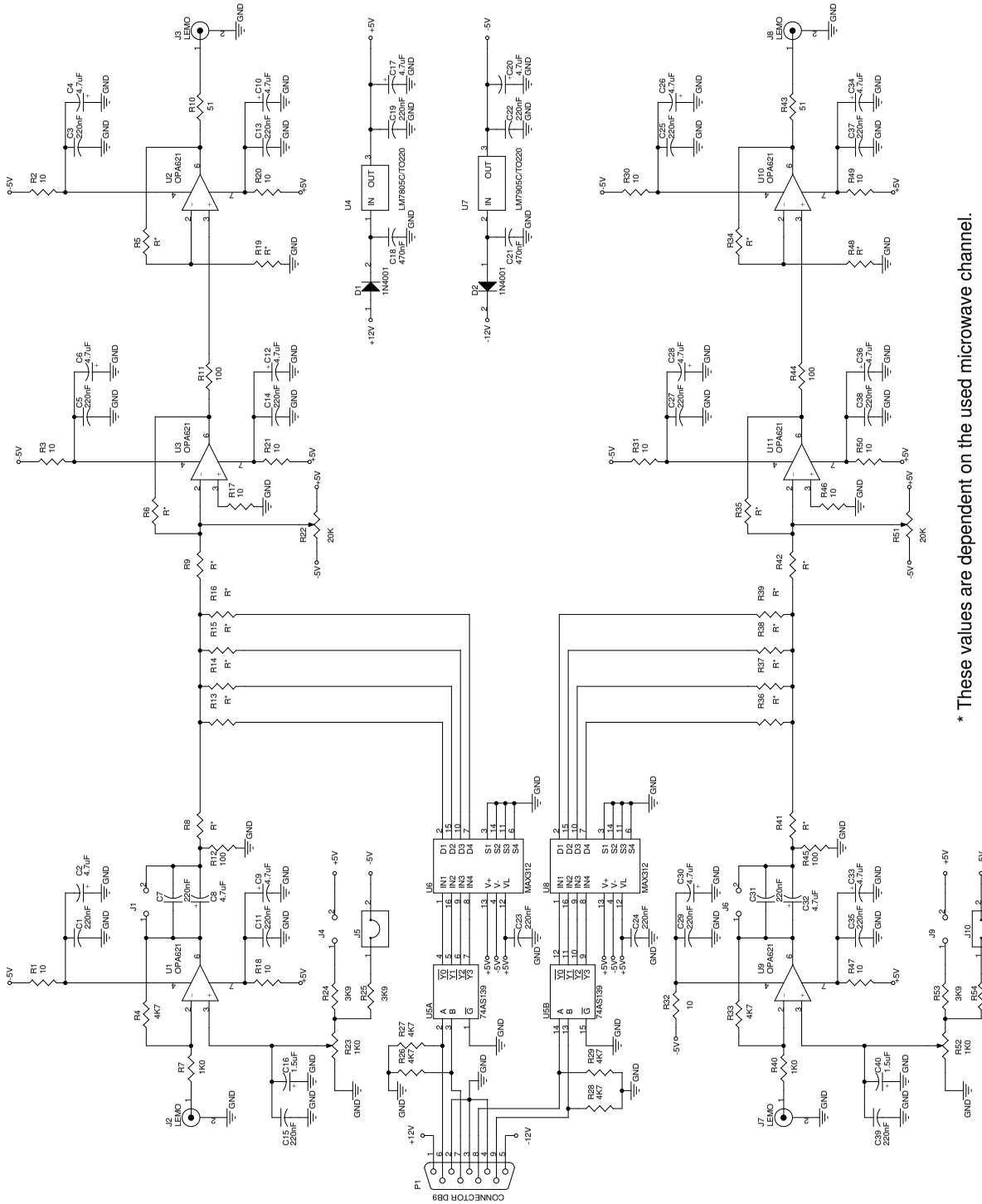

Figure C.10: Schematic of the detection amplifier.

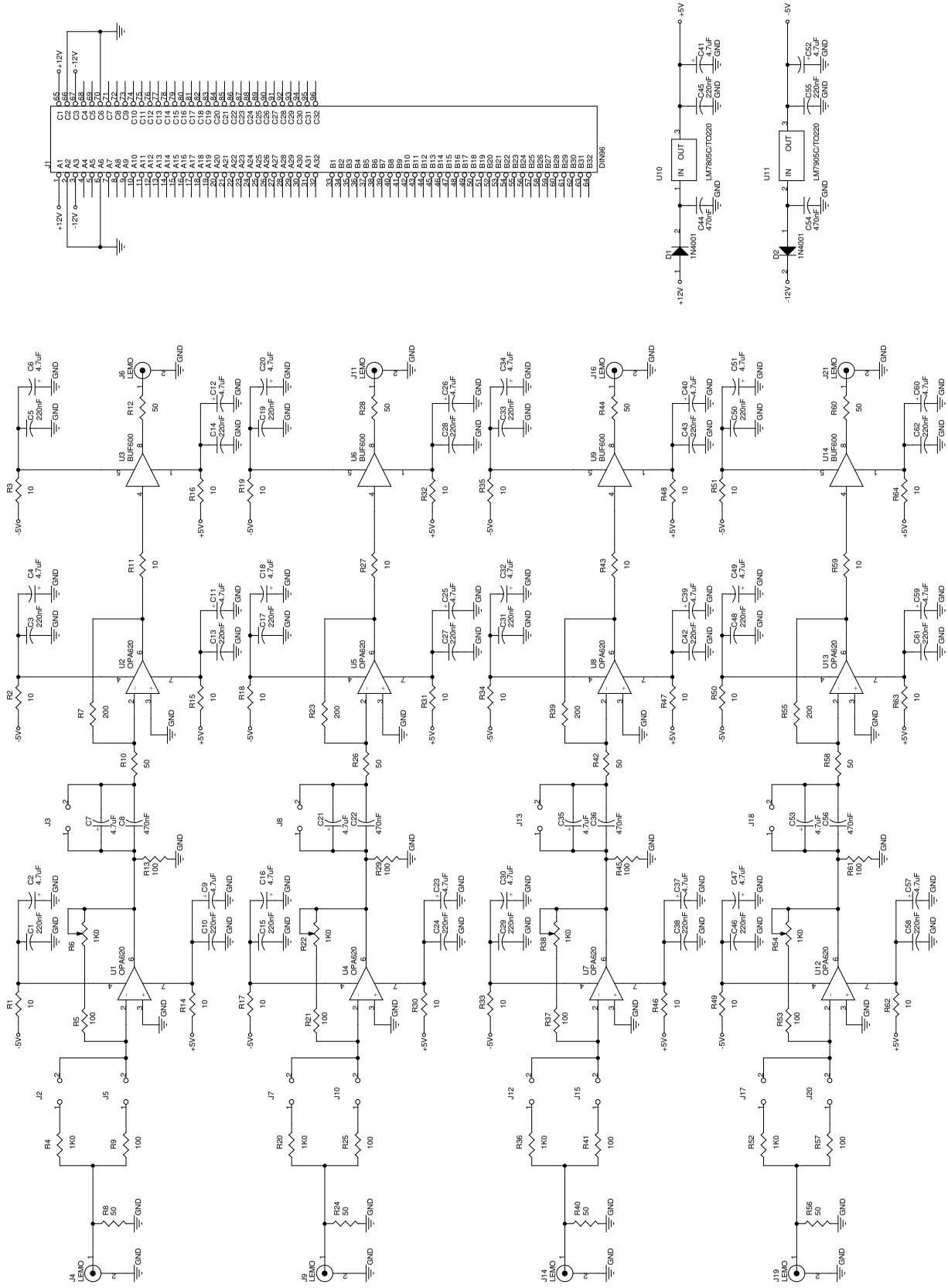

Figure C.11: Schematic of the acquisition amplifier.

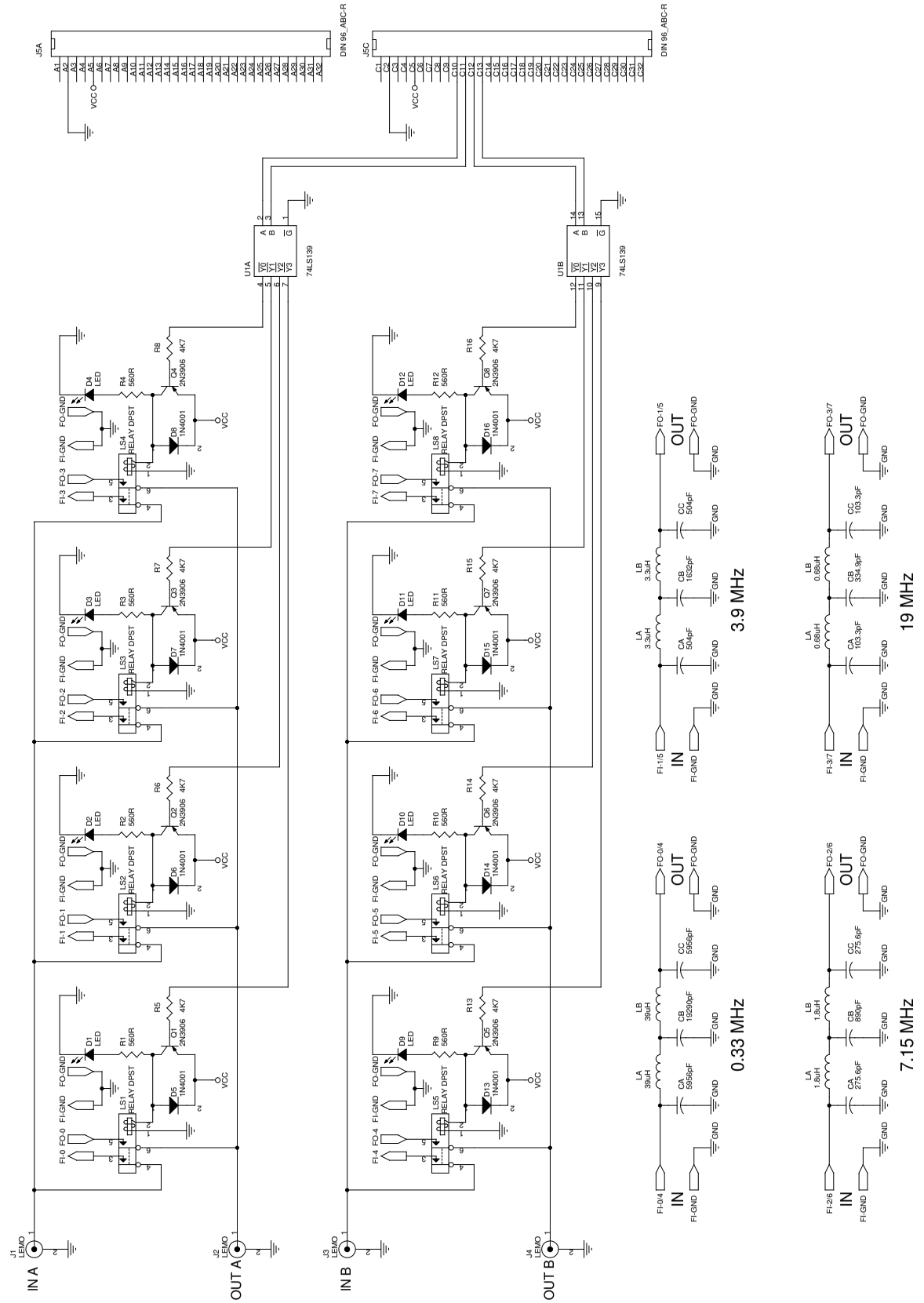

Figure C.12: Schematic of the acquisition low-pass filter board.